EVALUATION OF THE SOIL MOISTURE PREDICTION ACCURACY OF A SPACE RADAR USING SIMULATION TECHNIQUES

Remote Sensing Laboratory
RSL Technical Report 429-1

F. T. Ulaby, M. C. Dobson, J. A. Stiles, R. K. Moore and J. C. Holtzman

Fawwaz T. Ulaby, Principal Investigator

Final Report

Supported by:
NATIONAL AERONAUTICS AND SPACE ADMINISTRATION
Goddard Space Flight Center
Greenbelt, Maryland 20771
CONTRACT NAS 5-25807

THE UNIVERSITY OF KANSAS CENTER FOR RESEARCH, INC.
2291 Irving Hill Drive—Campus West
Lawrence, Kansas 66045

THE UNIVERSITY OF KANSAS CENTER FOR RESEARCH, INC.

2291 Irving Hill Drive—Campus West
Lawrence, Kansas 66045

Telephone: (913) 864-4832

EVALUATION OF THE SOIL MOISTURE PREDICTION ACCURACY OF A SPACE RADAR USING SIMULATION TECHNIQUES

Remote Sensing Laboratory
RSL Technical Report 429-1

F. T. Ulaby, M. C. Dobson, J. A. Stiles,
R. K. Moore and J. C. Holtzman

Fawwaz T. Ulaby, Principal Investigator

Final Report

Supported by:

NATIONAL AERONAUTICS AND SPACE ADMINISTRATION
Goddard Space Flight Center
Greenbelt, Maryland 20771

CONTRACT NAS 5-25807

1. Report No. NASA CR-	2. Government Accession No.	3. Recipient's Catalog No.
4. Title and Subtitle EVALUATION OF THE SOIL MOISTURE PREDICTION ACCURACY OF A SPACE RADAR USING SIMULATION TECHNIQUES		5. Report Date May 1981 6. Performing Organization Code
7. Author(s) Ulaby, Dobson, J. Stiles, Moore & Holtzman		8. Performing Organization Report No. RSL TR 429-1
9. Performing Organization Name and Address Remote Sensing Laboratory University of Kansas Center for Research, Inc. 2291 Irving Hill Drive - Campus West Lawrence, KS 66045		10. Work Unit No. 11. Contract or Grant No. NAS 5-25807
12. Sponsoring Agency Name and Address National Aeronautics and Space Administration Goddard Space Flight Center Greenbelt, Maryland 20771		13. Type of Report and Period Covered Final Report 14. Sponsoring Agency Code
15. Supplementary Notes		

16. Abstract

Image simulation techniques were employed to generate synthetic aperture radar (SAR) images of a 17.7 km x 19.3 km test site located east of Lawrence, Kansas. The simulations were performed for a space SAR at an orbital altitude of 600 km, with the following sensor parameters: frequency = 4.75 GHz, polarization = HH, and angle of incidence range = 7° - 22° from nadir. Three sets of images were produced corresponding to three different spatial resolutions, namely 20 m x 20 m with 12 looks, 100 m x 100 m with 23 looks, and 1 km x 1 km with 1000 looks. Each set consisted of images for four different soil moisture distributions across the test site. The purpose of this study is to evaluate the accuracy with which soil moisture can be predicted for each of the 12 resolution/soil moisture distribution combinations. The input information used to specify the gray level of each of the 800,000 pixels contained in the image included (when applicable) soil moisture, soil type, vegetation cover, surface roughness, row direction (relative to the radar look-direction), and local slope, while the prediction algorithm is based on a generalized formula relating the received power to soil moisture, with no information avail-

17. Key Words (Selected by Author(s))	18. Distribution Statement		
Radar, simulation, imagery, soil moisture, resolution, satellite, microwave	U		
19. Security Classif. (of this report)	20. Security Classif. (of this page)	21. No. of Pages	22. Price*
Unclassified	Unclassified	189	

* For sale by the National Technical Information Service, Springfield, Virginia 22151.

able to it on the scene properties except for the angle of incidence with respect to the mean elevation of the test site. The results indicate that, for the agricultural portion of the test site, the soil moisture of about 90% of the pixels can be predicted with an accuracy of ±20% of field capacity. Among the three spatial resolutions, the 1 km x 1 km resolution gave the best results for most cases; however, for very dry soil conditions, the 100 m x 100 m resolution was slightly superior.

TABLE OF CONTENTS

LIST OF FIGURES

LIST OF TABLES

Page

EVALUATION OF THE SOIL MOISTURE PREDICTION ACCURACY OF A SPACE RADAR USING SIMULATION TECHNIQUES

F. T. Ulaby, C. Dobson, J. Stiles, R. K. Moore and J. Holtzman
Remote Sensing Laboratory
University of Kansas Center for Research, Inc.
Lawrence, Kansas 66045

ABSTRACT

Image simulation techniques were employed to generate synthetic aperture radar (SAR) images of a 17.7 km x 19.3 km test site located east of Lawrence, Kansas. The simulations were performed for a space SAR at an orbital altitude of 600 km, with the following sensor parameters: frequency = 4.75 GHz, polarization = HH, and angle of incidence range = 7° - 22° from nadir. Three sets of images were produced corresponding to three different spatial resolutions, namely 20 m x 20 m with 12 looks, 100 m x 100 m with 23 looks, and 1 km x 1 km with 1000 looks. Each set consisted of images for four different soil moisture distributions across the test site. The purpose of this study is to evaluate the accuracy with which soil moisture can be predicted for each of the 12 resolution/soil moisture distribution combinations. The input information used to specify the gray level of each of the 800,000 pixels contained in the image included (when applicable) soil moisture, soil type, vegetation cover, surface roughness, row direction (relative to the radar look direction), and local slope, while the prediction algorithm is based on a generalized formula relating the received power to soil moisture, with no information available to it on the scene properties except for the angle of incidence with respect to the mean elevation of the test site. The results indicate that, for the agricultural portion of the test site, the soil moisture of about 90% of the pixels can be predicted with an accuracy of ±20% of field capacity. Among the three spatial resolutions, the 1 km x 1 km resolution gave the best results for most cases; however, for very dry soil conditions, the 100 m x 100 m resolution was slightly superior.

1.0 INTRODUCTION

During the past decade, several investigations have been conducted to evaluate the role of active microwave remote sensing techniques for sensing soil moisture content [1-19]. Although some of these investigations were not strictly related to soil moisture, their findings provided information on scene features (such as vegetation cover and surface roughness) that are related to the problem of sensing soil moisture with radar.

With the exception of one study, the investigations reported to date have involved the use of ground-based [1-14] or airborne radars [10, 13-18]. The exception is a Skylab investigation [19] in which the backscattering coefficient σ^o, measured by Skylab's 13.9 GHz scatterometer, was related to the moisture content of soil samples obtained from the ground areas observed by the sensor. Although σ^o exhibited a fair degree of correlation with moisture content, the results of the investigation should be considered as only a positive indication, rather than as a demonstration, of the potential use of radar for sensing soil moisture. This qualification is based on the fact that the resolution area of Skylab's scatterometer was of the order of 200 km^2, while the soil moisture estimate was based on a few point-samples.

Seasat provided the first opportunity for investigating the radar response to soil moisture with a high-resolution spaceborne imaging radar. In support of a project organized by Texas A&M University, Seasat SAR imagery was acquired for several passes over a soil moisture test-site in Oklahoma, and aircraft underflights were

also made using the NASA/JSC 1.6 GHz scatterometer. A report summarizing the results is forthcoming [20].

The purpose of this report is to document the results of an investigation conducted to evaluate the applicability of active microwave approaches to soil-moisture sensing from a satellite platform and to define the general system parameters of such an active microwave system. The report is divided into three major topics. The first topic (Section 2) consists of a literature review of the radar response to soil moisture and related scene parameters. The objective of this section is to specify the radar configuration that holds the greatest promise in terms of the accuracy and precision with which soil moisture may be estimated with an active microwave system. Specifically, the following parameters are to be identified: (a) microwave frequency, (b) angle of incidence range, (c) polarization configuration, and (d) the lower and upper limits of the dynamic range of σ^o. These parameters are used in Section 3 to evaluate the impact of spatial resolution on system-hardware and signal-processing requirements. Several different system configurations are considered, including the fully focused synthetic aperture radar (SAR), partially focused SAR, unfocused SAR, and the real aperture radar (RAR). Additionally, a combined radiometer-SAR (RADISAR) configuration is considered.

Three candidate configurations will be chosen to evaluate the relationship between soil moisture estimation accuracy and spatial resolution. This evaluation is the subject of the third topic (Sections 4 and 5). For each candidate configuration, image simula-

tion techniques are employed to generate a radar image of a test site located in the vicinity of Lawrence, Kansas, using a multitude of scene parameters to characterize the scattering coefficient of each resolution cell (pixel). Among these parameters are the soil moisture content, soil texture, local slope, cover-type, etc. The image thus generated is then subjected to a generalized algorithm using σ^o and satellite altitude and position as sole inputs and moisture content as sole output. Upon applying this algorithm, a predicted soil moisture "map" is produced. A soil moisture error map is then produced by taking the difference between the predicted moisture content and the true moisture content on a pixel-by-pixel basis. The performance of each of the three candidate system configurations (corresponding to three different spatial resolutions) is evaluated in terms of error distribution functions.

2.0 REVIEW OF THE RADAR RESPONSE TO SOIL MOISTURE

Table 2.1 provides a summary of the major studies reported in the literature that pertain to radar backscatter from soil surfaces. The scene parameters of primary importance are:

(a) soil moisture (profile)

(b) small-scale soil surface roughness

(c) large-scale periodic surface patterns (row tillage)

TABLE 2.1

Summary of Active Microwave Investigations
of Soil Moisture and Related Scene Variables

Platform	Soil Cover	Frequency GHz	Angular Range (Degrees)	Polarization(s)	Institution	Year Reported	Reference	Major Emphasis of Investigations and Comments
Truck	Bare	4-8	0-70	HH, VV	U. of Kansas	1974	[1,2]	Surface roughness
Truck	Bare	2-8	0-40	HH, VV	U. of Kansas	1976	[3]	Surface roughness, Miller clay soil
Truck	Bare	1-8	0-30	HH, VV, HV	U. of Kansas	1978	[4]	Surface roughness, Eudora silt loam soil
Truck	Bare	1-8	10-20	HH, VV, HV	U. of Kansas	1981	[5]	Soil type
Tower	Bare	9	10-80	HH, VV, HV	U. of Delft (Netherlands)	1979	[6]	Surface roughness
Tower	Bare	1.5,3,4.5,9	10-80	HH, VV	Inst. Nat'l. Agronomique (France)	1979	[7]	Surface roughness
Tower	Bare	1.5,3,4.5,9	0-70	HH, VV, HV	U. Paul Sabatier (France)	1980	[8]	Surface roughness
Car	Bare	9	30	HH, HV	U. of Tokyo (Japan)	1978	[9]	Surface roughness, low density soil
Truck & Aircraft	Bare	1.6,4.75,13.3	5-50	HH, VV, HV VV only for 13.3	NASA/JSC	1980	[10]	Row direction (of large-scale periodic patterns)
Truck	Vegetation	4-8	0-70	HH, VV, HV	U. of Kansas	1975	[11]	Masking by vegetation cover
Truck	Vegetation	8-18	0-70	HH, VV, HV	U. of Kansas	1975	[12]	Masking by vegetation cover
Truck	Vegetation	1-18	0-70	HH, VV, HV	U. of Kansas	1979	[13]	Row direction
Truck	Vegetation	1-8	0-50	HH, VV, HV	U. of Kansas	1979	[14]	Masking by vegetation
Aircraft	Bare and Vegetation	0.4,13.3	5-60	VV	U. of Kansas	1974	[15]	Differentiation between dry and irrigated fields
Aircraft	Bare	1.6, 13.3	5-40	HH, HV(1.6) VV(13.3)	Texas A & M U.	1978	[16]	Multi-date flights
Aircraft	Watersheds	0.4,1.6,4.75	5-50	HH	USDA/NASA/GSFC	1980	[17]	Multi-date flights
Aircraft	Bare and Vegetation	1.6,4.75,13.3	5-50	HH, VV, HV VV only for 13.3	U. of Kansas	1980	[18]	Soil moisture response for large number of fields
Skylab	Bare and Vegetation	13.9	30	VV	U. of Kansas	1974	[19]	IFOV = 200 km^2
Seasat	Bare and Vegetation	1.3	20	HH	Texas A & M U.	1981	[20]	Multi-date passes, report in writing stage

(d) soil texture

(e) vegetation cover

Parameter (a), soil moisture content, is the quantity of interest, while parameters (b) - (e) are quantities whose influence on the backscattering coefficient σ^o should be either minimized or accounted for, as discussed next.

2.1 Small-Scale Surface Roughness

Surface roughness is the prime mechanism responsible for making non-nadir radar observations possible, since for a perfectly smooth surface the backscattered power is zero except at nadir. Hence, the effect of surface roughness on σ^o has received the greatest attention, relative to the other factors listed above. Based on experiments conducted by the University of Kansas in 1974 (for three different surface roughnesses) and in 1975 (for five different surface roughnesses), a set of radar parameters was proposed for minimizing the effect of surface roughness on σ^o. These were: $4\text{GHz} \lesssim f \lesssim 5\text{GHz}$, $7° < \theta < 20°$ and HH-polarization. Comparable performance may also be achieved using HV polarization, but the use of HV polarization is usually less desirable than HH because of the higher transmitter power levels that are required. Figure 2.1 shows a summary of the results in the form of the correlation coefficient ρ as a function of θ for three different microwave frequencies. Here ρ is the linear correlation coefficient between σ^o(dB) and the volumetric moisture content of the surface 0-1 cm layer. Later analyses have shown that

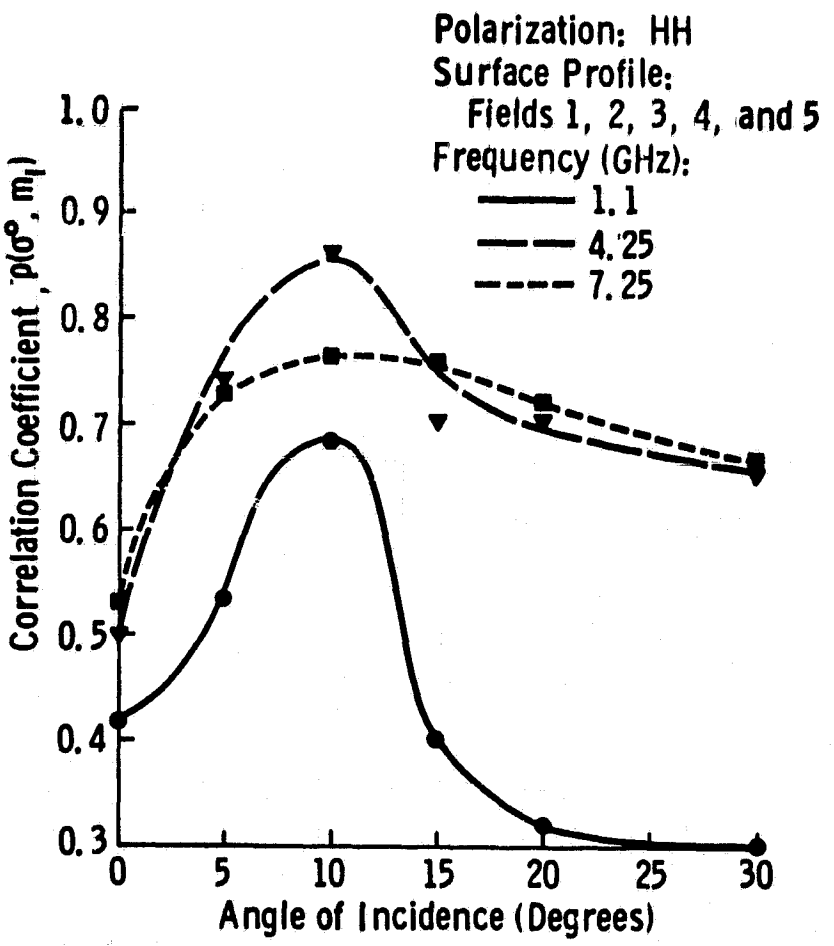

Figure 2.1 Linear correlation coefficient between σ^{o}(dB) and volumetric soil moisture of the surface 0-1 cm layer, plotted as a function of angle of incidence, for five different surface roughnesses (from [4]).

slightly higher magnitudes of ρ are obtained if the correlation is performed against the moisture in the 0-5 cm soil layer.

Figure 2.2 shows a similar set of curves for ρ versus θ based on airborne measurements made over watersheds in Oklahoma [17]. Although the magnitude of ρ is generally lower than that shown in Figure 2.1, the overall angular and frequency behavior is very similar. The lower magnitude of ρ is attributed to surface slope effects. The C-band channel (at 4.75 GHz) provides the highest magnitude of ρ (among the three frequencies used) and the peak value of ρ is in the 10° - 15° region, in agreement with the results shown in Figure 2.1.

The above conclusions were confirmed further by the experimental results reported by Le Toan et al. [8] of the Paul Sabatier University in Toulouse, France. Samples of their results are shown in Figures 2.3 and 2.4. The dependence on surface roughness is illustrated in Figure 2.3 where σ^o(dB) at 4.5 GHz is plotted as a function of rms surface height for several angles of incidence θ. On the basis of the behavior depicted in Figure 2.3 and other analyses, it was concluded that σ^o is least dependent on rms height for θ in the 6° - 20° range. Figure 2.4 shows σ^o versus m_v, the volumetric moisture content, at three microwave frequencies. The data shown include the smoothest and roughest surface conditions observed in their investigation.

2.2 Periodic Surface Patterns

Row tillage patterns associated with row crops, such as wheat, corn, and soybeans, represent a large-scale periodic surface pattern,

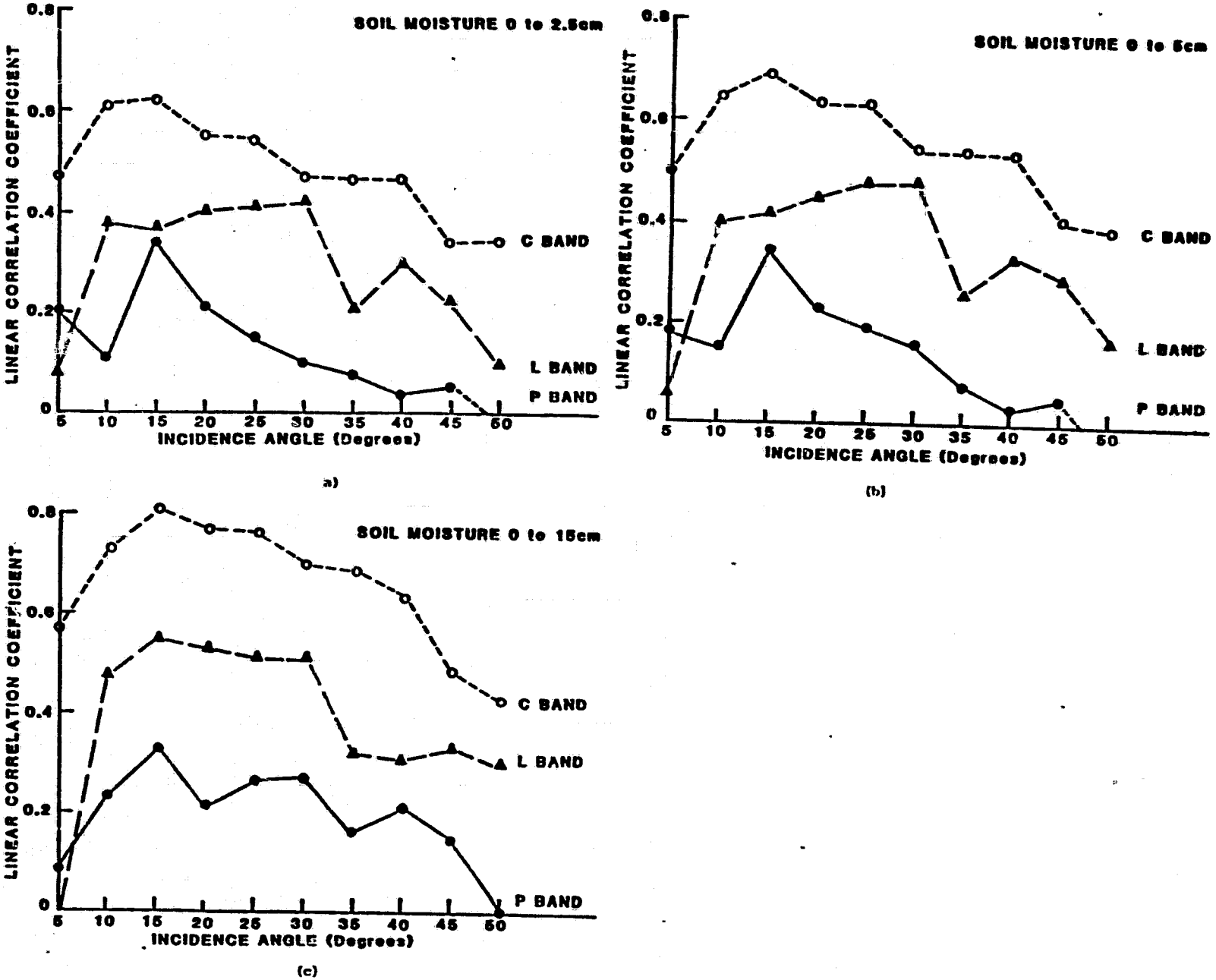

Figure 2.2 Linear correlation coefficient between σ^{o}(dB) and volumetric soil moisture as a function of angle of incidence for L-band (1.6 GHz), C-band (4.75 GHz) and X-band (0.4 GHz) (from Jackson et al. [17]).

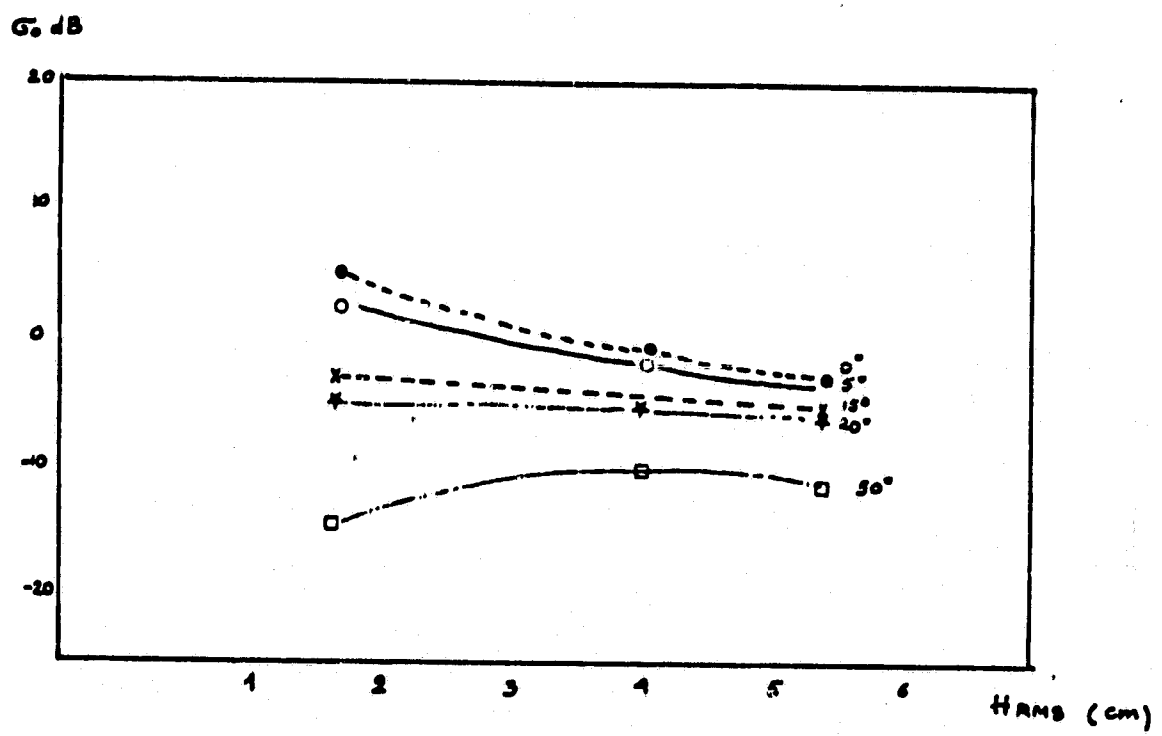

Figure 2.3 Variation of σ° with RMS height at 4.5 GHz, HH polarization for several angles of incidence. Soil moisture range: 0.12-0.18 g/cm^3 (from Le Toan et al. [8]).

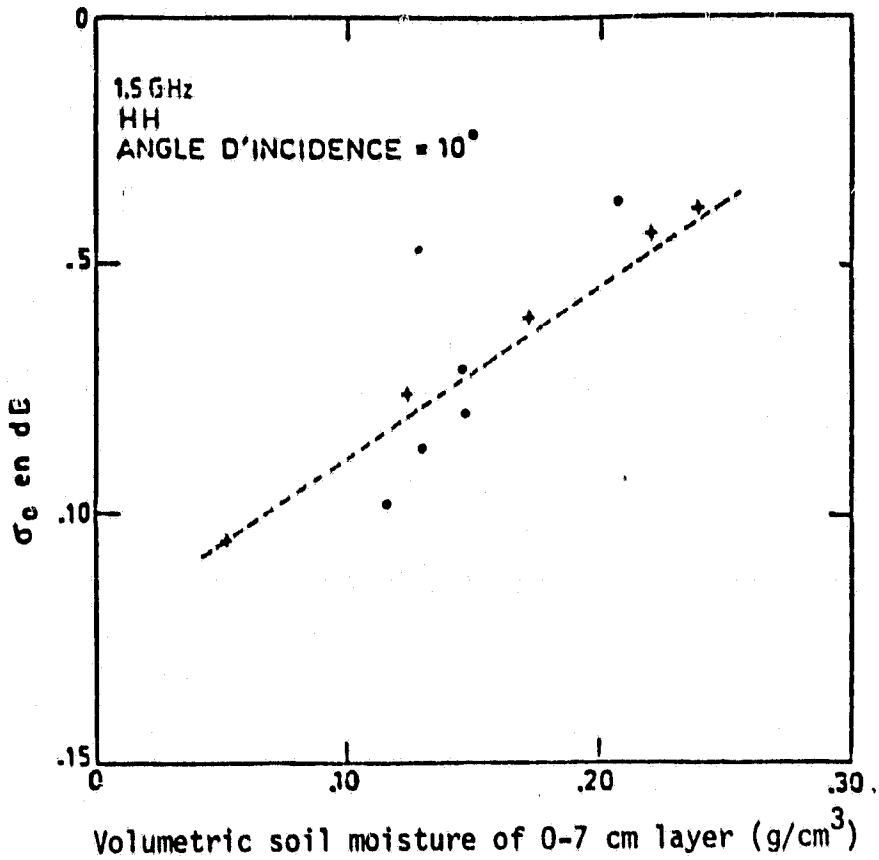

(a)

Figure 2.4 Variation of σ^o with volumetric soil moisture at (a) 1.5 GHz, (b) 3 GHz and (c) 4.5 GHz (from Le Toan et al. [8]).

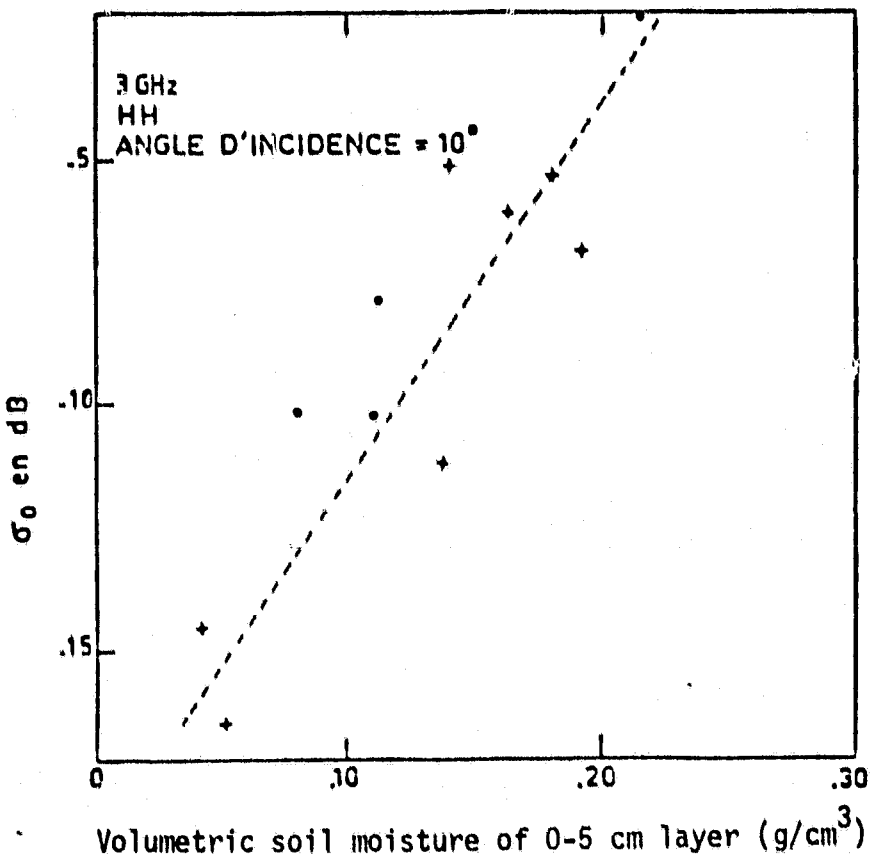

(b)

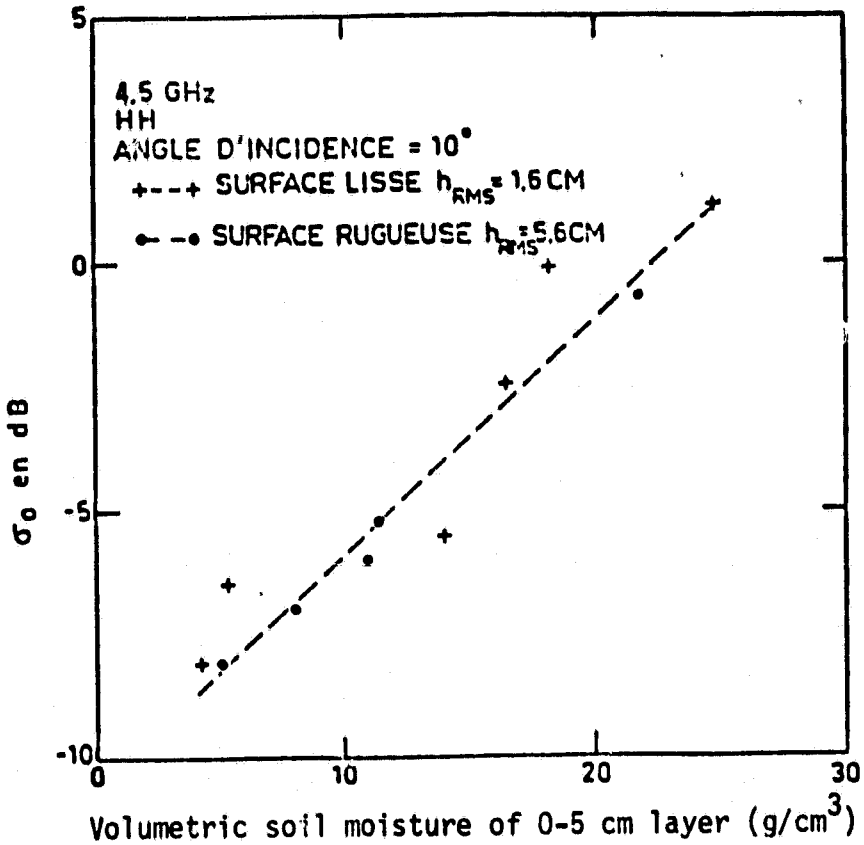

(c)

superimposed on which is the small-scale roughness discussed in the previous section. For rectangular fields with parallel rows, the periodic pattern is unidirectional exhibiting a repetitive spatial modulation function in the direction perpendicular to the row direction. For fields planted in circular rows, the spatial modulation function is a function of r, the distance from the center of the field.

The effect of periodic patterns on σ^o has been examined by three experimental investigations [10, 13, 18]. These investigations were performed for two classes of periodic patterns; the observations reported by Ulaby and Bare [13] are for row spacings and depths that are typical of dry-land farming practices, whereas the other two investigations [10, 18] are for comparatively deeper rows that are typical of irrigated-field conditions. Since the present study is based on conditions for a test site in eastern Kansas, where irrigation is seldom used, the results obtained by Ulaby and Bare [13] will be examined first.

Although the Ulaby and Bare [13] study was conducted for fields planted in wheat, soybeans, and corn, experimental evidence has shown that at frequencies below 8 GHz, the vegetation cover exercises a minor effect on σ^o at angles in the 0° - 20° range. Two types of periodic patterns were observed. The corn and soybean fields were characterized by a row spacing of 90 cm and a row height (trough to peak) of 6 cm, while the wheat fields had 15-cm row spacing and 2-cm row height. The difference between $\sigma^o_{\perp}$(dB) and $\sigma^o_{//}$(dB), corresponding

to observations with the look direction orthogonal and parallel to the row direction, respectively, has been named the look-direction modulation function, M(dB). Figures 2.5 - 2.7 show M(dB) as a function of angle for HH, HV and VV polarization. For the two frequencies shown, it is observed that M(dB) is much higher at 1.1 GHz in comparison to 4.25 GHz. Furthermore, generally HV polarization appears to be considerably less sensitive to look direction than the like-polarized configurations. On the basis of this study, it was concluded that for soil moisture determinations, the look-direction ambiguity problem may be avoided by operating at frequencies higher than 4 GHz with HH polarization, or at any frequency with HV polarization. It should be emphasized that these conclusions pertain to the periodicities and row depths investigated in the above study, which are typical of dry-land farming soil surface conditions.

For periodic patterns with deeper rows, σ° was observed to be sensitive to look direction (relative to row direction) at 1.6 GHz, 4.75 GHz and 13.3 GHz [10, 18]. Figures 2.8 and 2.9 show plots of M(dB) as a function of θ for HH and VV polarizations, based on airborne scatterometer data acquired by NASA/JSC [10]. It is observed that the location of the peak is independent of the frequency and that the magnitude decreases with increasing frequency. These results are in agreement with theoretical model predictions [21]. Another set of row-direction data is shown in Figure 2.10 for a wheat stubble field [18]. Large differences are observed between $\sigma^{\circ}_{\perp}$ and $\sigma^{\circ}_{//}$ for HH polarization at all the frequencies. In contrast, smaller differences are observed for the HV-polarized data. Further discussion of this

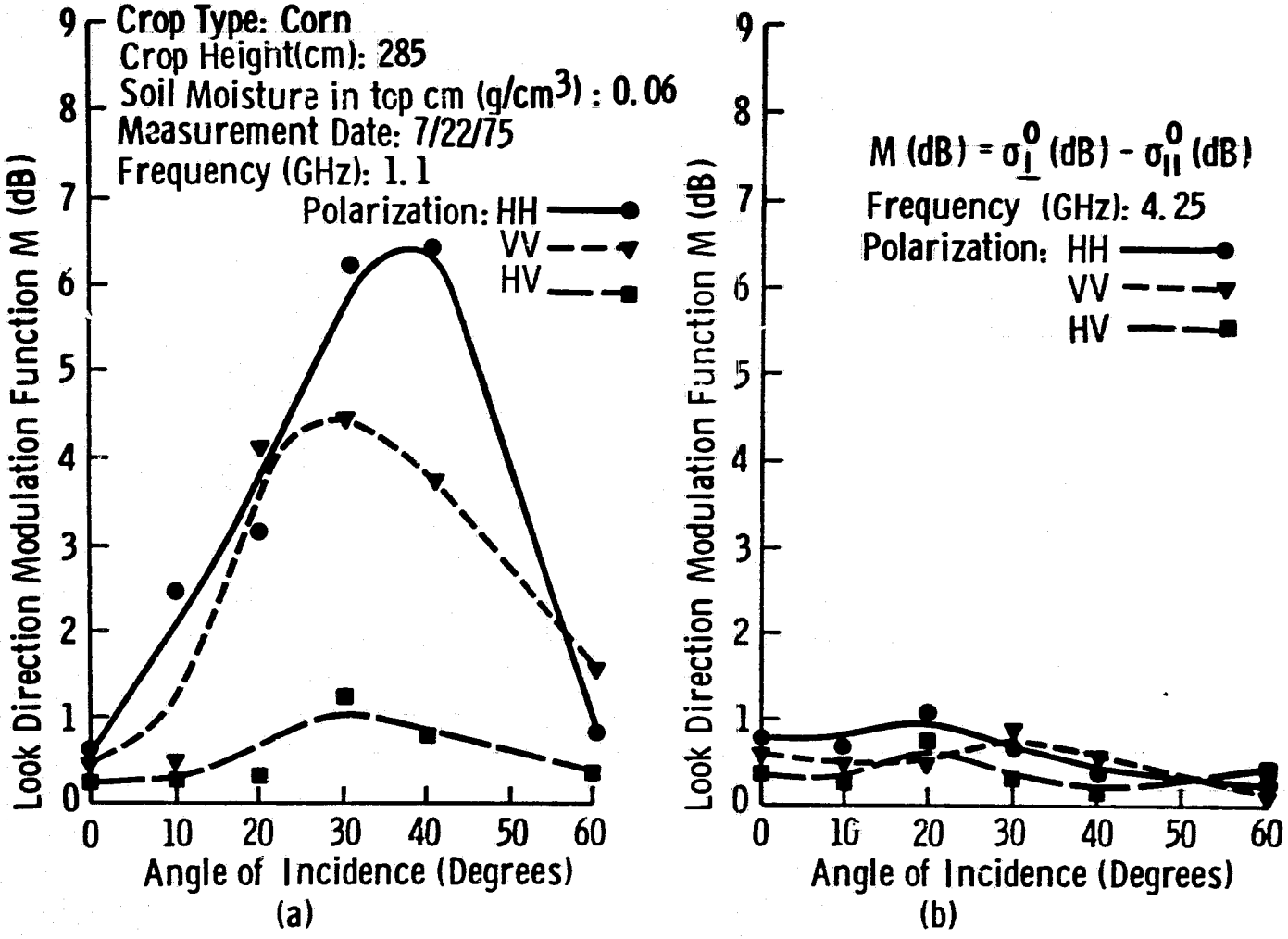

Figure 2.5 Comparison of the angular response of the look-direction modulation function of a corn field for HH, HV and VV polarizations at a) 1.1 GHz and b) 4.25 GHz (from [13]).

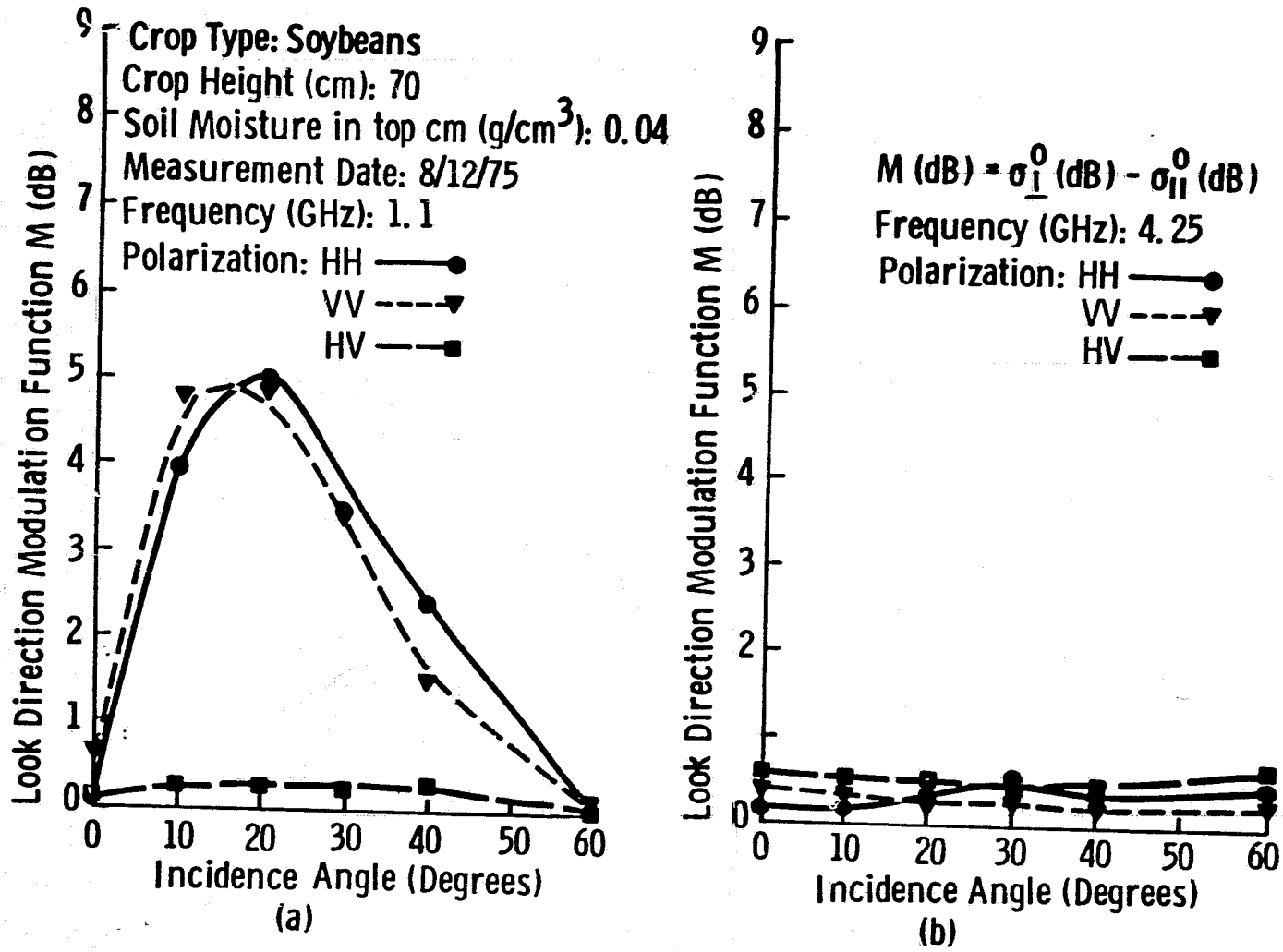

Figure 2.6 Comparison of the angular response of the look-direction modulation function of a soybean field for HH, HV and VV polarizations at a) 1.1 GHz and b) 4.25 GHz (from [13]).

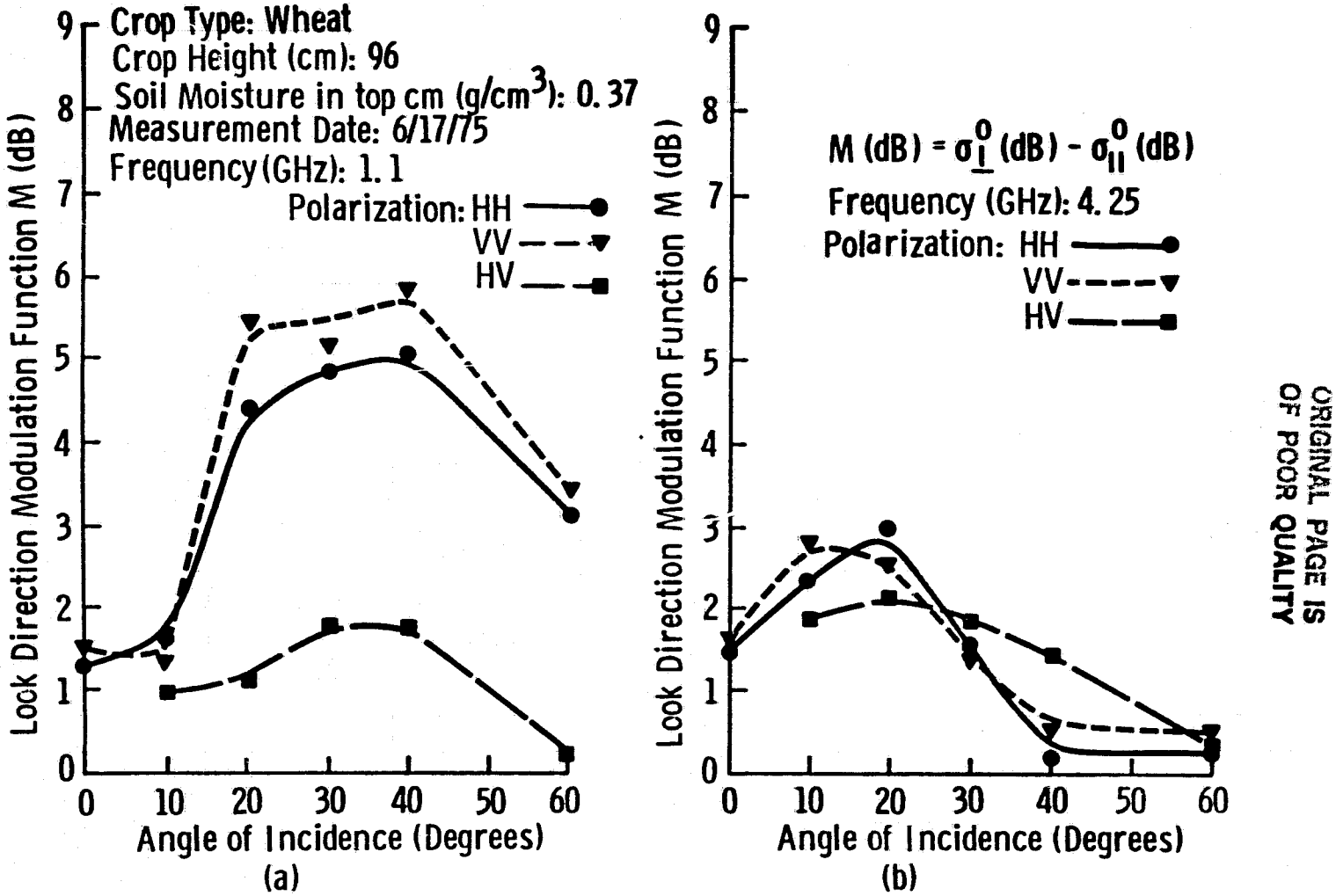

Figure 2.7 Comparison of the angular response of the look-direction modulation function of a wheat field for HH, HV and VV polarizations at a) 1.1 GHz and b) 4.25 GHz (from [13]).

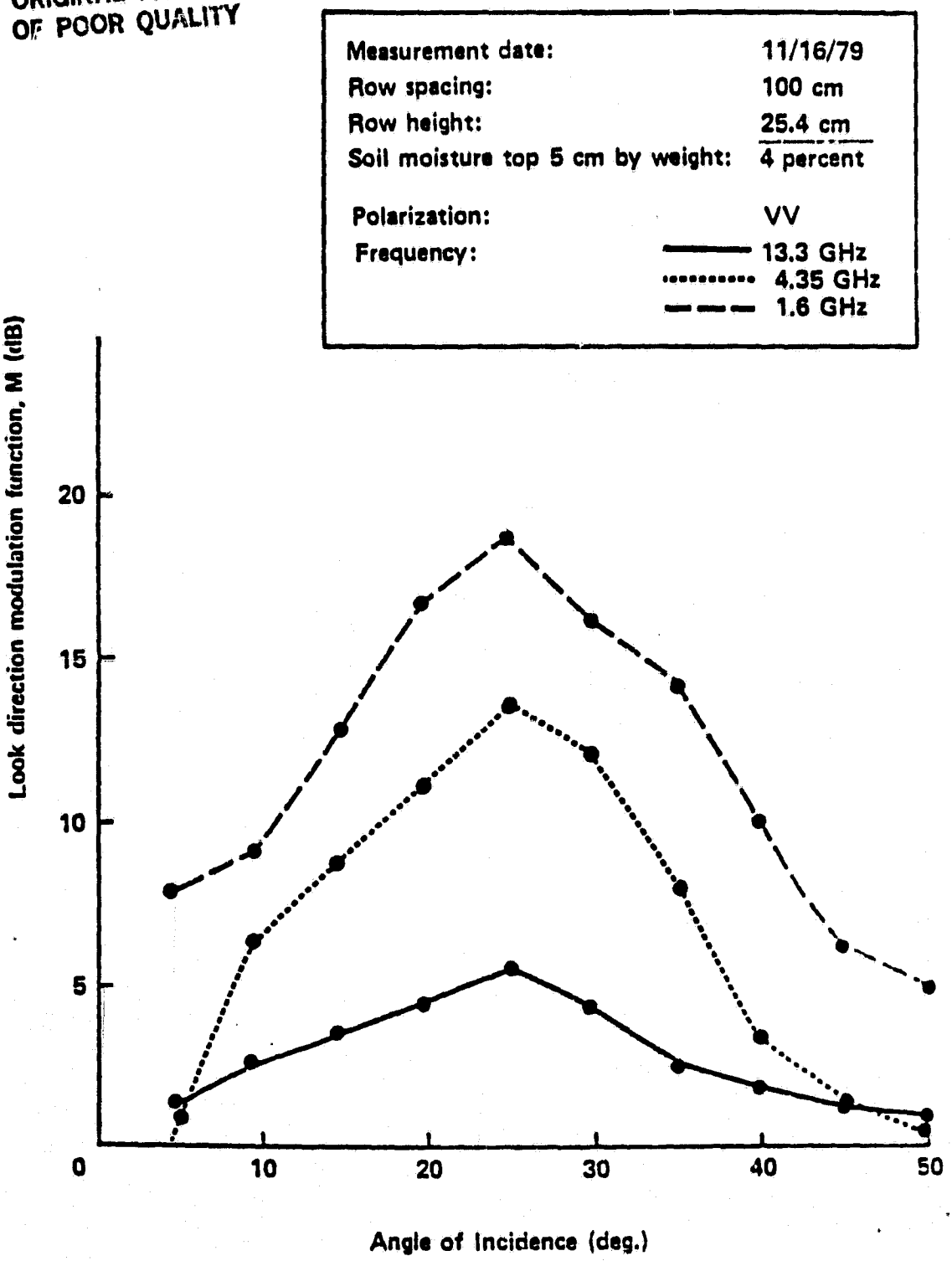

Figure 2.8 Look-Direction Modulation Function as a function of angle of incidence for a row spacing of 100 cm and row height of 25.4 cm (from Fenner et al. [10]).

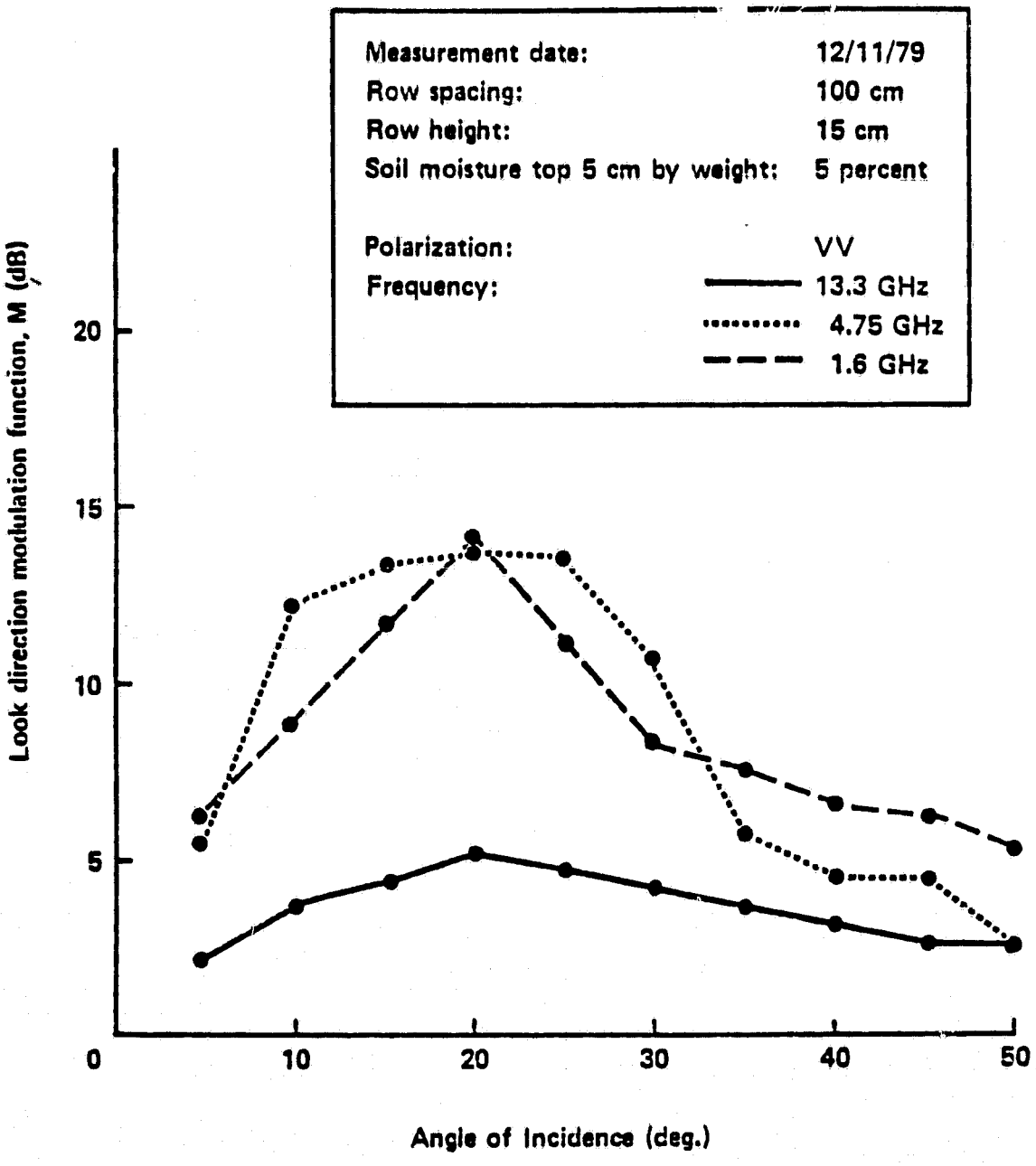

Figure 2.9 Look Direction Modulation Function as a function of angle of incidence for a row spacing of 100 cm and row height of 15 cm (from Fenner et al. [10]).

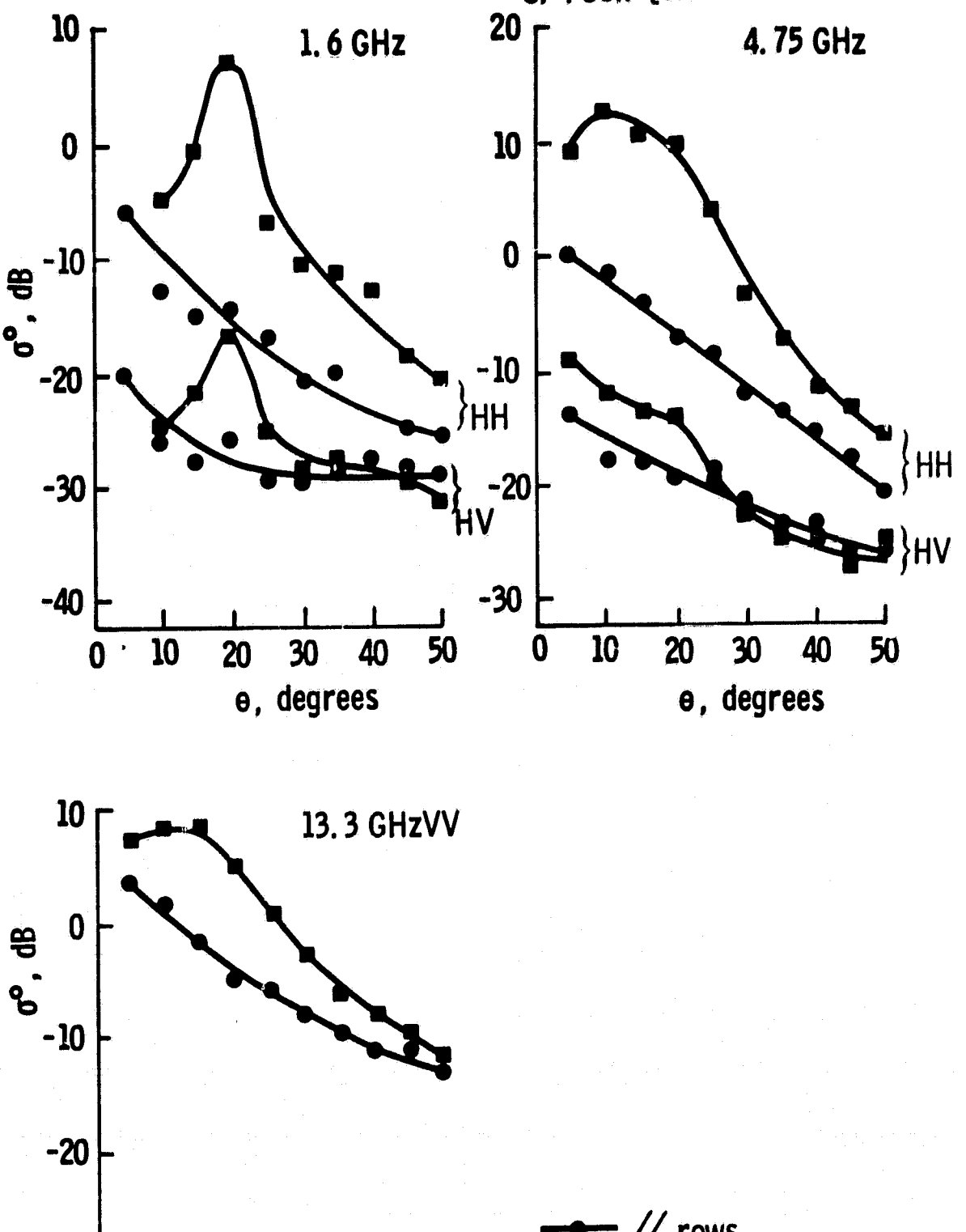

Figure 2.10 Variation of σ° with angle of incidence for a wheat-stubble field, from airborne observation flown in parallel and perpendicular directions relative to row direction. It is suspected that the observed differences between $\sigma^{\circ}_{//}$ and $\sigma^{\circ}_{\perp}$ for HV polarization are not real; the $\sigma^{\circ}_{\perp}$ data are biased due to polarization coupling by the antenna (from [18]).

subject is deferred to Section 2.5 where the composite influence of all the scene variables is considered.

2.3 Soil Texture

Soil texture exercises an indirect, but significant, influence on the sensitivity of σ^o to soil moisture. Experimental measurements indicate that the dielectric properties of soil are dependent on its composition. For a given volumetric moisture content, the real part of the dielectric constant is generally highest for sand and lowest for clay. Figures 2.11 and 2.12 contain a summary of measured dielectric-constant curves for a variety of soils (Table 2.2) at 5 GHz and 1.4 GHz. Generally, the spread in values due to texture decreases slowly with frequency.

The scattering coefficient σ^o is related to the reflection coefficient, which in turn is governed by the dielectric properties of the soil. Thus, the reflection coefficient of different soil types exhibit different responses to soil moisture content. This is illustrated in Figure 2.13 for 1.4 GHz (based on data reported by Newton [24]). The dependence of σ^o on soil texture is shown in Figure 2.14 [5].

The dependence on soil type may be removed by expressing soil moisture in terms of a tension-related quantity. Schmugge [25] has proposed the use of percent of field capacity, M_{FC}, as a soil moisture indicator where field capacity is the gravimetric moisture content at 1/3-bar tension. Additionally, Schmugge provides an approximate

Table 2.2 Different types of soils used for the dielectric measurements as a function of water content at 1.4 GHz and 5 GHz (from [22].

No.	Soil type	Texture (percent) Sand	Silt	Clay	Wilting[1] point WP (cm^3/cm^3)	Transition[2] moisture W_t (cm^3/cm^3)	γ^+	α^3	Remarks
1	M5	88.0	7.3	4.7	0.034	0.20	0.40	0	Measurement frequency = 5 GHz (Wang *et al.*, 1978)
2	F2	56.0	26.7	17.3	0.115	0.22	0.40	0	
3	H7	19.3	46.0	34.7	0.220	0.31	0.35	0	
4	Harlingen clay	2.0	37.0	61.0	0.358	0.31	0.30	0	
5	Yuma sand	100.0	0	0	0.004	0.17	0.50	0	Measurement frequency = 1.412 GHz (Lundien, 1971)
2	Eufaula fine sand	90.0	7.0	3.0	0.024	0.16	0.50	0	
3	Dougherty fine sand	82.0	14.0	4.0	0.034	0.17	0.50	0	
4	Minco very fine sand	70.0	22.0	8.0	0.051	0.17	0.50	0	
5	Openwood street silt	22.0	70.0	8.0	0.092	0.23	0.50	8	
6	Chickasha loam	58.0	28.0	14.0	0.098	0.22	0.40	8	
7	Zaneis loam	48.0	36.0	16.0	0.114	0.22	0.40	8	
8	Collinville loam	45.0	39.0	16.0	0.115	0.23	0.40	8	
9	Kirkland silt loam	26.0	56.0	18.0	0.137	0.20	0.40	8	
10	Tabler silt loam	22.0	56.0	22.0	0.159	0.19	0.40	8	
11	Vernon clay loam	16.0	56.0	28.0	0.192	0.28	0.45	26	
12	Long lake clay	6.0	54.0	40.0	0.255	0.26	0.40	26	
1	Sand	86.0	7.0	7.0	0.046	0.20	0.40	0	Measurement frequency = 1.4 GHz (Newton, 1977)
2	Samples 4 and 5	40.0	26.0	34.0	0.205	0.30	0.30	22	
3	Samples 7 and 18	36.0	29.0	35.0	0.212	0.28	0.30	16	
4	Samples 14 and 15	52.0	9.0	39.0	0.221	0.30	0.30	18	
5	Sample 13	44.0	12.0	44.0	0.250	0.31	0.30	22	
6	Miller clay	3.0	35.0	62.0	0.361	0.33	0.30	20	

[1]Computed from (1).
[2]Determined from (2)-(5).
[3]Determined from (6).

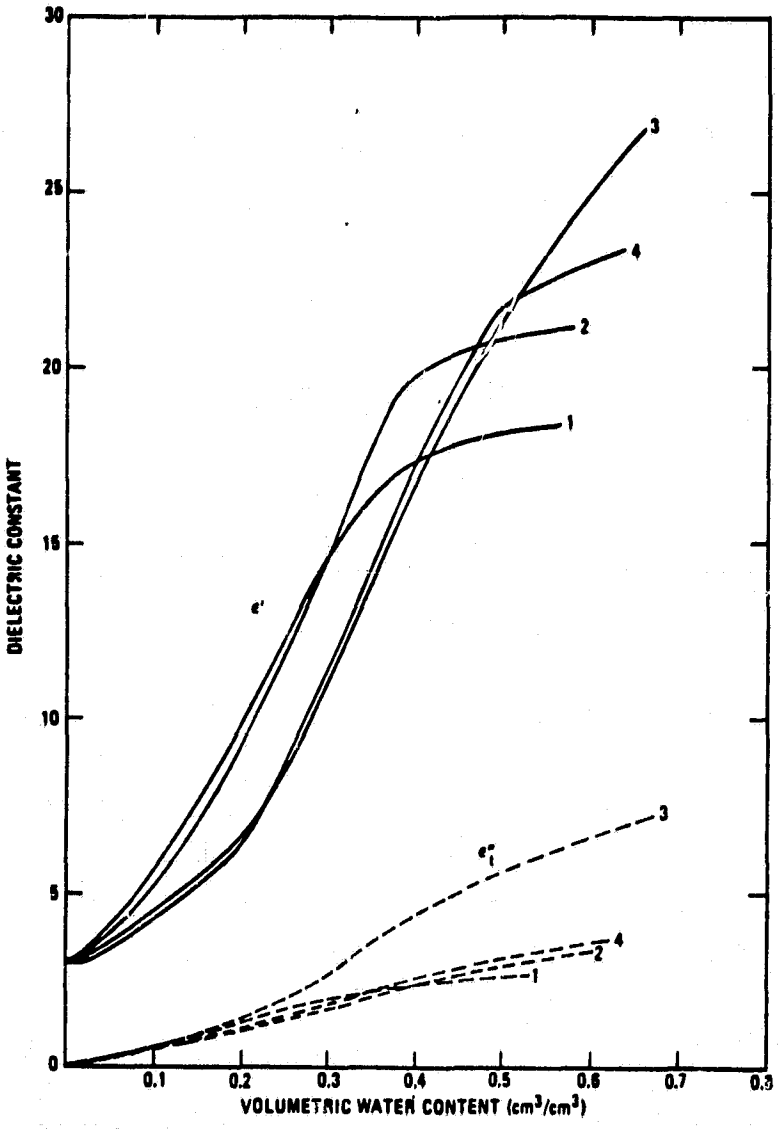

Figure 2.11 Dielectric constant as a function of volumetric moisture content at 5 GHz for the soils listed in Table 2.2 (from [22]).

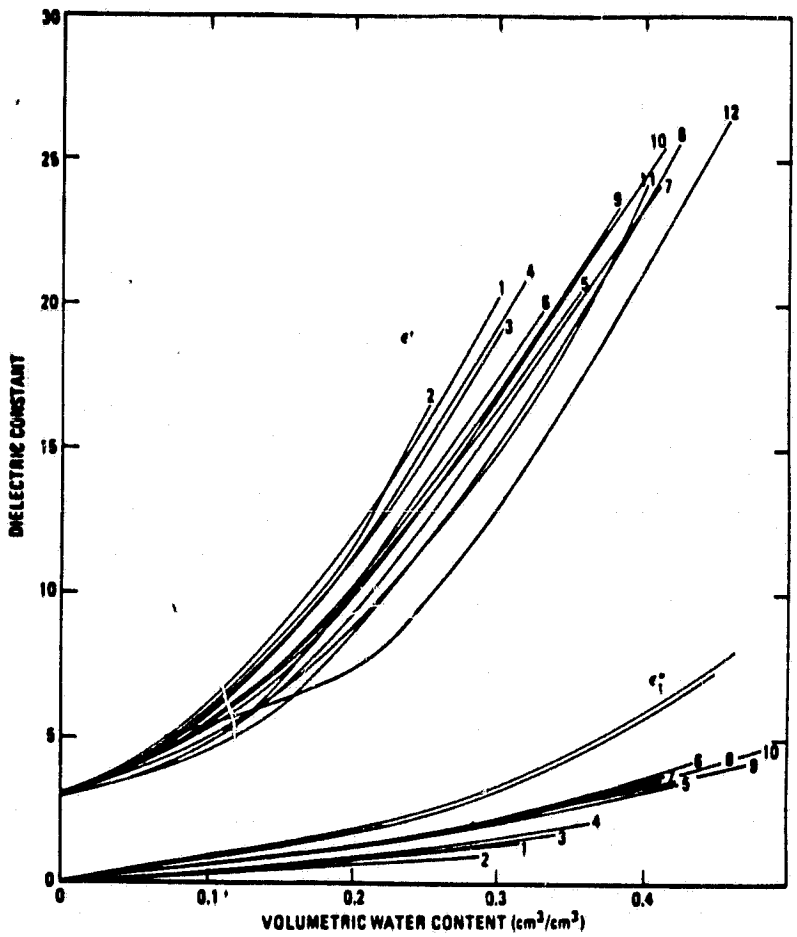

Figure 2.12 Dielectric constant as a function of volumetric moisture content at 1.412 GHz for the soils listed in Table 2.2 (from [22]).

a)

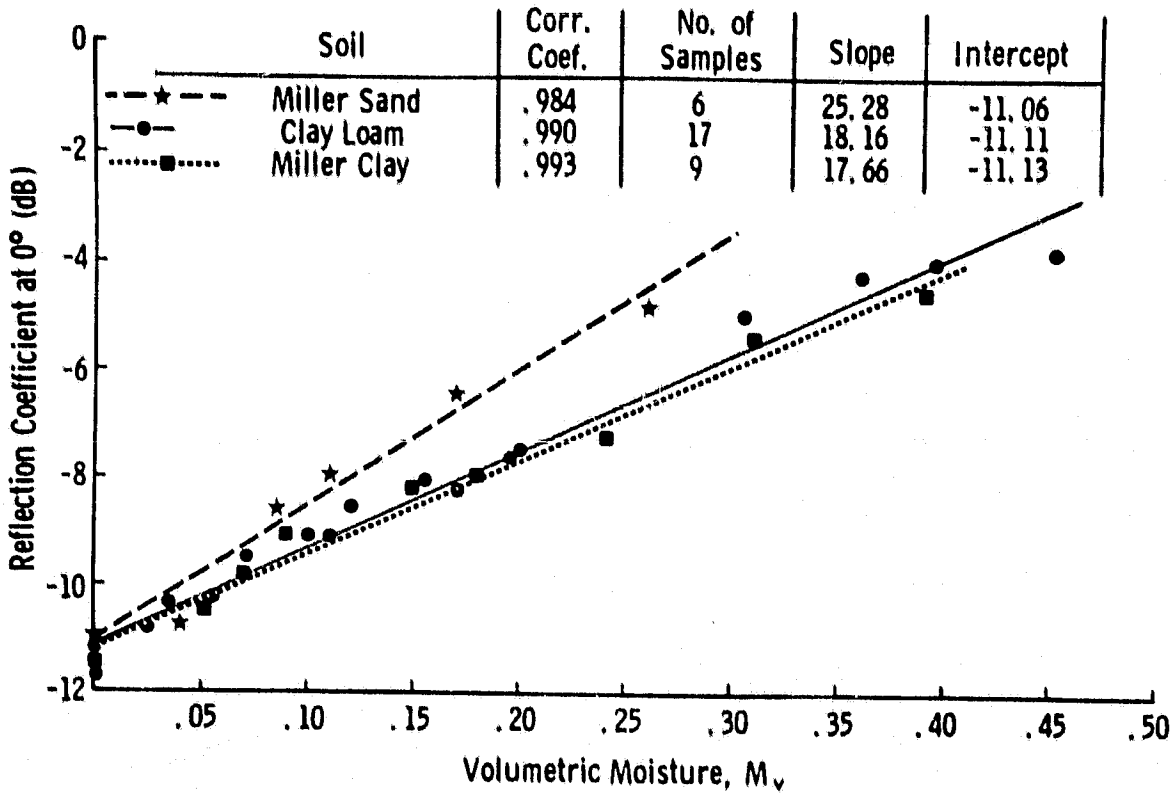

Figure 2.13 Reflection coefficient R(dB) of sand, clay loam, and clay at 1.4 GHz, 0 degrees as a function of volumetric moisture (from [5]).

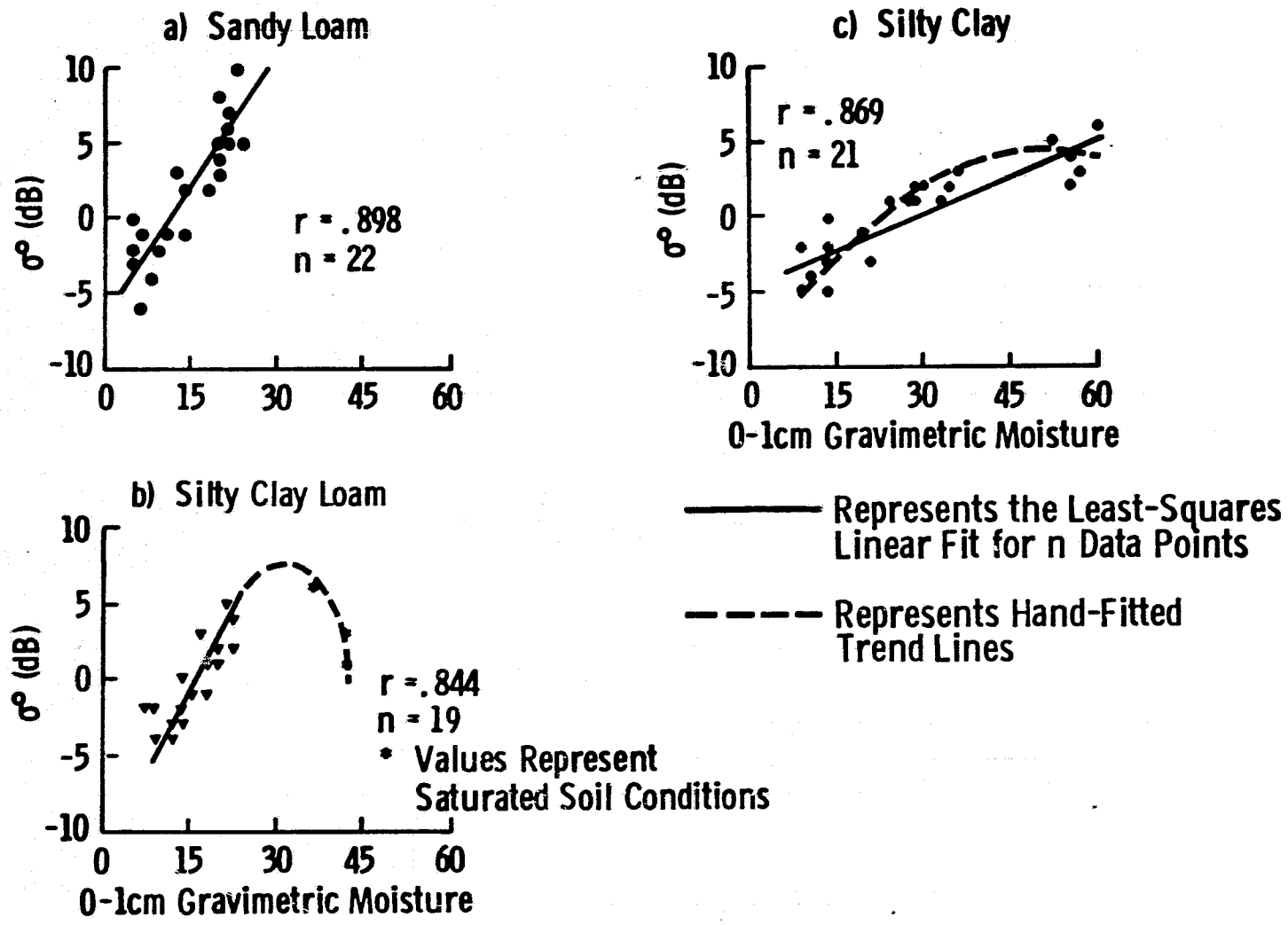

Figure 2.14 Backscattering coefficient at 4.6 GHz, 10 degrees, HH polarization as a function of 0-1 cm gravimetric soil moisture (a) sandy loam, (b) silty clay loam, and (c) silty clay. Saturated soil conditions in the field of silty clay loam are not included in linear regression (from [5]).

expression relating the field capacity to the relative composition of the soil (sand and clay contents).

The impact of soil texture on the sensitivity of σ^o to moisture content was recently investigated by Dobson and Ulaby [5]. Figures 2.15 and 2.16 depict the observed dependence of σ^o on moisture for several different sampling depths, with moisture expressed volumetrically in Figure 2.15 and as percent of 1/3-bar moisture in Figure 2.16. Comparison of the two sets of linear regressions clearly demonstrates the utility of the conversion to percent of 1/3-bar moisture for removing the dependence on soil texture. The overall response to soil moisture is summarized in Figure 2.17, where plots of the linear correlation coefficient between σ^o(dB) and moisture in the top 5 cm soil layer are shown for different soil moisture indicators including gravimetric, volumetric, percent of 1/3-bar moisture, percent of 1-bar moisture and percent of field capacity, where field capacity is estimated on the basis of the expression given by Schmugge [25]. Based on the results of the above study, soil moisture given in future sections is expressed as percent of field capacity, primarily because the majority of data acquired in past years does not include soil-tension-versus-moisture curves, and therefore Schmugge's equation is used as an approximate estimator of 1/3-bar moisture.

2.4 Vegetation Cover

Experimental observations indicate that for angles between nadir and about 20°, vegetation cover exercises a minor influence on σ^o for

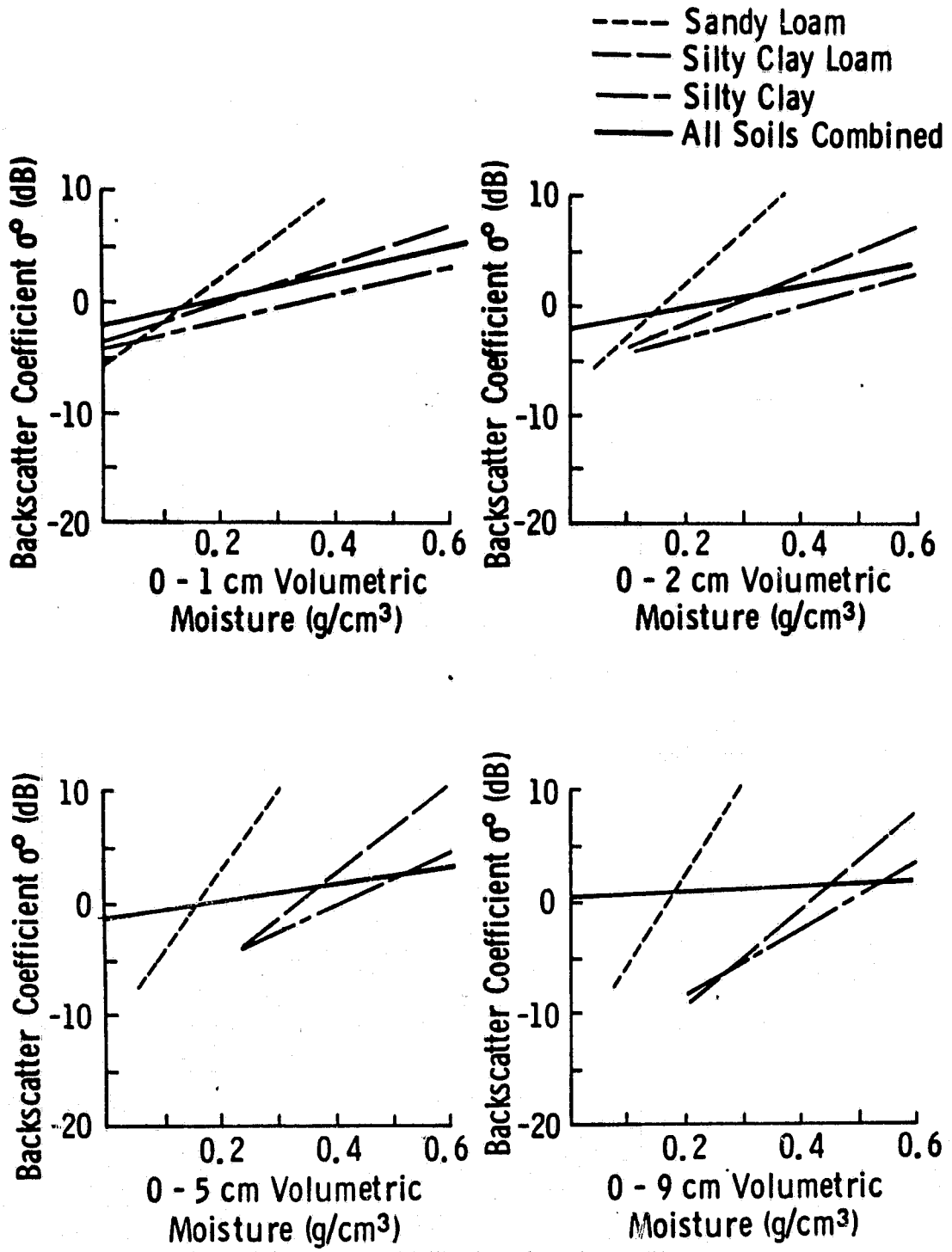

Figure 2.15 Linear regression fits of radar response at 4.625 GHz, 10 degrees, and HH polarization to volumetric soil moisture in the 0-1, 0-2, 0-5, and 0-9 cm layers. Regression results are based on all data obtained for each soil texture and an equally distributed combined texture data base (from [5]).

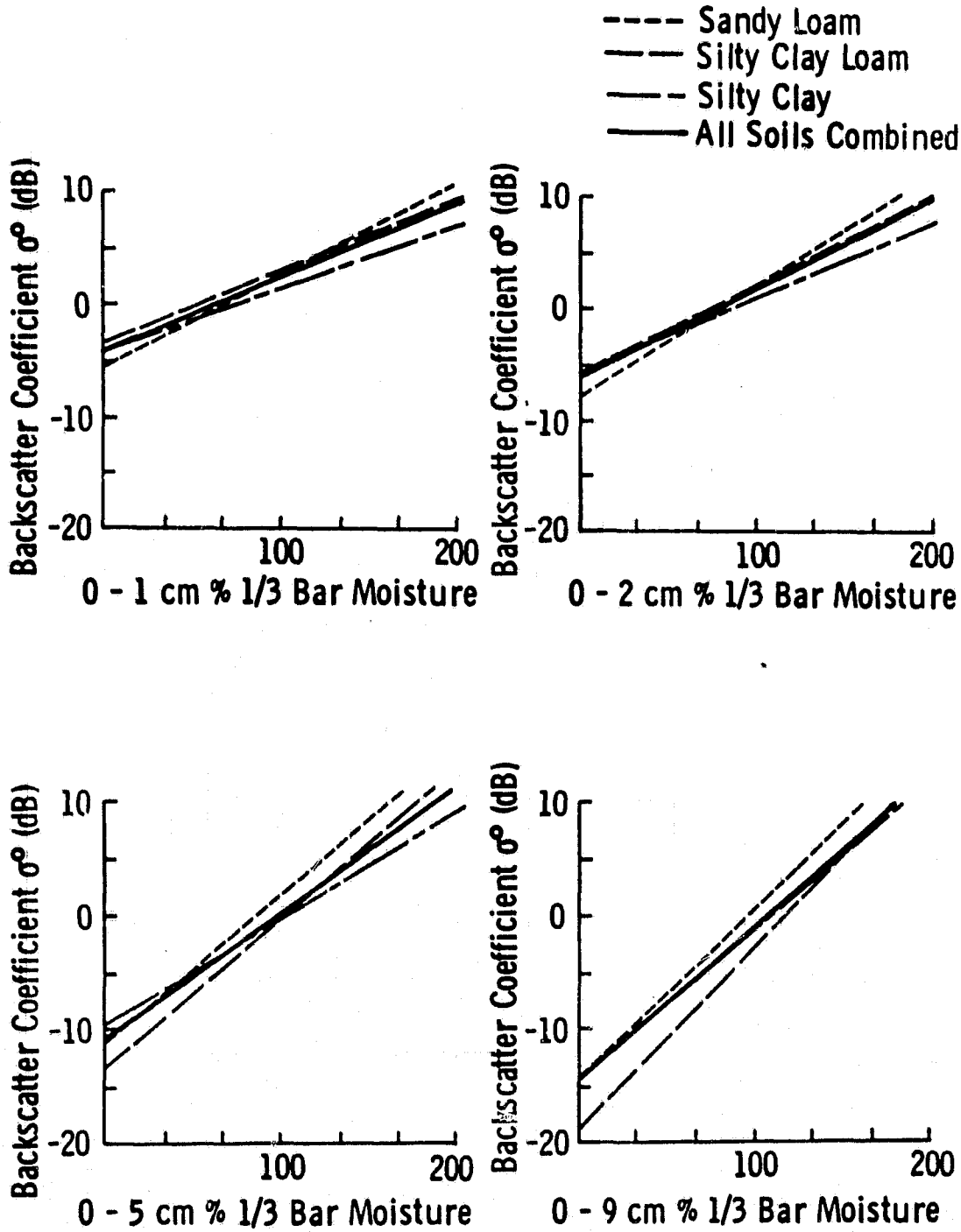

Figure 2.16 Linear regression fits of radar response at 4.625 GHz, 10 degrees, and HH polarization to percent of 0.33 bar water content in the 0-1, 0-2, 0-5, and 0-9 cm soil layers. Regression results are based on all data obtained for each soil texture and an equally distributed combined texture data base (from [5]).

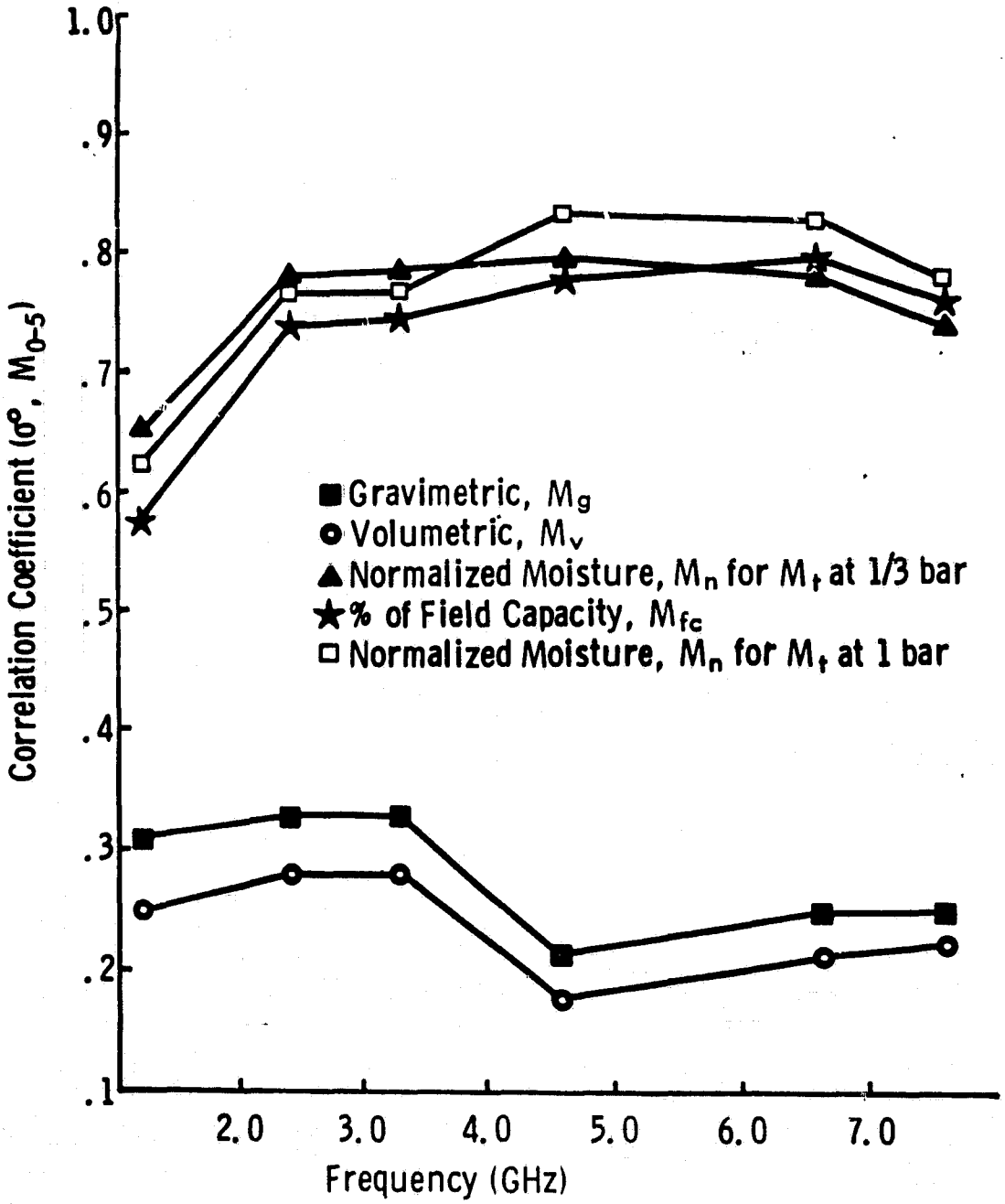

Figure 2.17 Linear correlation coefficient as a function of frequency for various 0-5 cm soil moisture indicators with σ^o at 10 degrees incidence angle and HH polarization. Soil moisture is expressed as gravimetric M_g, volumetric M_v, percent of 0.33 bar moisture, percent of estimated field capacity M_{fc}, and percent of 1.0 bar moisture. Data is from the combined multitexture data base (from [5]).

frequencies below 8 GHz. Figure 2.18 shows σ^o versus M_{FC} for fields of corn, wheat, milo and soybeans, observed by the University of Kansas MAS system at 4.25 GHz, and Figure 2.19 is a scattergram containing 324 measurements acquired by the MAS system over a three-year period, of which 181 points are for bare fields and 143 points are for vegetation-covered fields. It is observed that the slope of the bare regression line is slightly higher than that of the vegetation regression line, which is attributed to the slight attenuation by the vegetation cover.

Further verification of the above "apparent" independence of vegetation cover was obtained from airborne scatterometer data. Figure 2.20 shows σ^o versus M_{FC} for 29 vegetation-covered fields and 21 bare fields as observed by the 4.75 GHz C-130 scatterometer. The data include only fields with no row-periodicity and fields with row periodicity that were observed in a direction parallel to the row direction.

2.5 Composite Effects of Scene Parameters

The 50 fields of Figure 2.20 are treated as a single category in Figure 2.21. In addition, separate regression lines are shown for wheat stubble fields and for non-wheat fields observed with the look-direction orthogonal to the row direction. The reason for separating wheat stubble from the other fields is that the row spacing was 30 cm

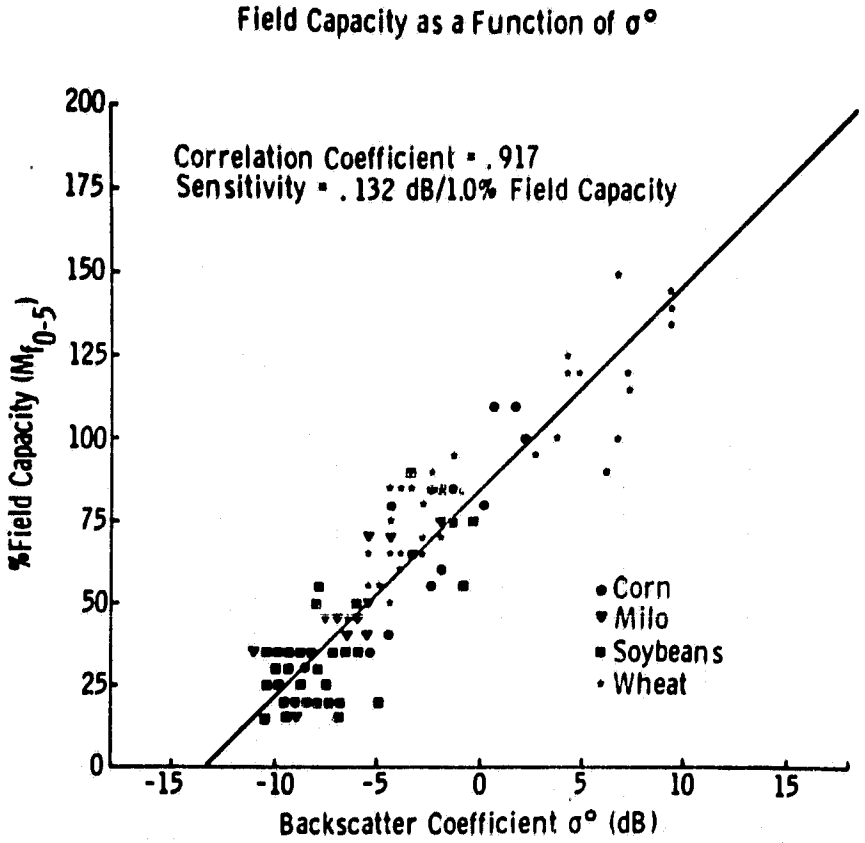

Figure 2.18 Soil moisture content in percent of field capacity as a function of σ^{o}(dB) at 4.25 GHz, θ = 10° and HH polarization (from [14]).

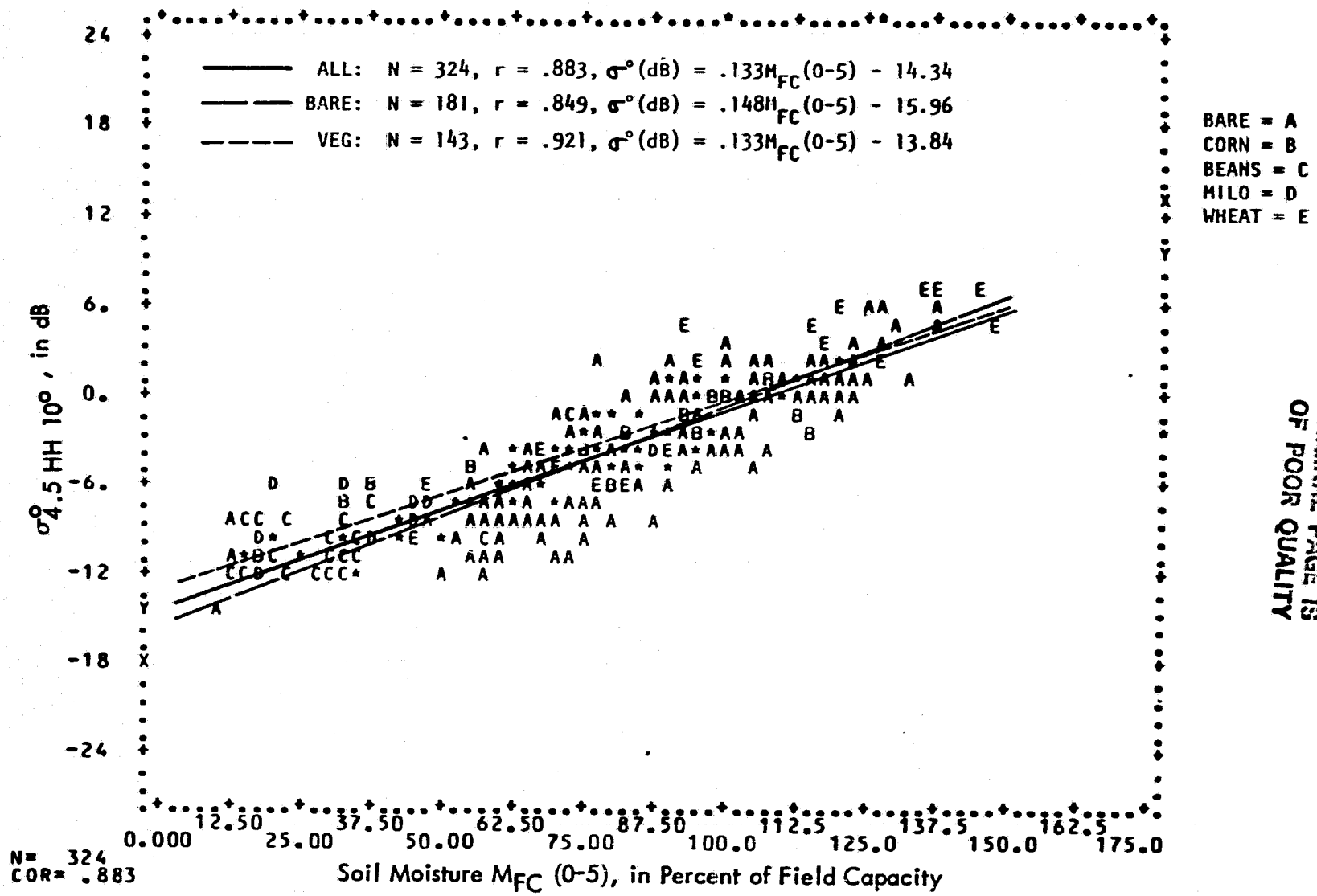

Figure 2.19 Radar backscatter response to soil moisture for bare fields, vegetation-covered fields, and both types combined.

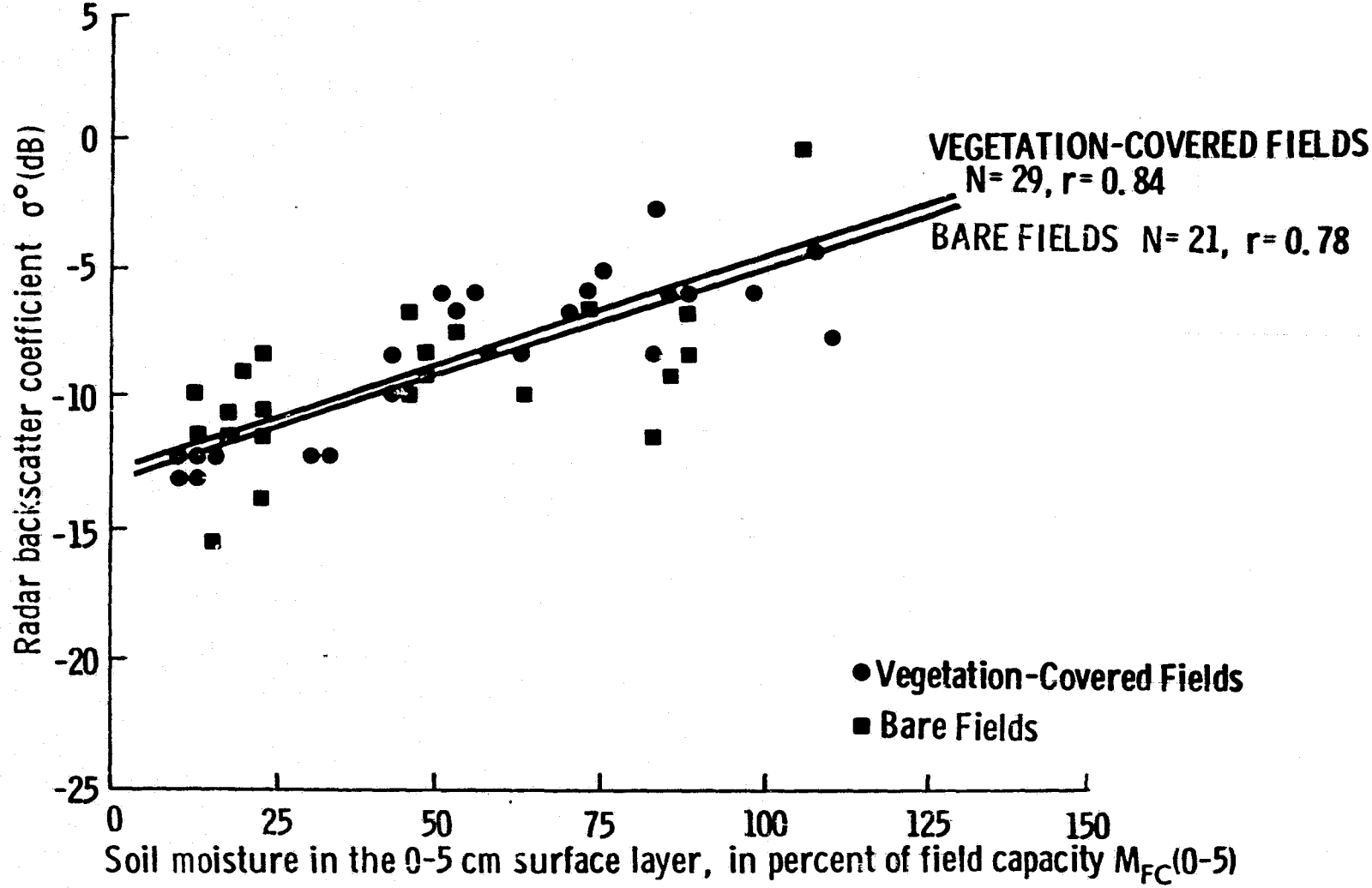

Figure 2.20 Radar backscatter response to soil moisture based on airborne measurements at 4.75 GHz, θ = 10° and HH polarization (from [18]).

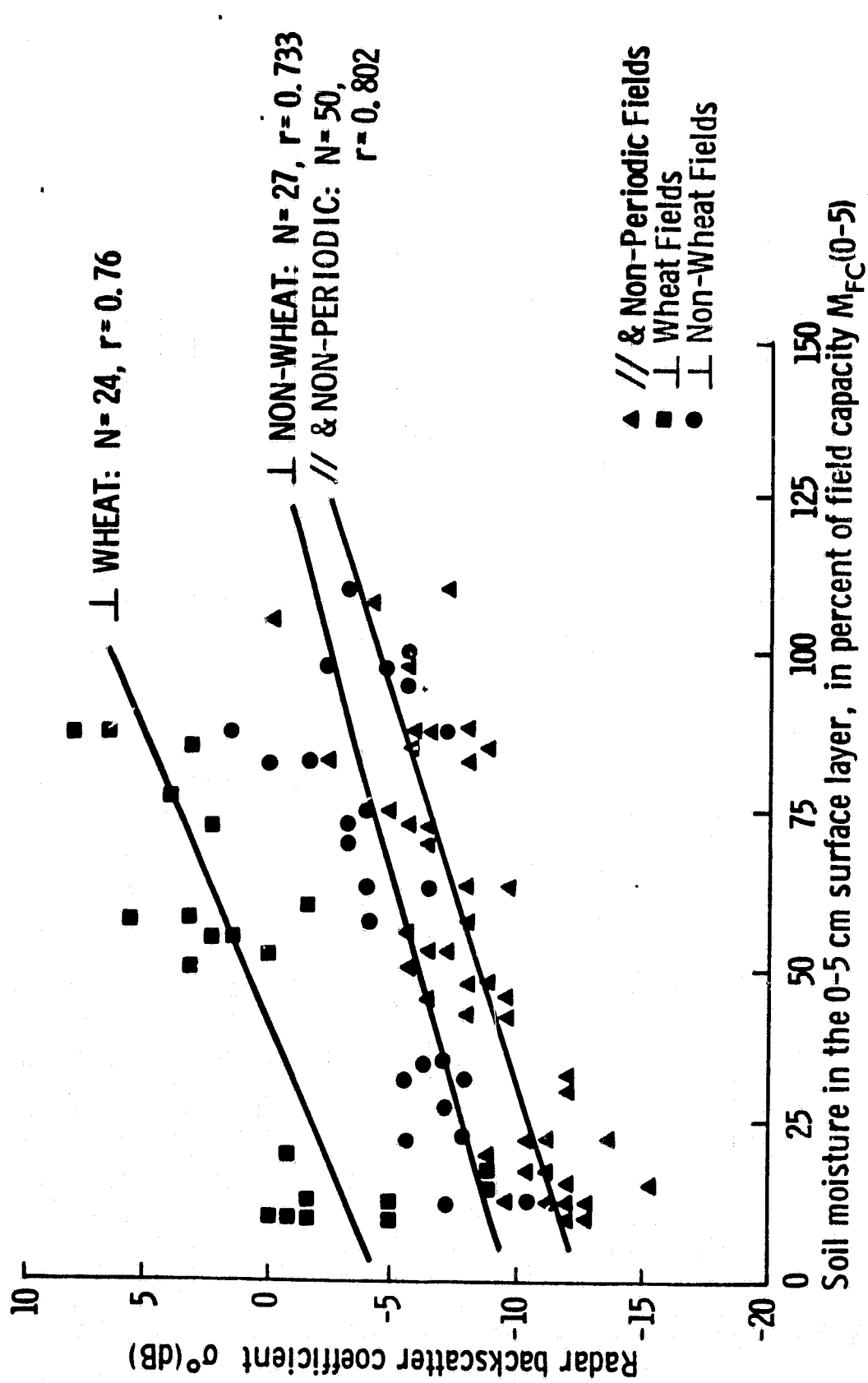

Figure 2.21 Variation of σ^{o} with percent field capacity for different covers, at 4.75 GHz, HH polarization and $\theta = 10°$, (from [18]).

and the row depth was 5 - 8 cm for the wheat stubble fields, in contrast to the non-wheat fields whose periodicity and row depth were typically around 80 cm and 7 - 12 cm, respectively. As expected, the different row structures resulted in different regressions.

Evaluation of the row-direction effect on the relationship between σ^o and M_{FC} is shown in Figure 2.22, where angular plots are given of three parameters: (a) correlation coefficient between σ^o and M_{FC}, (b) sensitivity of σ^o to M_{FC} (slope of regression line) and (c) Y-intercept (value of σ^o(dB) at M_{FC} = 0). Ideally, one would like to see the three sets of curves--representing parallel (//) look direction, $\perp$ look direction for wheat, and $\perp$ look direction for non-wheat--identical for all three parameters. Unfortunately, this is not the case for HH polarization. However, this ideal situation is almost a reality for HV polarization (Figure 2.23).

2.6 Summary of Sensor-Configuration Selection

Based on the previous sections, the following conclusions are reached:

a) To minimize the effects of vegetation cover on the radar response to soil moisture, angles below 30° and preferably below 20° should be used.

b) In the absence of periodic row patterns, the following configuration appears to provide optimum performance with regard to sensing soil moisture content: (a) frequency: 4-5 GHz, (b) angle of

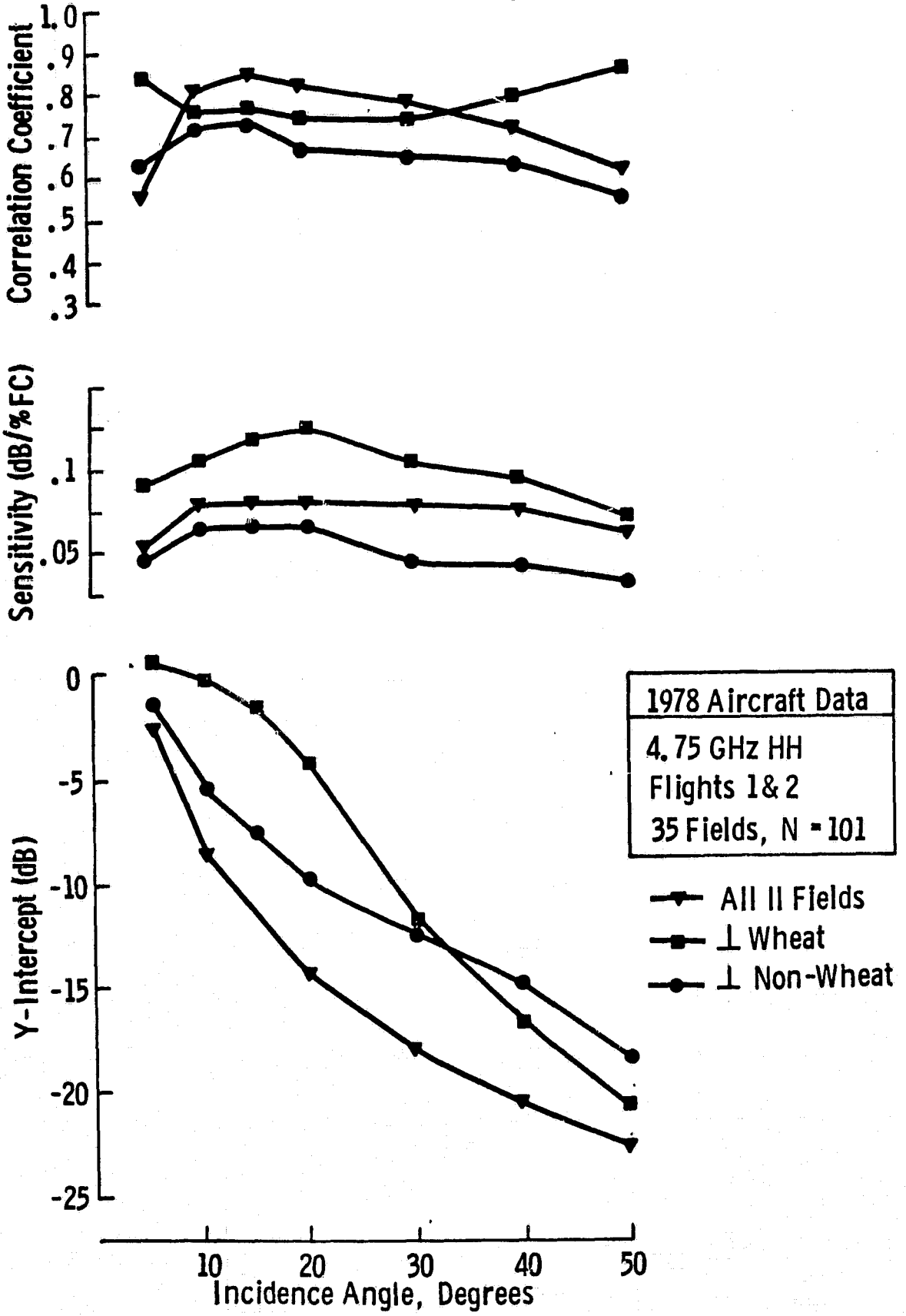

Figure 2.22 Correlation coefficient, sensitivity and Y-intercept for linear regression of σ^{o}(dB) against percent field capacity, at 4.75 GHz, HH polarization (from [18]).

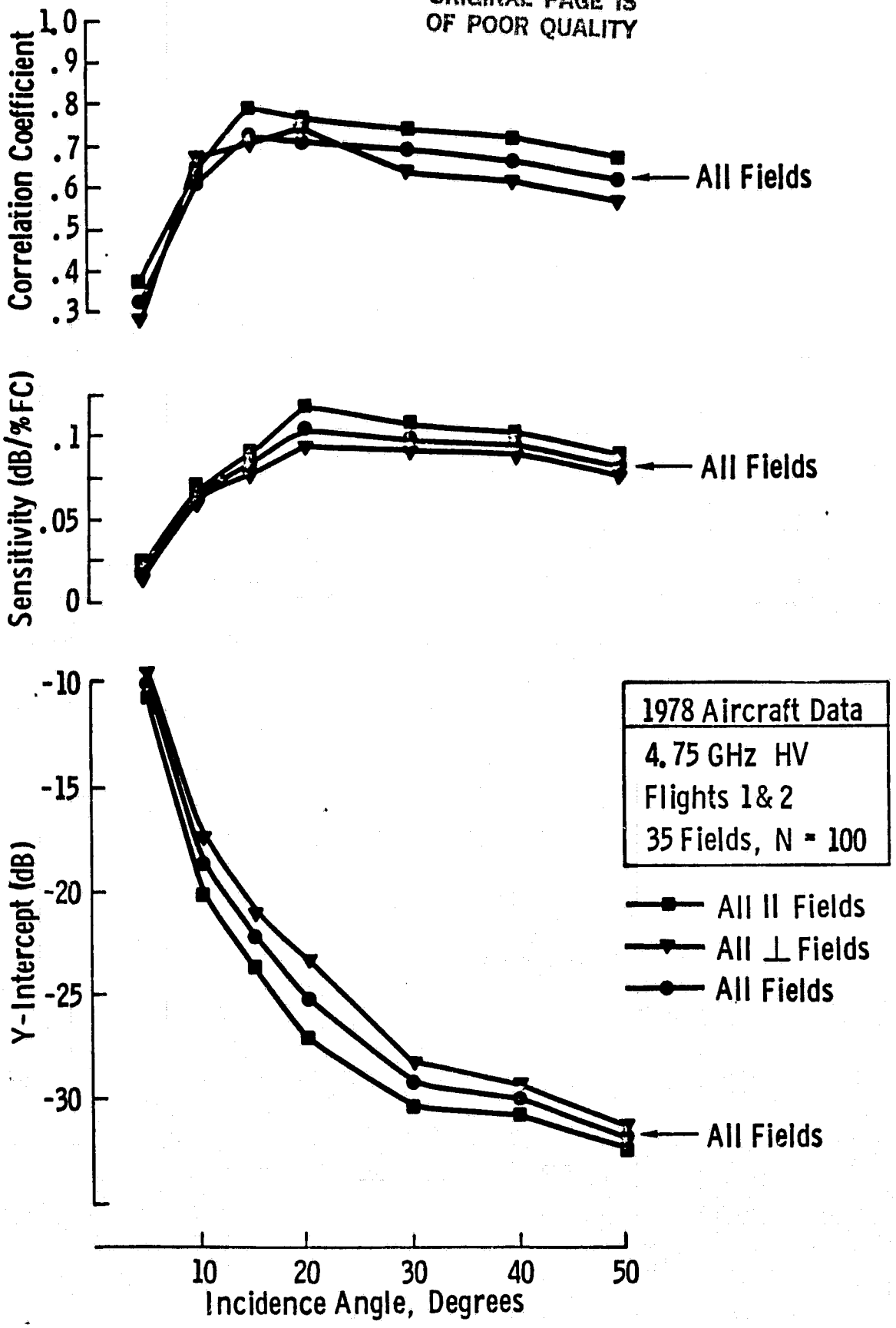

Figure 2.23 Correlation coefficient, sensitivity and Y-intercept for linear regression of σ^{o}(dB) against percent field capacity, at 4.75 GHz, HV polarization (from [18]).

incidence range: 10-20°, and (c) polarization: HH. On the average, the moisture being sensed is that contained in the top 5 cm layer, and the moisture content is expressed as percent of field capacity of that layer.

c) If periodic patterns are present and if the row-depth-to-period ratio is smaller than about 1/10, σ^{o} is approximately insensitive to look direction for frequencies higher than 4 GHz, and therefore the configuration given in (b) may be used, although some improvement in correlation to moisture may be obtained by operating with HV polarization instead. The above row-pattern characteristics are typical of conditions that prevail during most of the growing season in dry-land farming regions.

d) In regions where irrigation practices are common, row-depth-to-period ratios may be as high as 1/4, in which case the variation due to look direction becomes very large, thereby introducing ambiguities in the estimated value of soil moisture. In this case, HV polarization should be used because of its weaker sensitivity to look direction (in comparison to HH polarization).

3.0 SYSTEM CONFIGURATION STUDY

3.1 Introduction

Imaging radars for soil moisture determination may take on several different configurations depending upon the resolution needed. A major purpose of this study is to determine the resolution required and, consequently, its impact on radar system parameter selection.

Should fine resolutions be required, no alternative to the nearly fully focused synthetic aperture radar (SAR) exists. On the other hand,

as the required resolution becomes coarser, the options available to the system designer increase. Various forms of partially focused and unfocused SAR may be used. When the resolution requirement is coarse enough, one may consider using a real-aperture sidelooking radar (RAR). A "RAR" is much easier to build than is a "SAR," so this option must be examined seriously. Furthermore, when the resolution requirement is relatively modest, one may consider a combined microwave radiometer and scanning synthetic aperture radar (RADISAR). The resolution for the radar can be of the order of hundreds of meters, whereas that for the radiometer will be a few kilometers or tens of kilometers, but the SAR picture is embedded within the radiometer cell so that the two may be used jointly for the soil-moisture determination.

As the resolution requirement is tigntened, the required power, data rate and processing complexity for the radar all increase. The power required for the RAR is usually quite small at the swath-width that one uses for soil-moisture determination. The power required for a partially focused or unfocused SAR may also be quite small under these conditions. The power for the RADISAR may be extremely small because the total antenna area may be larger for a RADISAR than for a sidelooking radar that does not scan its beam.

The complexity of the processing for fine-resolution SAR precludes on-board processing. However, for coarser resolution SAR, the complexity is reduced by such a large amount that one may think very seriously about on-board processing, which in turn reduces the required telemetry rate to an almost negligible level. Therefore, one must examine the resolution requirement extremely carefully and determine from this whether the advantages for other purposes of fine resolution should be

traded against the advantages of coarse resolution in terms of low power, on-board processing, and low telemetry rate.

In this study a particular spacecraft configuration has been considered as shown below:

Angles of incidence θ:	7° - 22°
Spacecraft height h:	600 km
Frequency f:	4.75 GHz
Wavelength λ:	6.316 cm
Noise figure F:	4 (6 dB)
Signal-to-noise ratio S_n(min):	4 (6 dB)
Loss factor α:	2 (3 dB)
Scattering coefficient σ^o(min):	0.008 (-21 dB), @ θ = 22°
Antenna length D:	8.7 m (8.7 m and 15 m for RAR and 5 m for RADISAR)
Antenna radiation efficiency η:	0.75

These values are considered to be reasonable ones for implementation. The value of the scattering coefficient is a bit higher than usually applied in radar design, but with the small angles of incidence and typical land backscatter observed in our ground-based measurement programs, we feel sure that this is an adequate design level.

From the fundamental geometric parameters one can calculate certain other derived geometric parameters that are used repeatedly in the discussion below. These include (Figure 3.1):

Ground swath width S_g:	143 km
Slant swath width R_a:	38.5 km
Antenna pointing angle range δ:	6.39° - 20.02°

These parameters are common to all of the systems considered here, the primary variables being ground resolution in both across-

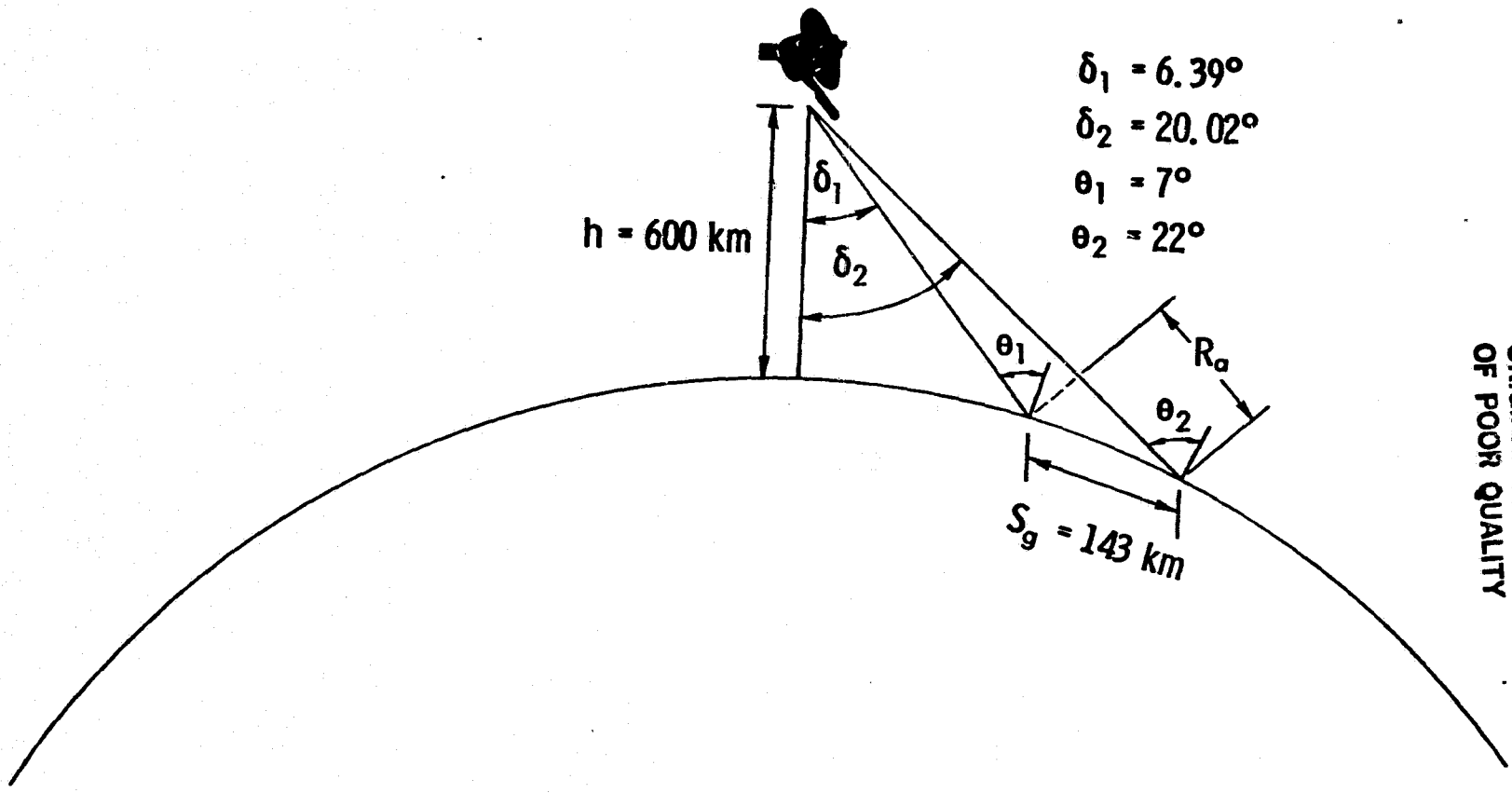

Figure 3.1 Side-looking SAR observing a curved earth from an altitude of 600 km.

track direction r_y and alongtrack direction r_a. The number of independent samples averaged (number of independent looks) N is a very important factor that must be considered in evaluating the performance of a system of this kind. Section 3.2 discusses this matter.

3.2 Equivalent Resolutions

An experiment performed at the University of Kansas some years ago [26] indicated that one can define a resolution volume from which the interpretability of an image can be determined. The experiment involved the use of human interpreters evaluating images for features of significant geographic importance; therefore, one cannot be assured that the same criteria would apply for a measurement system for soil moisture. However, it appears likely that something similar should be applicable; so, lacking this improved description of the usefulness of an image, one can take advantage of the previous study to rate the various simulated images produced in this study.

The most significant conclusions of the referenced study are:

(a) Square and rectangular pixels having the same area are equally interpretable.

(b) A gray-scale resolution can be defined such that it can be used with the alongtrack and acrosstrack resolutions to produce the resolution volume.

The resolution volume is defined as

$$V = r_a r_y r_g = r_e^2 \tag{3.1}$$

where V is the resolution volume, r_a is the alongtrack resolution, r_y is the acrosstrack resolution, r_g is the newly defined gray-scale reso-

lution, and r_e is the pixel dimension of a square pixel of photographic quality having equivalent interpretability. The referenced study found that a numerical measure of the interpretability of an image is related to the resolution volume by an exponential; presumably a similar relation may apply for the soil moisture problem, but, in fact, some of the simulations reported later indicate that the larger resolution volumes may be better for the soil moisture problem.

The gray-scale resolution r_g was defined after considerable experimentation with other measures as

$$r_g = \frac{\text{signal exceeded 10\% of time, } \chi^2(2N) \text{ distribution}}{\text{signal exceeded 90\% of time, } \chi^2(2N) \text{ distribution}} \quad (3.2)$$

That is, the gray-scale resolution is the ratio of the signal level exceeded 10% of the time (brighter pixels) to the signal level for which 10% of the pixels are blacker. Thus it is a ratio of the brightest-to-darkest picture elements in the speckle pattern of the image - a sort of dynamic range for the speckle of the image. One may also think of it, for the soil-moisture problem, as a measure of measurement uncertainty.

When the number of independent samples exceeds about four, a simple expression can be used to approximate r_g:

$$r_g \simeq \frac{\sqrt{N} + 1.282}{\sqrt{N} - 1.282} \quad (3.3)$$

The value of r_g allows one to determine more readily the effect of having a given number of independent samples than one can determine either from the standard deviation associated with that number of samples (standard deviation is not a good measure for a chi-square distribution) or from simply looking at the number N.

The fact that one may obtain equivalent results with a rectangular and a square pixel having the same area means that one may perform trades in the design between resolution in the alongtrack and in the across-track direction, as long as the area of the pixel remains the same. In the referenced study, this was found to hold in farmland and other areas up to a ratio of 10:1 between the length and width of the pixel.

3.3 System Configuration Studies

The three types of systems considered here are the real-aperture radar (RAR), the synthetic-aperture radar (SAR), and the scanning radar-radiometer (RADISAR). Since the simplest system is the RAR, it is considered first, followed by the SAR, for which the most examples are presented, and finally by the RADISAR, for which only one example is given.

3.3.1 Real-Aperture Radar

Figure 3.2 shows the configuration of a real-aperture radar for use in space. The typical real-aperture radar used in aircraft uses a noncoherent pulse transmitter, but the peak power required for such a transmitter is usually too high in space applications thus, a coherent with a pulse-compression scheme ("chirp") must be used. A frequency synthesizer is therefore required to generate coherent local-oscillator and transmitter signals. The coherent transmitter signal is fed to a chirp generator that produces an expanded-length reduced-amplitude pulse. Either frequency-modulation or binary-phase-code modulation may be used for this purpose.

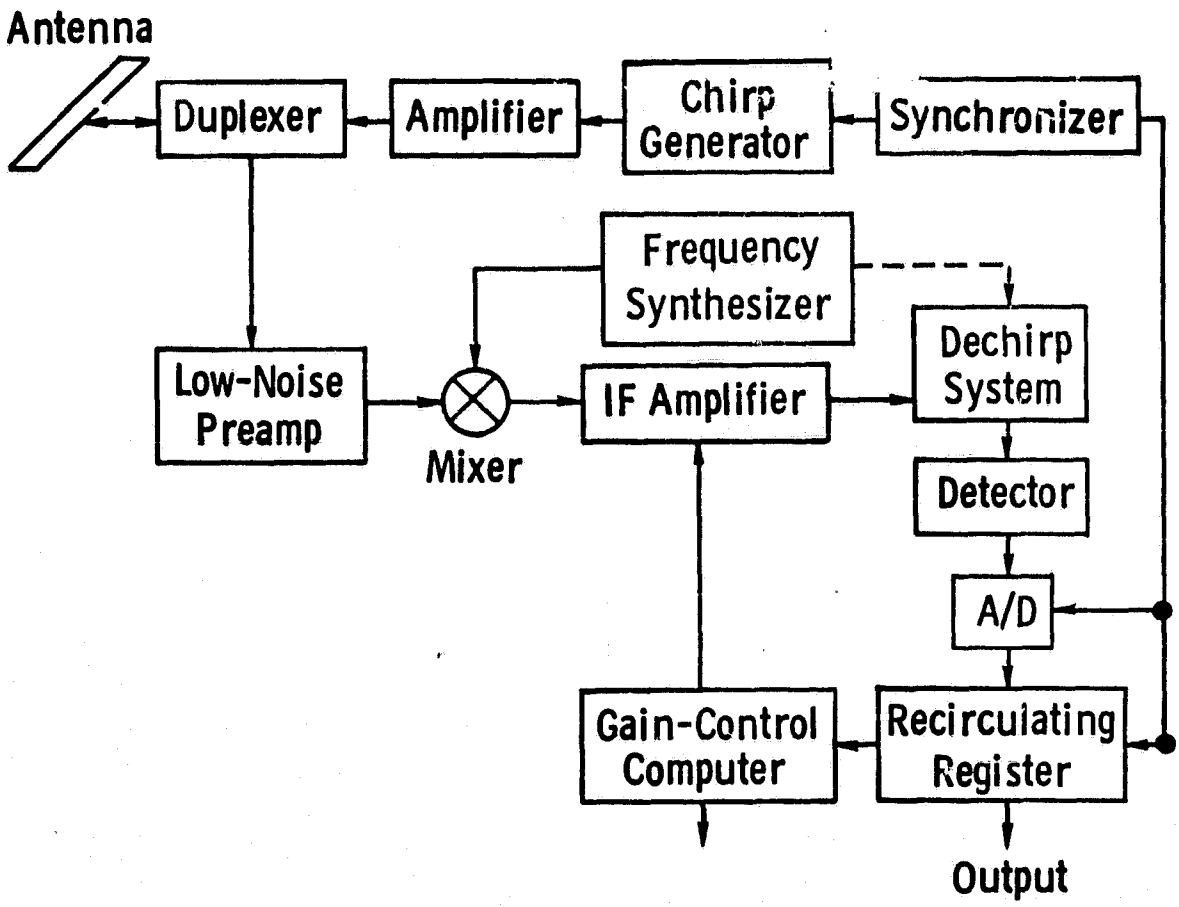

Figure 3.2 Configuration of RAR.

This pulse is then amplified to the required level and fed to the antenna through the duplexer that allows use of a single antenna for transmitting and receiving. The antenna is long and narrow, in this case 8.7 m or 15 m long by 40 cm high (the height determines the swath width of 7° - 22°). The length determines the alongtrack resolution and consequently should be as great as is feasible.

The signal returns to the antenna and is fed through the duplexer to a low-noise amplifier, through a mixer and intermediate-frequency amplifier, to a de-chirping system that converts the signals from the stretched pulse into signals with the appropriate range resolution. This signal is then detected and digitized into a sequence of binary bytes, each of which corresponds to a given range.

The sequence of bytes is fed into a shift register and, as each successive pulse is received, the bytes corresponding to the same range from this and preceding pulses are added by recirculating the signal in the register and adding on a range-element by range-element basis at the input. This register may collect all the signals from the pulses corresponding to a given alongtrack resolution cell with the same amplitude weighting and produce one output for that alongtrack cell. Another configuration recirculates each pulse with a slightly less-than-unity gain, thereby resulting in a continuous output, since the effect of the earlier pulses gradually dies out. The output is used both to feed the telemetry-or recording-system and to feed a gain-control computer.

The gain-control computer may have some reference variation in gain with range that is expected to be typical of the terrain imaged. However, it also uses the output of the recirculating register to pro-

duce an average signal return versus distance curve which can then be used to control automatically the gain of the amplifier so that the average return at each range is the same. Of course, the gain actually used for a particular range must also be telemetered to the ground so that the actual amplitude involved can be established for the measurement of soil moisture.

The form of the radar equation used to determine the average transmitter power is

$$P_t = \frac{8\pi k T_o F S u \beta_v^2 h^3 \alpha}{\eta^2 D^2 \lambda r_y \sigma^o \cos^3 \theta} \tag{3.4}$$

where:

k = Boltzmann's constant

T_o = the reference temperature 290 K

F = the noise figure of the receiver

S = the required signal-to-noise ratio

u = the velocity of the spacecraft

β_v = the vertical beamwidth of the antenna

h = the height of the spacecraft

α = the loss allowance

η = the radiation efficiency of the antenna

D = the length of the antenna

λ = the wavelength

r_y = the acrosstrack resolution

σ^o = the scattering coefficient

θ = the angle of incidence (relative to vertical)

In deriving this equation the following assumptions have been made:

Antenna gain G is

$$G = \frac{4\pi}{\beta_a \beta_v} \eta \tag{3.5a}$$

where β_a is the alongtrack beamwidth.

Pulse repetition frequency PRF is

$$PRF = 2u/D \tag{3.5b}$$

$$\beta_a = \lambda/D \tag{3.5c}$$

$$\text{Bandwidth} = \frac{1}{\text{slant resolution}} \tag{3.5d}$$

Equation (3.4) has been used in determining the required <u>average</u> power in the subsequent tabulations. The peak power required depends upon the duty cycle which, in turn, depends jointly upon the PRF and the amount of pulse compression used. These are independent choices that may be made by the designer.

The number of independent samples potentially available for RAR and SAR and actually available for the RAR has been shown [27] to be

$$N_a = \frac{2r_a}{D} \tag{3.6}$$

An important factor for fine resolution is the rate at which the A/D converter must operate to digitize the range resolution cells. This is

$$\text{A/D rate} = \frac{1}{\tau_e} = \frac{c}{2r_y \sin\theta_{min}} \tag{3.7}$$

where

τ_e = effective pulse-length in seconds (after compression)

c = speed of light

θ_{min} = angle of incidence at the inner edge of the swath, in this case 7°.

Another important quantity for a spacecraft radar is the required telemetry rate (or recording rate if an on-board recorder is used). This is simply the number of pixels per second and is given by

$$\text{telemetry rate} = \frac{R_a u}{r_R r_a} \tag{3.8}$$

where R_a is the slant swath width, and r_R is the slant range resolution ($r_R = r_y \sin\theta$).

3.3.2 Synthetic Aperture Radar

Figure 3.3 illustrates the synthetic aperture radar configuration assumed. The radar itself is a common form; in the processing many options are available and only one is indicated, since only one needs to be shown to illustrate the relative complexity of the different options available.

The signal transmitted is essentially the same as for the RAR shown in Figure 3.2, and the receiver is the same through the de-chirp system, with one exception. Slight variations in velocity or pointing angle of the antenna can cause Doppler frequency shifts that are a problem with SAR. These can be compensated for by adjusting the local oscillator either at the first mixer or at the product detectors shown for the I and Q channels. Hence, a signal from accurate navigation sensors must

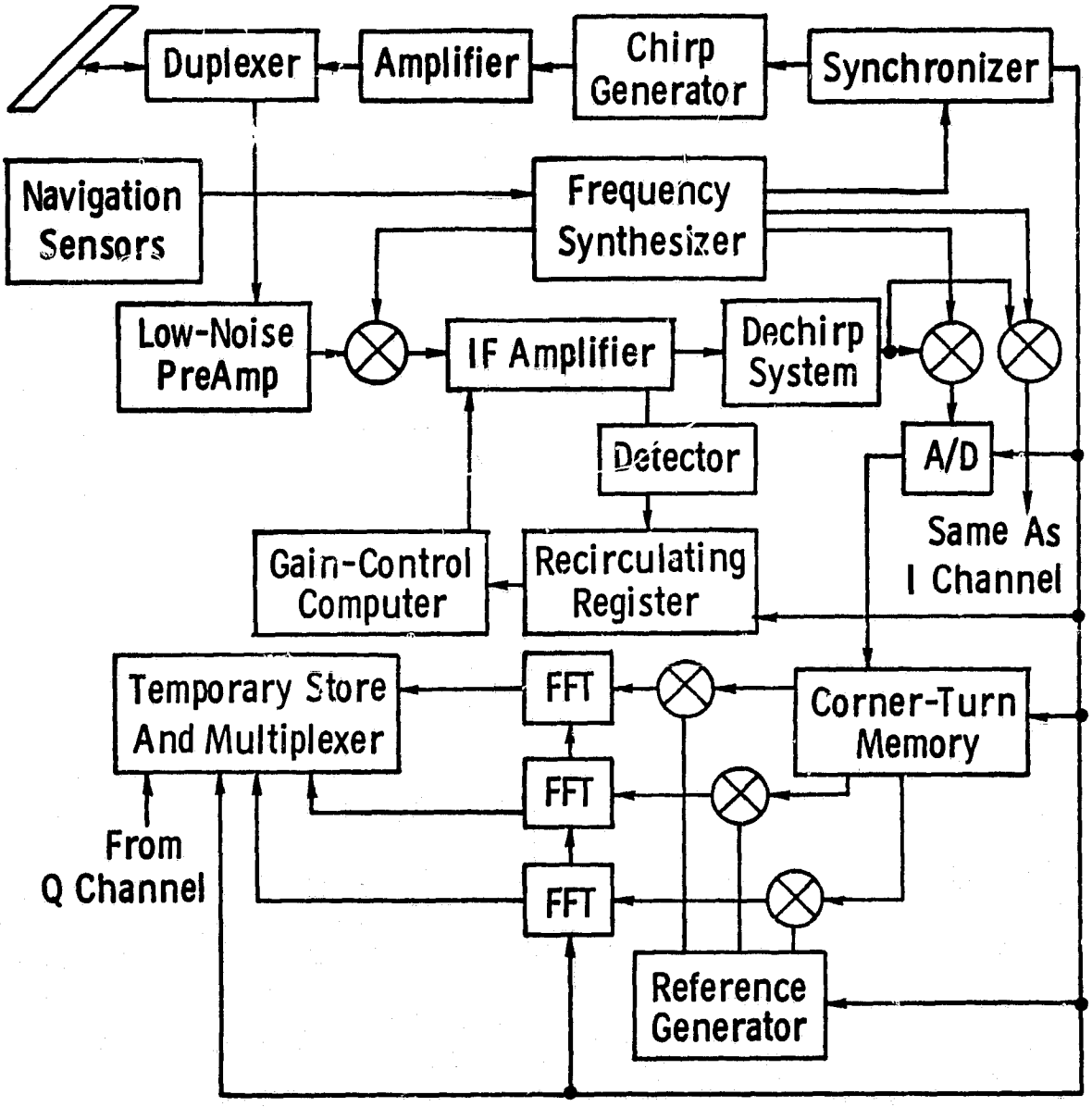

Figure 3.3 SAR configuration assumed.

be fed into the frequency synthesizer. Following the de-chirp system, the synthetic-aperture radar differs from the real-aperture radar. The signal is beaten down to zero by feeding a local oscillator signal at the intermediate frequency into the product detectors I and Q. These represent the in-phase and quadrature components necessary to distinguish positive Doppler frequencies from negative Doppler frequencies in the output. The processor has independent channels from this point on until everything is recombined in the unit at the end, called "Temporary Store and Multiplexer." At this point the in-phase and quadrature components are combined to make a single spectral component corresponding to a particular Doppler frequency which, in turn, corresponds to a particular angle off the side looking direction.

Since the outputs from the receiver are in a range sequence for each pulse, but SAR processing requires an alongtrack sequence at each range, a corner-turning memory is required. This memory is basically a matrix in which the signals are entered in range sequence as each pulse returns, and the signals for a particular range are read out in azimuth sequence. For a focused or partially focused synthetic aperture radar, these azimuth outputs are then mixed with a slowly varying chirp signal that represents the Doppler frequency shift due to motion of the target from a positive Doppler frequency when the target is in the beam through zero, to a negative Doppler frequency as the target leaves the beam. Thus, these mixers in essence amount to correlators between the referenced signals and the individual target "chirps." The output of each mixer is then Fourier-transformed through an FFT computer to produce the equivalent of the output of a bank of filters. Each frequency output at this point corresponds to a

different alongtrack element contained in the beam. A separate mixer and FFT is required for each range element so that the number of FFT computers needed may be very large. However, these computers operate relatively slowly, so configurations may also be established whereby faster FFT computers can be shared among different range channels. For simplicity in discussing the complexity of the processor, we assume that each range channel has its own FFT unit. For an unfocused SAR, no reference function is required.

The outputs of the FFTs are fed to the Temporary Store and Multiplexer that combines the I and Q outputs, as mentioned earlier, and also serves to sort out the returns at the different azimuth angles. This permits superposition of the different independent looks at a particular point on the ground, since these looks are obtained at different times. For example, when a target enters the antenna pattern, it is at a maximum forward angle and consequently a maximum positive Doppler frequency. In a multilook processor, the signal is only observed for a given look during part of the passage of the antenna beam by the target. At the end of that time, the look is completed and the signal is placed in the store. The next time this target is observed, it is at a different azimuth angle and comes out of a different "filter output" of the FFT. Hence, the Temporary Store and Multiplexer must account for this, and first take the output for a given target from the highest-frequency "equivalent filter" of the FFT, then from the next-highest-frequency "equivalent filter," and so on until all of the independent looks have been properly averaged. Obviously, this is a relatively complicated process, so the Temporary Store and Multiplexer is a fairly complex computer.

It should be emphasized that many other configurations of synthetic-aperture processor could be considered. However, the one shown here is adequate for illustrating the relative complexity of such systems. If one simplifies the system by some alternate design, the simplification will be in proportion for the different alternative radar configurations considered here.

The values calculated for the real-aperature radar for average power, number of independent samples available, analog-to-digital processing rate, and telemetry rate use the same relations as those for the synthetic aperture, so that Equations (3.4) through (3.8) apply to the SAR as well as to the RAR.

The length of the FFT required is simply the number of pulses contained within a synthetic aperture at the maximum angle of incidence, where the synthetic aperture is the longest. This is the ratio of the length of the alongtrack resolution cell for the real aperture (alongtrack illuminated area) to the spacing between potential independent samples D/2, divided by the number of independent looks into which the potential synthetic aperture is subdivided. The resulting expression is

$$\text{FFT Length} = \frac{2\lambda h}{ND^2 \cos\theta_{max}} \tag{3.9}$$

The number of FFTs involved is simply the number of range cells and this is the ratio of the slant swath width R_a to the slant range resolution r_R. That is

$$\text{Number of FFT's} = \frac{R_a}{r_R} \tag{3.10}$$

The size of the corner-turning memory, in principle, would be simply the product of these two, but because of the time sequence in which signals enter the radar, it must be somewhat longer than that. A conservative number is twice the product of the quantities described in Equations (3.9) and (3.10). Therefore, the size of the corner-turning memory is

$$\text{Size of C.-T. Memory} = \frac{4\lambda h R_a}{D^2 r_y(\theta_{min}) \sin\theta_{min} \cos\theta_{max}} \qquad (3.11)$$

It should be recalled, however, that this corner-turning memory and the FFTs must be duplicated for the in-phase and quadrature channels. Furthermore, when excess bandwidth is used to obtain additional independent samples beyond those available in the alongtrack direction, the number of corner-turn memories and FFTs is multiplied by the excess-bandwidth ratio needed to achieve the required number of independent samples. Therefore, the processor in such a situation becomes extremely large and complex.

The total number of independent samples is the product of the number N_r obtained by excess range bandwidth and the number N_a obtained in the alongtrack direction

$$N = N_r N_a$$

The number required in the range direction is the excess-bandwidth ratio mentioned above, and N_a is given by Equation (3.6).

In Figure 3.3, reference functions are shown to be required for the SAR processor. The number of different reference functions required depends upon the depth of focus, which is given by

$$\text{Depth of Focus} = 2r_a^2/\lambda \tag{3.12}$$

The depth of focus is defined in the slant-range direction so that the number of reference functions required is simply the ratio of the slant swath width to the depth of focus or

$$\text{Number of Ref. Funcs.} = \frac{\lambda R_a}{2r_a^2} \tag{3.13}$$

For the first three cases discussed in the next section, more than one reference function is required. For the remaining cases of partially focused synthetic aperture a single reference function suffices, and for the unfocused synthetic-aperture, no reference function is required.

3.3.3 Scanning Radiometer-SAR

Figure 3.4 illustrates the scanning synthetic-aperture configuration that can be combined with a radiometer to produce the RADISAR. Basically, this system uses a scanned-array antenna and filters to separate the SAR signals from the radiometer signals; beyond that it is the same (except in some details of processing) as the other SARs and any radiometer design may be chosen. A larger antenna area may be used for the RADISAR than for the other configurations discussed here because of the fact that the antenna scans from one position to another, so the antenna height is not constrained by the swath. For this reason the power required is less.

3.4 System Tradeoffs

Various systems have been postulated for use in the soil moisture problem, with the reference system being a fully-focused synthetic-

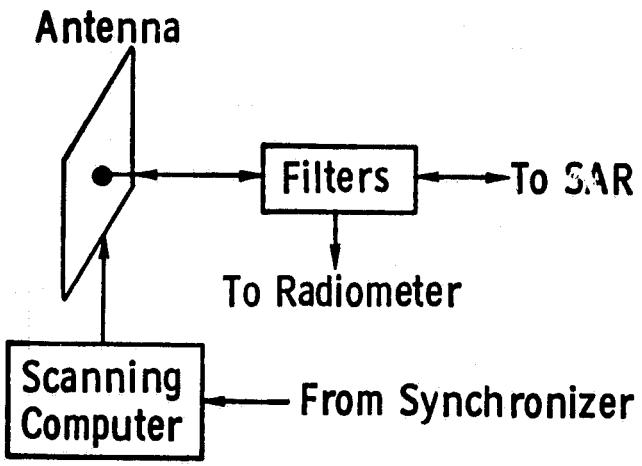

Figure 3.4 RADISAR configuration.

aperture radar with antenna 8.7 meters long and with a square pixel at 7°. Table 3.1 summarizes some of the characteristics of the systems considered, and Table 3.2 gives more details. The characteristics shown in Table 3.1 are: the equivalent square photographic quality pixel dimension r_e discussed in Section 3.2, the dimensions of the radar pixel at 22°, the number of looks used in the postulated system, the required average power, the speed required for each analog-to-digital converter, and the telemetry rate required if all processing is done on-board. If processing is not done on-board the telemetry rate is much higher (except for Case 1).

Case 1 is the fully focused reference case. Note that to achieve the 4.4 m resolution at 7° in the range direction, a 1.4 m resolution is needed at 22°. The power required is quite large and the A/D converter rate and telemetry rate are exceedingly large.

In Case 2, a partially focused SAR with 10 x 10 m resolution at 22° is compared with Case 1. Since it uses 12 looks to reduce the variance of the signal, and has to obtain many of these looks by excess bandwidth, its power requirement is also large, but the A/D converters operate at a rate about one order of magnitude less than for Case 1, and the telemetry rate is also an order of magnitude less. The equivalentphotographic-quality pixel dimension is not much more for Case 2 than for Case 1. This kind of resolution is probably entirely too fine for a soil-moisture radar.

Case 3 shows the resolution likely to be the finest that might be considered for a soil-moisture radar, and it has a 30 x 30 m resolution at 22°. Because it requires excess bandwidth, it also has a fairly high power (800 W), but its telemetry rate is down significantly.

TABLE 3.1

Design Options--Condensed Table

Case No.	Type	Equivalent-Square Photographic-Quality Pixel Dimension (m x m) 7°	22°	Radar Pixel at 22° r_a x r_y (m x m)	Number of Looks	Average Transmitter Output Power (W)	A/D Rate (Bytes/Sec)	Telemetry Rate for On-Board Processing (Bytes/Sec)
1	Fully Focused SAR	19.6	11.6	4.4 x 1.4	1	9850	2.9×10^8	2.7×10^8
2	Partially Focused SAR	25	14.7	10 x 10	12	7198	4.0×10^7	1.7×10^7
3	Partially Focused SAR	75	44	30 x 30	12	800	1.3×10^7	1.8×10^6
4	Partially Focused SAR	122	72	100 x 30	23	460	1.3×10^7	5.5×10^5
5	Partially Focused SAR	223	132	100 x 100	23	138	4.0×10^6	1.7×10^5
6	Unfocused SAR	343	202	300 x 100	69	138	4.0×10^6	5.5×10^4
7	Unfocused SAR	594	351	300 x 300	69	46	1.3×10^6	1.8×10^4
8	Unfocused SAR	1010	596	1000 x 300	230	46	1.3×10^6	5500
8a	Unfocused SAR	1084	640	300 x 1000	69	13.8	4.0×10^5	5500
9	RAR (D = 8.7 m)	1004	592	4564 x 71	1049	194	5.6×10^6	5100
10	RAR (D = 15 m)	1036	616	2724 x 120	363	38.6	3.3×10^6	5100
11	Unfocused SAR	1844	1088	1000 x 1000	230	13.8	4.0×10^5	1660
12	RAR (D = 15 m)	2992	1765	2724 x 1000	363	4.6	4.0×10^5	610
13	RAR (D = 8.7 m)	4613	2722	4564 x 1500	1049	9.2	2.7×10^5	240
14	RADISAR (5 m x 5 m antenna, 19 scan positions)	785	463	570 x 173	12	0.66	2.3×10^6	1.7×10^4

In Case 4, the processing is greatly simplified, but the range resolution is kept the same. Because the excess bandwidth is not required for Case 4, and is for Case 3, the power is less in Case 4.

Case 5 is a partially-focused SAR with 100 x 100 m resolution at 22° and 23 independent samples. This might be a realistic design. However, as indicated by the resolution study, this kind of resolution is probably not required; hence, the unfocused cases, Cases 6-8 and 11, are also shown. Note that the power required can be very small for these cases. Case 8a is shown in Table 3.1 to illustrate the effect on the power of exchanging the azimuth resolution for the range resolution. Of course, this is done at 22°, and at 7° it is not quite as good a system. However, the power is reduced from 46 to 13.8 watts.

Four RAR cases are shown, two with 8.7 m antenna lengths like the SAR, and two with 15 m antenna lengths. Cases 9 and 10 are designed to achieve a 7° equivalent photographic pixel dimension of about 1 km. As a result, the pixels have a very high length-to-width ratio, probably higher (at least in Case 9) than one can use to extend the results of the study indicated in Section 3.2. The 20:1 ratio in Case 10, however, may be reasonable. The other two cases have arbitrarily selected rather large range resolutions at 22°, so that the effective square-photographic-quality-pixel dimensions for these cases are very large. Note, however, that the powers are quite small.

Case 14 is the only case of the RADISAR considered. For the RADISAR, the 40 cm height of the other antennas needed to achieve the 7° - 22° swath width has been replaced by a 5 m height, and the antenna has been shortened to 5 m. This square array will produce nearly circular radiometer patterns on the ground. With this size antenna, 19 scan positions

are required for the scanning synthetic-aperture radar, which means that there are 19 radiometer measurements made across the swath. Because of the larger antenna, the average power is only 0.66 watts.

Table 3.2 gives more details of the systems described in Table 3.1, and also repeats some of the significant factors listed in Table 3.1.

Table 3.3 gives additional information regarding the complexity of the synthetic-aperture processors, namely the length of and number of FFTs and the size of the corner-turn memory (in bytes). Note that, in each case, a number for the FFT length that is a multiple of two is given. This is the actual length of the FFT, although some other transforms do not require that the length of the input be a multiple of two. In Case 1, both 1024 and 2048 are listed because the 1080 is so close to 1024 that only a small compromise would be made in using it. The corner-turn memory need not contain the additional zeros that enter the FFT.

A column is also included in Table 3.3 listing the number of FFT systems and corner-turn memories required. Thus, the numbers in columns 3 through 5 are for each set of these items and the total number required is that indicated in the last column.

The tradeoffs between resolution and the equipment required for the system, as well as the telemetry rate, are best illustrated by comparing the values of equivalent pictorial quality resolution r_e with the other quantities. Figure 3.5 illustrates the relation between this equivalent pixel dimension and the power and telemetry requirements. For the SAR, the power requirement decreases rapidly as the pixel dimension increases. Since the power required for the SAR depends primarily on the range resolution, cases involving similar pixel areas such as

TABLE 3.2: POTENTIAL SYSTEM DESIGN OPTIONS

Case #	Type	Slant Range Resolution r_R(m)	Number of Looks Available in Azimuth	Number of Looks Used N	7° $r_a \times r_y$ (m x m)	7° Equiv. Square Photo Pixel (m x m)	22° $r_a \times r_y$ (m x m)	22° Equiv. Square Photo Pixel (m x m)	Average Power (W)	A/D (Bytes/sec)	Telemetry Rate for On-Board Processor (Bytes/sec)
1	Fully focused SAR	0.52	1	1	4.1x4.3	19.6x19.6	4.4x1.4	11.6x11.6	9850	2.9×10^8	2.7×10^8
2	Partially focused SAR	3.75	2.3	12	9.3x31	25x25	10x10	14.7x14.7	7198	4.0×10^7	1.7×10^7
3	Partially focused SAR	11.2	6.9	12	28x92	75x75	30x30	44x44	800	1.3×10^7	1.8×10^6
4	Partially focused SAR	11.2	23	23	93x92	122x122	100x30	72x72	460	1.3×10^7	5.5×10^5
5	Partially focused SAR	37.5	23	23	93x307	223x223	100x100	132x132	138	4.0×10^6	1.7×10^5
6	Unfocused SAR	37.5	69	69	280x307	343x343	300x100	202x202	138	4.0×10^6	5.5×10^4
7	Unfocused SAR	112	69	69	280x922	594x594	300x300	351x351	46	1.3×10^6	1.8×10^4
8	Unfocused SAR	112	230	230	934x922	1010x1010	1000x300	596x596	46	1.3×10^6	5500
8a	Unfocused SAR	375	69	69	280x3074	1084x1084	300x1000	640x640	13.8	4.0×10^5	5500
9	RAR (D = 8.7 m)	26.6	1049	1049	4264x218	1004x1004	4564x71	592x592	194	5.6×10^6	5100
10	RAR (D = 15 m)	45.0	363	363	2545x369	1036x1036	2724x120	616x616	38.6	3.3×10^6	5100
11	Unfocused SAR	375	230	230	934x3074	1844x1844	1000x1000	1088x1088	13.8	4.0×10^5	1660
12	RAR (D = 15 m)	375	363	363	2545x3074	2992x2992	2724x1000	1765x1765	4.6	4.0×10^5	610
13	RAR (D = 8.7 m)	562	1049	1049	4263x4611	4613x4613	4564x1500	2722x2722	9.2	2.7×10^5	243
14	RADISAR (5 m x 5 m antenna 19 scan positions)	213	12	12	532x532	785x785	570x173	463x463	8.66	2.3×10^6	1.7×10^4

TABLE 3.3

Data-Handling Parameters

Case	22° r_a x r_y (m x m)	FFT Length (Bytes)	FFT #	Corner-turn Memory (Bytes)	Number Required
1	4.4 x 1.4	1080 (1024 or 2048)	73410	1.6×10^8	2
2	10 x 10	470 (512)	10278	1.7×10^7	12
3	30 x 30	157 (256)	3510	1.1×10^6	4
4	100 x 30	47 (64)	3510	3.3×10^5	2
5	100 x 100	47 (64)	1028	9.7×10^4	2
6	300 x 100	16 (16)	1028	3.2×10^4	2
7	300 x 300	16 (16)	343	11000	2
8	1000 x 300	4.7 (8)	343	3200	2
8a	300 x 1000	16 (16)	103	3200	2
9	4564 x 71	DNA			
10	2724 x 120	DNA			
11	1000 x 1000	4.7 (8)	105	990	2
12	2724 x 1000	DNA			
13	4564 x 1500	DNA			
14	570 x 173	14 (16)	31	900	2

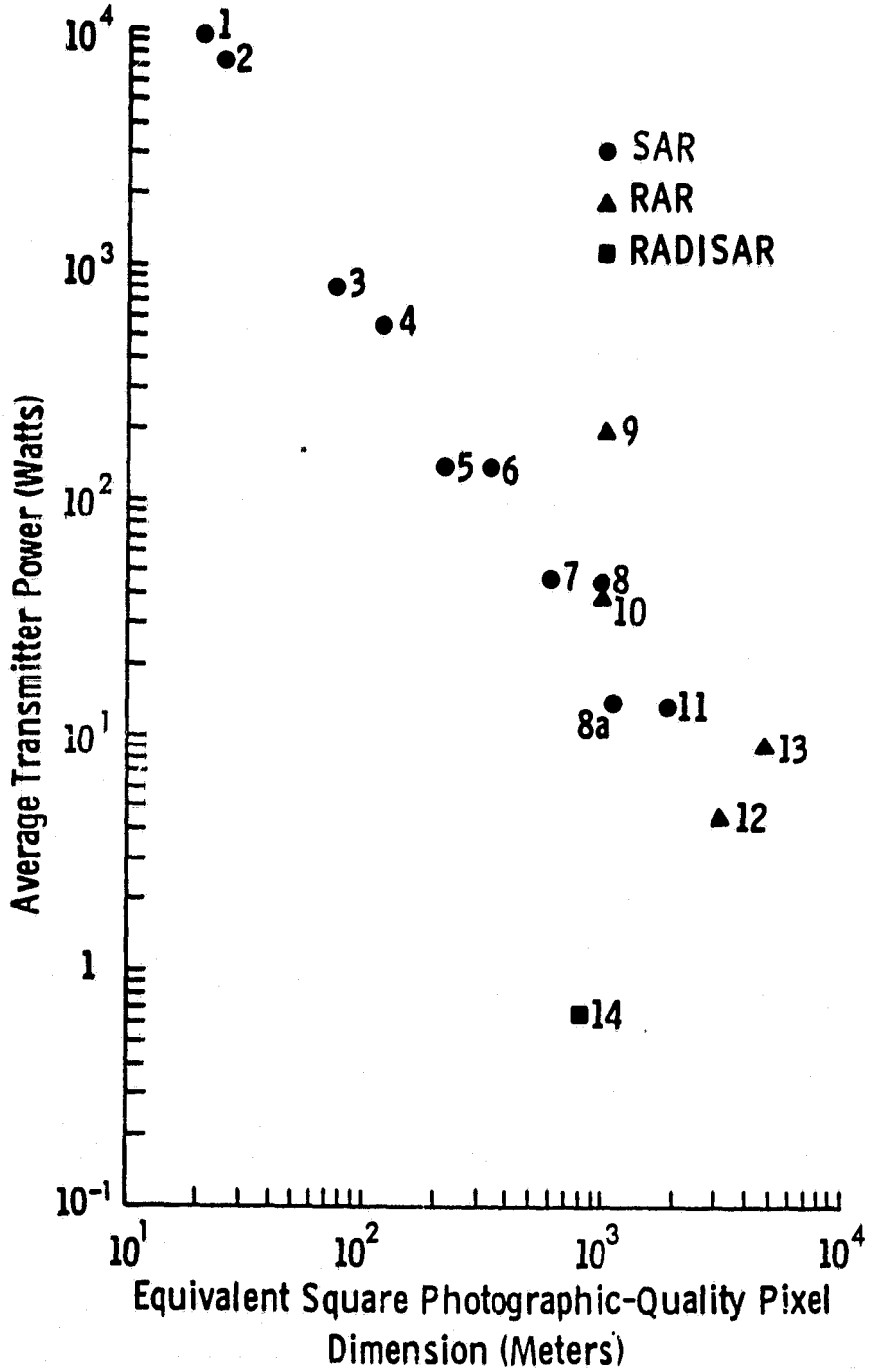

(a)

Figure 3.5. (a) Average transmitter power, and (b) telemetry rate, as a function of equivalent-square photographic-quality pixel dimension. The numeral next to a point refers to the case number in Table 3.1.

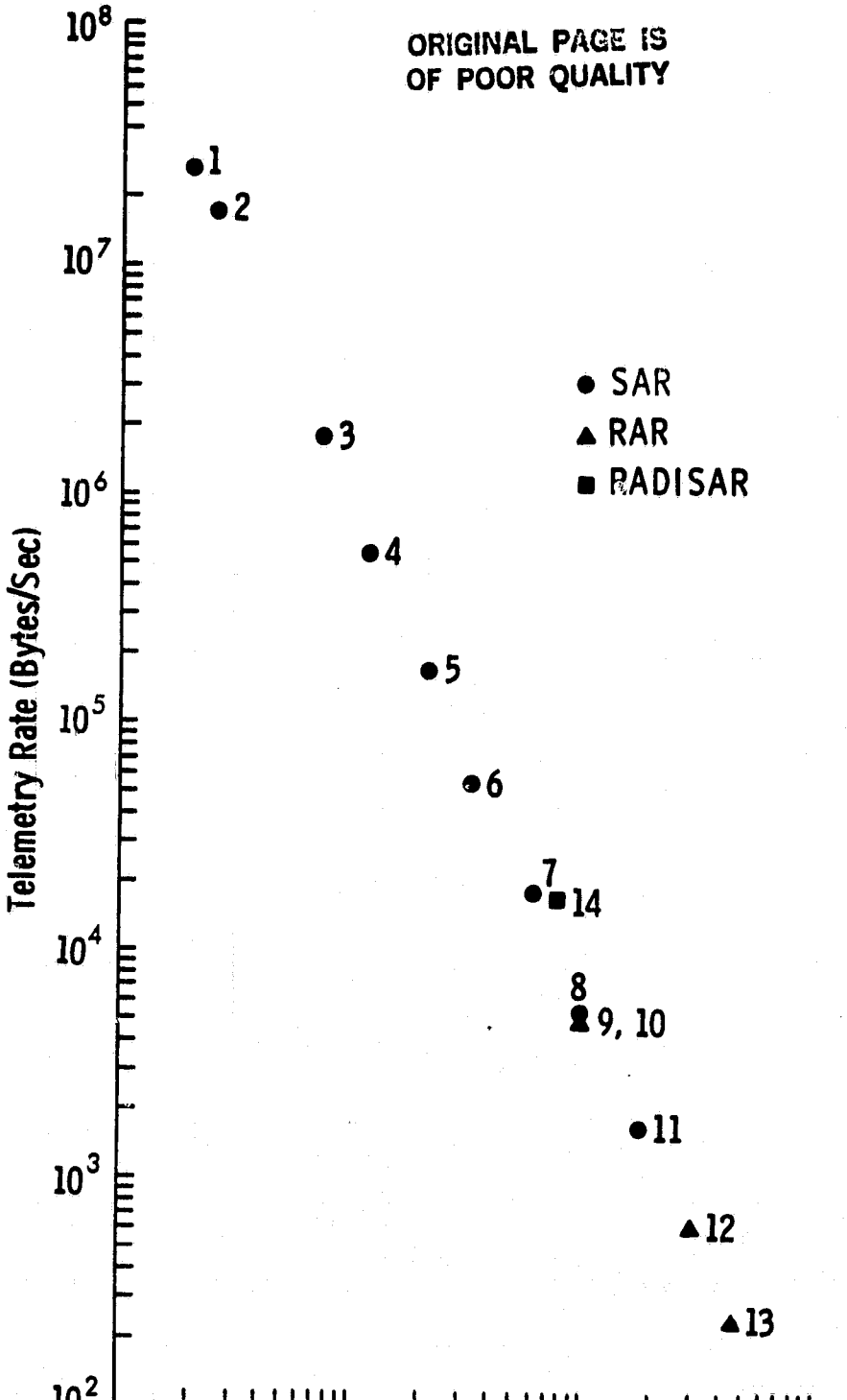

(b)

8 and 8a have similar photographic pixel dimensions but different power requirements. On the other hand, cases where range resolution applies to two different alongtrack resolutions, such as 3 and 4, or 5 and 6, require the same power (except for the increase in 3 due to use of excess bandwidth).

Although RARs follow the trends of the SAR reasonably well, the power requirements can differ quite significantly since the RAR power requirement also depends upon the range resolution. For instance, to achieve an r_e of about 1000, Case 9 requires a 71 m acrosstrack resolution at 22°, which causes the average power to go up to 194 W, a value much higher than required for the same equivalent pixel dimension with the SARs of Cases 8 and 8a. The RADISAR is well off the trend because its antenna area is not constrained to a reasonable length multiplied by a fixed height. Clearly the RADISAR is the least power-consuming of the options, but the processing for comparable r_e is more complex in ways not indicated by this kind of comparison. It also requires a larger and more complex antenna. However, this antenna makes possible the use of both lower power for the radar and of the radiometer along with the radar, which may be a significant advantage.

3.5 Relation of Tradeoffs to Simulations

Not all of the examples illustrated in Section 3.4 could be simulated. The simulation process is an expensive and time-consuming one, and the simulations must start off with a spatial resolution for the data base of 20 m x 20 m. For this reason, an actual simulation of Case 1 was impossible. An actual simulation at 7° of Case 2 was not possible, but one with a comparable equivalent square-photographic-quality pixel

was possible. However, the same could not be said about Case 2 at 22°, since the effective resolution there was finer than could be readily achieved with the data base. Also, although the techniques are available for degrading the image from a 20 x 20 image to any other value with larger pixel dimensions and with any number of equivalent independent samples, some methods are easier to carry out than others, and this tends to constrain the number of independent samples in the simulations.

Two sets of simulations were performed, covering the angular ranges of 7.5°-9.3° and 11°-12.8°. A third set, covering the 17.95°-19.6° range, was planned but was not performed due to time and cost constraints. In Table 3.4, a comparison is made between the simulations performed and the nearest equivalent system-study cases.

The simulations labeled A all are at the spatial resolution corresponding to the data base. They are all approximately equivalent in r_e to Case 2 at 7°. That is, the value of r_e obtained with the simulation was not significantly poorer (within 20%) than the r_e for Case 2 at 7°. Note that simulation B is approximately equivalent to Case 4 and simulation C is approximately equivalent to Case 8.

The soil-moisture-measurement implications of the simulations are discussed in other sections. However, one can say that simulation B has a resolution adequate to distinguish fairly easily the features of the image, whereas simulation C makes many of the features indistinguishable, although it is still quite useful for soil-moisture measurement. Simulation B has a considerably better resolution than the RADISAR case studied or any of the RAR cases studied. Simulation Case C, although most directly comparable with Cases 8 and 8a, is also reason-

TABLE 3.4

Simulations Compared with Nearest-System Case

Simulation Case	θ	Mid-Range Angle	r_y (m)	N	r_e (m)	Nearest System Case	r_e at θ (m)
A1	7.5°- 9.3°	8.2°	20	12	29.5	2	25 at 7°
A2	11.1°-12.8°	12.1°	20	12	29.5	2	25 at 7°
B1	7.5°- 9.3°	8.2°	90	23	125	4	122 at 7°
B2	11.1°-12.8°	12.1°	93	27	96	4	94 at 12°
C1	7.5°- 9.3°	8.2°	900	2250	974	8	976 at 7.5°
C2	11.1°-12.8°	12.1°	900	2800	753	8	750 at 13°

ably like Cases 9 and 10 for the RAR and gives a larger equivalent pixel dimension than Case 14 (the RADISAR).

Thus, one can state that the simulations conducted are reasonably representative of a fine-resolution case (2), a medium-resolution case (4), and a relatively poor-resolution case (8). Insufficient time and resources were available to simulate the still-coarser resolutions associated with Cases 11, 12, and 13; these may be quite useful for soil-moisture determination, but rather poor for other imaging purposes. This kind of simulation should be performed for these poorer resolutions and, indeed, extended to the larger cells that are likely to be found with a radiometer. Similarly, simulations to show the effect of pixels that are rectangular rather than square should be conducted for ratios of r_a to r_y considerably larger than those used in the simulations conducted to date. Not only may a maximum value of this ratio exist beyond which the concept of the gray-scale resolution and the resolution volume does not apply, but some maximum value for the alongtrack or acrosstrack pixel dimension may exist beyond which the results will be of little value.

4.0 SIMULATION STUDY

4.1 Radar Image Simulation

Image simulation has been used as a research tool to help determine sensor parameters for an orbital altitude radar whose images are to provide soil moisture information. The sensor parameters include, but are not limited to, operating frequency, polarization, angle of incidence, resolution, averaging, and data format. The investigation

of these parameters and the ability of spaceborne radar to provide quantitative soil moisture information was carried out by varying both sensor parameters (angle of incidence, resolution, averaging) and ground conditions (varying amounts of soil moisture). The frequency and polarization for the modeled sensor were chosen according to studies of terrain backscatter reviewed earlier in this report.

The following sections describe the physical processes of radar image formation, and the design and implementation of algorithms to generate radar images. Later, the results (images) are analyzed quantitatively to determine how well one can estimate soil moisture from a processed radar image. A processed radar image is one in which known sensor-dependent effects have been removed. For example, antenna gain variations in the range dimension are removed by scaling the image data according to an angularly dependent function.

The radar image simulation algorithms used in this study were developed by Stiles et al. [28]. The simulation procedure follows closely the actual operation of synthetic aperture radar imaging; thus, it is relevant to present an overview of the image formation processes herein. Sensor, terrain, propagation channel, geometric, and data processing effects will be treated in Sections 4.1.1 through 4.1.5. The overview and simulation will be presented in terms of generating fully focused synthetic aperture radar images. Changes necessary to accommodate the production of real aperture and partially focused SAR images will be discussed in Section 4.1.5.

4.1.1 An Overview of the Radar Image Formation Process

The orbital platform for a coherent radar system has known velocity, altitude, and attitude; the radar antenna is usually oriented with its electrical boresight perpendicular to the spacecraft velocity vector. The sensor transmits a waveform with known amplitude and phase modulations which are used in the information decoding process.

The pulse repetition frequency (PRF), is designed to simultaneously satisfy range ambiguity limitations (which set the maximum PRF) and azimuth ambiguity limitations (which define the minimum PRF) [35]. The azimuth dimension is parallel to the platform velocity vector while the range dimension is orthogonal to the velocity vector in the most common configuration. The power density transmitted into space by means of a directional antenna is large in the direction of the antenna main lobe and small in the direction of the side lobes. Due to diffraction the power density that is incident upon the ground is reduced from the transmitted value. The scattering and reflection processes which occur next direct some portion of the power in the "backscatter" direction, i.e., toward the radar receiving aperture. The backscatter cross-section of the illuminated terrain (σ) incorporates all ground effects needed to estimate the average received power $\overline{P}_R$; by the definition $\sigma = \sigma^o \cdot A_{eff}$ the ground effects can be further broken into a backscatter coefficient σ^o and an effective ground area term A_{eff}. Various types of terrain can be represented as having different backscatter responses, thus, the action of the terrain upon the transmitted pulse is characterized by amplitude modulations. Additionally, phase modulations are incurred because of the relative motion of the antenna with respect to the ground scatterers.

These modulations have been theoretically modeled, and are also used in the signal decoding process.

Each transmitted pulse illuminates a swath of ground; the corresponding received pulse is mixed with a stored signal to put the information on a carrier of lower frequency. Then the packet of information is written as a modulated bipolar video frequency onto a "signal film," or it is stored digitally as a matrix row. Each subsequent received pulse is written alongside the previous one in synchronism with the spacecraft's velocity. To relate the signal film coordinates to the ground geometry, distance across the width of the film represents increasing range from the antenna, while distance along the film represents azimuth.

The processing of the raw data is simple in concept, but complicated in practice. It is appropriate to think of the raw data as a two-dimensional complex signal having amplitude and phase; additionally, the signal film consitutes a Fresnel zone plate whose diffraction properties are used to produce the final image. Two basic operations are performed on the data in the orthogonal dimensions of range and azimuth: range compression and azimuth focusing. Both are implementable by frequency-dependent phase shifts; the end-product following these operations is a "complex image" referred to as a radar hologram. Either the real amplitude or real magnitude of the hologram is usually used to develop a film negative for the final radar image.

The resultant radar image has properties much different from those of noncoherent imagery. The phase coherence of the sensor not only allows fine resolution images to be generated, but it also inherently causes a strong correlation to be induced upon the backscattered signals, thus making the image representation of the fading signal appear speckled

and wormy. Additionally, the geometry of radar gives it unique properties which one must understand for interpretation purposes. These geometrical factors will be discussed in the following sections.

4.1.2 Target Geometry Considerations

Four geometric effects are of considerable importance in radar imaging and the simulation of images: foreshortening, layover, shadow, and local slope. Additionally, earth curvature can be important, and is discussed in Section 4.1.3. Foreshortening refers to object compression seen in the radar image, and it occurs for positive slopes (landform rising along the increasing range direction). Layover is a more severe case which is commonly demonstrated by the "flagpole" example in which the incidence angle of the radar and the height of the pole dictate that the top of the flagpole is "seen" by the radar before the base of the pole. Shadow is the absence of illumination due to the presence of trees, buildings, mountains, etc., which occlude the terrain that they precede in range. These geometry-related factors are incorporated in simulation through range calculations with respect to the radar, and by neighborhood comparisons. Specifically, average return powers computed by the radar equation [29] are apportioned to the correct range gates or bins.

The local angle of incidence, θ_ℓ, is defined as the angle between a local normal for a scattering element and the range vector running from the antenna to the element. Implicitly, a planar facet exists to help define the local normal. The simulation algorithms examine the terrain and define slopes in the range and azimuth dimensions to determine the facet orientation. When θ_ℓ is zero degrees, i.e., the scatter-

ing element or cell is oriented perpendicularly with respect to the range vector, then the backscatter power is predicted by the known backscatter response for that target class, e.g., pasture, for an angle of incidence, θ, of zero degrees. The assumption is thus made that the backscatter response (σ° vs. θ) should be examined at θ_ℓ to incorporate local slope. Thus, the simulation algorithms use $\sigma^\circ(\theta_\ell)$ to predict return power (through the radar equation [29]).

Multipath effects can be significant for certain terrain conditions, but are not included in the simulation algorithms. Multipath reflections from water, followed by scattering from the terrain can cause the "far shore" of lakes, rivers, etc., to be brightened. Since our application for simulation is to test soil moisture prediction algorithms, primarily for agricultural regions, water-body boundaries are not of great interest.

4.1.3 Earth Curvature Considerations

The sensor platform altitude, being significant in relation to the radius of the Earth, causes the angle of incidence, θ, measured between a normal to the ground within the swath and the range vector, to be larger than the radar incidence angle measured between nadir (relative to the sensor) and the range vector. As shown in Figure 3.1, $\theta > \delta$. The relationship between these angles of incidence is given by

$$\theta = \sin^{-1}\left\{\left[\frac{a+h}{a}\right] \cdot \sin\delta\right\} \qquad (4.1)$$

Because θ also affects the local angle of incidence, θ_ℓ, the Earth's curvature is quite significant. The mid-range δ values employed in

the simulations, i.e., 8.4° and 11.9°, correspond to θ's of 9.1° and 13.0°, respectively.

The geometry effects defined above are modeled and incorporated as deterministic influences on the amplitude structure of the reflected pulse of microwave energy. They affect the average power calculations for each picture element as they define where the power from scattering regions belong in the radar image. The scattering action of the terrain, which perturbs the amplitude and phase of the transmitted pulse, is, however, modeled as a random phenomenon commonly known as fading. For most distributed targets the random point process is reasonably described by the Rayleigh distribution [30]. The requirements for this case are that no one scattering center dominates the reflection/scattering process, that there are many scattering centers within the smallest discriminable terrain element, and that the phases of the returns from the various centers are independent [30]. This topic will be discussed further in Section 4.1.4.

4.1.4 Simulation of Fading and Other System Effects

The radar system transmits a narrowband signal and receives a scattered signal that is characterized as a narrowband Gaussian random process [38]. This model for the real signal is consistent with the Rayleigh scattering model [31]. That is, the statistical nature of the envelope can be generated either by drawing samples from a Rayleigh random number generator or by generating and processing two independent random Gaussian numbers for the N = 1 case (thus, mimicking the quadrature reception of the SAR signal.) The detected voltage statistics

are governed by a negative exponential distribution for N = 1. For most of the simulations prepared for this study, the following model [32,33] was used to compute instantaneous values of the scattered power

$$P_R = \frac{\bar{P}_R}{2N} \cdot y \tag{4.2}$$

where P_R is the power calculated for each facet on the ground, $\bar{P}_R$ is the average power calculated by the radar equation, N is the number of independent samples, and y is a random variable which is distributed as an exponential variate or as a chi-square variate with 2N degrees of freedom. Thus, if an N = 1 image is desired, two free squares enter the calculation, i.e.,

$$x_2^2 = Z_1^2 + Z_2^2 \tag{4.3}$$

where Z_1 and Z_2 are independent, normally distributed random numbers, $\mu(0,1)$ (zero mean, unit variance). The larger the number of looks desired, the higher the probability becomes that the actual received power is close to $\bar{P}_R$, which is given by [29, 34] as

$$\bar{P}_R = \bar{P}_T \frac{G_T(\theta,\phi) G_R(\theta,\phi) \lambda^2 \sigma^\circ A}{(4\pi)^3 R^4} \tag{4.4}$$

The assumption was made that the factor

$$\bar{P}_T \frac{G_T(\theta,\phi) G_R(\theta,\phi)}{(4\pi)^3} \lambda^2 \tag{4.5}$$

could be written as a constant, and that furthermore this constant value c could be calibrated out of the resultant SAR image by a scaling

constant. If a linear system model is applicable for the receiver and processor, then this scaling is plausible. Since the terrain surface slope is generally unknown, it is not possible to remove the range R and resolution area A terms for estimating σ^o.

As discussed earlier, the value of σ^o used for computing the average received power from a resolution cell is $\sigma^o(\theta_\ell)$ where

$$\theta_\ell = \cos^{-1}(\hat{p} \cdot \hat{n}) \tag{4.6}$$

$\hat{p}$ = the unit vector pointing from the center of the resolution cell to the antenna center

$\hat{n}$ = local normal unit vector constructed for a facet model of the resolution cell

Average power was actually calculated for the finest resolution possible, approximately 20 meters by 20 meters. That is, for each entry in the ground-truth data base, the local angle of incidence was determined from the given elevations of the cell in question and its nearest four neighbors and from the given sensor position. The corresponding value of the backscatter coefficient is drawn from a stored table of σ^o versus θ_ℓ. The average received power that is utilized for each location is

$$\bar{P}_R = \frac{c\, A\sigma^o(\theta_\ell)}{R^4} \tag{4.7}$$

where c = 1 and A is defined as

$$A = \frac{d_{az}}{\cos\rho} \quad \frac{d_r}{\sin(\theta-\psi)} \tag{4.8}$$

where

d_{az} = data base resolution in the azimuth dimension

d_r = data base resolution in the range dimension

θ = angle of incidence relative to a flat surface (not the local angle)

ρ = angle of the slope of the cell in the plane orthogonal to the plane of incidence

ψ = angle of the slope in the plane of incidence

The simulations that were produced are in ground range format, and this basically means that range gates were explicitly set up in non-equal intervals; in fact, the range gates were purposely made smaller at the near-range edge of the image. The gate length is given by

$$G = \frac{c\tau_e}{2} \cdot \sin\theta \tag{4.9}$$

Suppose that the slant range resolution is 25 meters. Then the range gate defined by Equation 4.9 has length 8.6 meters for a nominal angle of incidence of 20°. The purpose of the inclusion of the $\sin\theta$ factor is to compensate for the inherent poorer resolution (in range) that occurs in the near range of the scene compared with the far range.

The local angle of incidence, and subsequently the area and back-scatter coefficients, are computed for each terrain cell. The average power is distributed among range bins according to the position of the terrain facet center relative to the start- and stop-points of the appropriate range bins. For example, if the range to a certain ground facet puts it three-tenths of a range bin away from the start of the $(k + 1)$ range bin, then three-tenths of the power for that ground

facet will be allotted to the k^{th} bin and seven-tenths is contributed to range bin k + 1.

The power in each of the ground-range gates is used as the basis for the calculation of the fading value as in Equation 4.2. As was indicated in Table 3.4, there were various numbers of looks required; in cases where N is greater than 12, the approach via Equation 4.2 was used to generate N = 1, 2, or 3 looks. These images were subsequently smoothed to trade resolution for averaging via the application of a low-pass filter [28] which implements the scanning mixed integration for SAR S/N improvement [36, 37] to achieve the looks calculated for B1, B2, C1, and C2 (Table 3.4). In the case for which N was required to be 12 looks, a Gaussian approximation to the operation of Equation 4.2 was used, that is [39]

$$P_R = \bar{P}_R\left(1 + \frac{Z}{\sqrt{N}}\right) \tag{4.10}$$

where Z is distributed as a Gaussian random variable with zero mean, unit variance, i.e., $\mu(0,1)$.

Noncoherent spatial domain smoothing was applied to several of the images generated via Equation 4.2. Coherent processing will be defined as any operation on amplitude and phase of a radar signal; incoherent processing will be defined as operations on amplitudes only or on power only. Thus, azimuth focusing and range compression are coherent operations; signal processing to improve the signal-to-noise ratio is usually done coherently with an incoherent sum of intensity data at the end.

4.1.5 Noncoherent Processing to Increase Averaging

When the number of looks required (see Table 3.4) was large (>12), it was infeasible to generate chi-square random numbers to satisfy our needs. However, if we first generate N = 1, 2, or 3 simulations, 20 m x 20 m resolution, we would be able to use these as bases for subsequent resolution degradations. Therefore, we applied a spatial domain convolution (reported in [28]) as suggested by Zelenka [37]. The low pass filter derived and applied to N = 1, 2, or 3 images accomplishes the scanning mixed integration operation for speckle reduction.

Both the scanning and discrete mixed integrators [37] use non-redundant spectral information for a radar scene and they make intensity images from the inverse transforms of several subsections of the spectra. A moving window is applied for scanning, and fixed windows at several locations are used in the discrete mixed-integration case. Convolution simultaneously degrades resolution while averaging out the variations in image intensity due to coherent fading. Thus, it was possible to increase the number of looks and to degrade resolution by approximately integral multiples to the values specified in Table 3.4.

4.1.6 Radar System Parameters Modeled

Three different radar systems were modeled in this study; these consisted of two partially focused SAR's and one unfocused SAR (see Table 3.4). Since the ground truth data base pixel spacing is 20 meters by 20 meters, the finest resolution simulations were generated for this resolution. The frequency and polarization of the radar were 4.75 GHz; horizontally transmitting, horizontally receiving, respectively.

Due also to data base size limitations (approximately 19.2 kilometers in range by 16.4 kilometers along the azimuth dimension) it was not possible to represent the desired swath (143 km along the range dimension) by one simulated radar image. It was necessary to use the same data base for several different angles of incidence as samples of the desired swath (see Table 3.4).

4.2 Determination of Mean Backscattering Coefficient of Target Conditions as a Function of Incidence Angle and Moisture

The data reviewed in section 2.0 were compiled and evaluated to determine algorithms which estimate mean backscattering coefficient at approximately 4.75 GHz and HH polarization as a function of target class and incidence angle. The general form of the estimation algorithm is given as:

$$\bar{\sigma}^{o} = f(\theta_{\ell}) + g(\theta_{\ell}) \times M_{Fc} \qquad (4.11)$$

where

$\bar{\sigma}^{o}$ = the mean σ^{o} in dB of a given target class

$f(\theta_{\ell})$ = a function of incidence angle θ which includes row-direction effects in certain agricultural crops

$g(\theta_{\ell})$ = the radar sensitivity to moisture for a given target-class as a function of incidence angle

M_{FC} = the 0-5 cm soil moisture expressed as a percent of the 1/3-bar water content

θ_{ℓ} = the local angle of incidence

Source data at center frequencies between 4.25 and 4.9 GHz with HH polarization representing each target class in the simulation were used to determine $f(\theta)$ and $g(\theta)$ in Equation 4.11. For a given target class, values of $f(\theta)$ and $g(\theta)$ were established by least-squares linear regression of σ^o as a function of soil moisture M_{FC} at each available angle of incidence. The linear regression coefficients for bare soil and crop classes are given in Table 4.1 at incidence angles of 0°, 10°, 20° and 30°. A representative scatterplot is shown in Figure 4.1 for smooth bare soil at 10° incidence angle. The linear regression coefficients were fitted with third-order polynomials as a function of incidence angle to produce $f(\theta)$ and $g(\theta)$ as given in Table 4.2. Assuming σ^o to be continuous and correlated as a function of incidence angle, the values in Table 4.2 permit the estimation of mean radar backscattering coefficient $\bar{\sigma}^o$ for $0° \leq \theta \leq 30°$ and $0 \leq M_{FC} \leq 150$.

All moisture dependent $\bar{\sigma}^o$ algorithms incorporate percent of the 1/3-bar water content M_{FC} in the 0-5 cm layer as the pertinent soil moisture indicator. The 1/3-bar water content approximates field capacity for certain soils. For the data sources listed in Table 4.1, the 1/3-bar water content of the soil was either measured directly [42,44] or estimated from soil textural components by [25]:

$$FC = 25.1 - 0.21\ (\%\ \text{sand}) + 0.22\ (\%\ \text{clay}) \tag{4.12}$$

where

FC = estimated water content at 1/3 bar

and

$$M_{FC} = 100\ Mg/FC \tag{4.13}$$

where

TABLE 4.1

Linear Regression Coefficients, Correlation Coefficients, Sample Size, and Data Sources of 4.75 GHz, HH Radar Response to 0-5 cm Soil Moisture of Target Classes at Selected Incidence Angles

Target Class	Sample Size	Incidence Angle	Regression Coefficients		Linear Correlation Coefficient	Number of Soil Textures	Number of Experimental Fields	Data Sources
			$f(\theta)$	$g(\theta)$				
Bare Soil, Smooth	46	0	- 5.13	0.182	.49	2	3	[40,41]
	106	10	-17.53	0.160	.85	5	6	[40,41,42]
	106	20	-21.01	0.131	.83	5	6	[40,41,42]
	46	30	-23.82	0.112	.66	2	3	[40,41]
Bare Soil, Medium Rough	49	0	-11.69	0.137	.73	2	3	[40,41]
	49	10	-15.49	0.149	.89	2	3	[40,41]
	49	20	-17.47	0.128	.82	2	3	[40,41]
	49	30	-18.85	0.114	.83	2	3	[40,41]
Bare Soil, Rough	29	0	-15.09	0.157	.83	2	2	[40,41]
	29	10	-14.18	0.139	.88	2	2	[40,41]
	29	20	-17.06	0.145	.89	2	2	[40,41]
	29	30	-19.82	0.163	.88	2	2	[40,41]
Corn	33	0	- 7.77	0.128	.68	2	3	[43,44]
	32	10	-11.36	0.104	.87	2	3	[43,44]
	32	20	-14.22	0.076	.74	2	3	[43,44]
	33	30	-15.57	0.079	.69	2	3	[43,44]
Milo	22	0	- 9.74	0.124	.86	1	1	[43]
	22	10	-12.12	0.086	.73	1	1	[43]
	22	20	-13.48	0.067	.54	1	1	[43]
	22	30	-14.47	0.062	.57	1	1	[43]
Soybeans	55	0	-10.00	0.181	.91	2	3	[43,44]
	55	10	-13.60	0.126	.89	2	3	[43,44]
	55	20	-14.63	0.093	.90	2	3	[43,44]
	55	30	-16.13	0.096	.89	2	3	[43,44]
Wheat	34	0	- 1.68	0.108	.72	2	5	[43,44]
	34	10	-16.02	0.160	.91	2	5	[43,44]
	34	20	-12.84	0.025	.35	2	5	[43,44]
	34	30	-14.20	0.019	.23	2	5	[43,44]

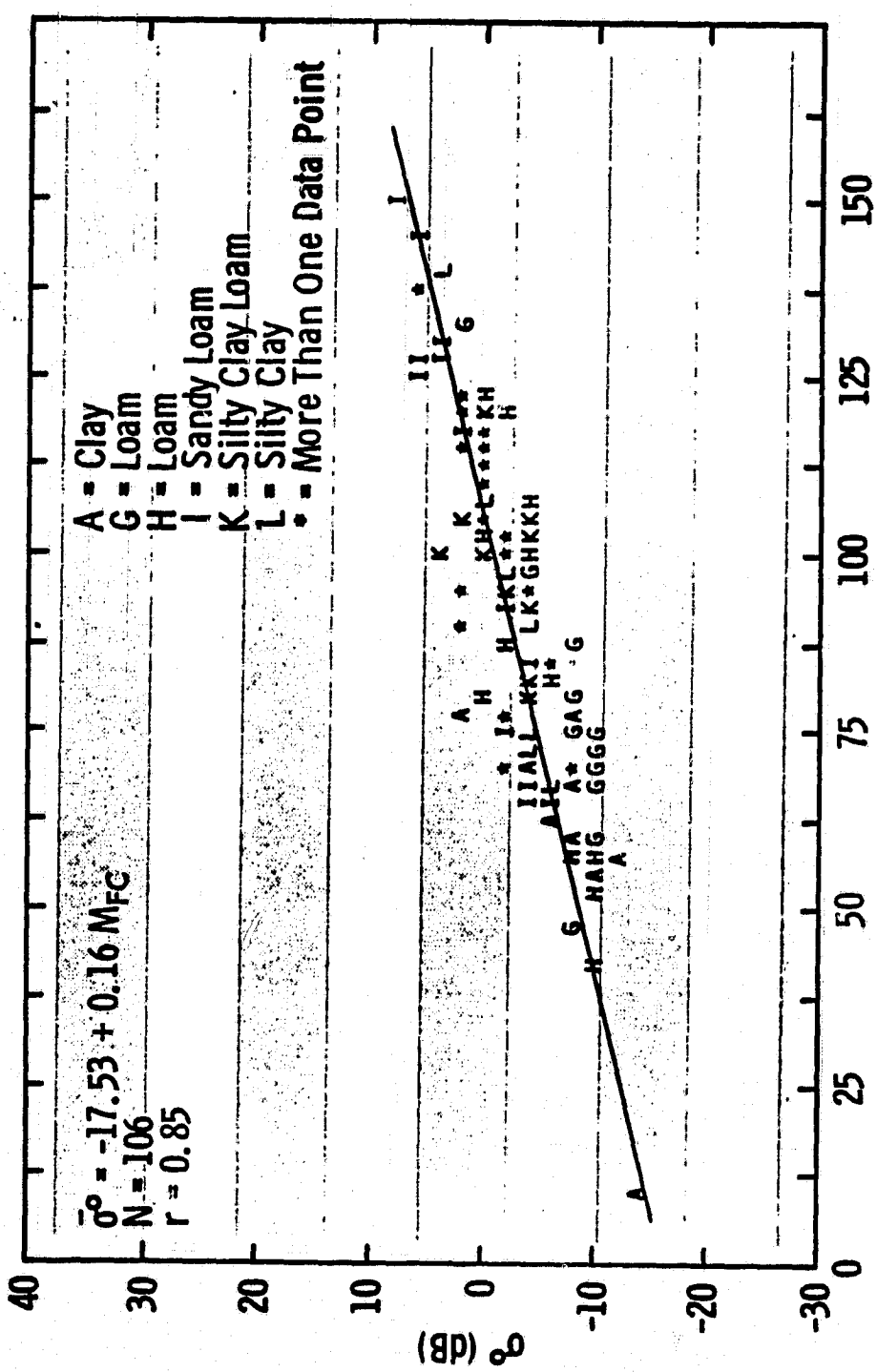

Figure 4.1 Backscattering Coefficient σ^o at 4.5 GHz, HH Polarization, 10° Angle of Incidence from Smooth Bare Soil Plotted as a Function of Percent of 1/3-Bar Water Content in the 0-5 cm Soil Layer

TABLE 4.2

Mean σ^o Algorithms for Simulated Target Classes

$$\bar{\sigma}^o = f(\theta) + g(\theta)\, M_{FC}$$

A. Targets Modeled as a Function of Soil Moisture, Where $g(\theta) \neq 0$.

$$f(\theta) = f_1 + f_2\theta + f_3\theta^2 + f_4\theta^3$$

$$g(\theta) = g_1 + g_2\theta + g_3\theta^2 + g_4\theta^3$$

Target Class	Roughness Class or Row Direction*	Algorithm Coefficients**							
		f(θ)				g(θ)			
		f_1	f_2	$f_3 \times 10^{-2}$	$f_4 \times 10^{-3}$	g_1	$g_2 \times 10^{-2}$	$g_3 \times 10^{-3}$	$g_4 \times 10^{-5}$
Bare Soil	Smooth	- 5.13	- 1.961	8.59	- 1.375	0.182	- 0.122	- 0.123	0.287
	Medium Rough	-11.69	- 0.512	1.52	- 0.202	0.137	0.463	- 0.381	0.70
	Rough	-15.09	0.219	- 2.25	0.332	0.157	- 0.353	0.191	- 0.22
Mown Pasture	NA	- 5.13	- 1.961	8.59	- 1.375	0.182	- 0.122	- 0.123	0.287
Pasture	NA	- 1.675	- 3.045	19.8	- 3.674	0.107	2.522	- 2.523	5.278
Alfalfa	NA	- 1.675	- 3.045	19.8	- 3.674	0.107	2.522	- 2.523	5.278
Soybeans	Parallel	-10.00	- 0.591	2.81	- 0.509	0.181	- 0.614	0.041	0.228
	+Perpendicular	-10.00	- 0.574	3.31	- 0.676	0.181	- 0.614	0.041	0.228
Milo	Parallel	- 9.74	- 0.311	0.835	- 0.108	0.124	- 0.502	0.132	- 0.113
	+Perpendicular	- 9.74	- 0.294	1.34	- 0.275	0.124	- 0.502	0.132	- 0.113
Corn	Parallel	- 7.77	- 0.369	- 0.036	0.133	0.128	- 0.093	- 0.205	0.607
	+Perpendicular	- 7.77	- 0.352	0.464	- 0.034	0.128	- 0.093	- 0.205	0.607
Wheat		- 1.675	- 3.045	19.8	- 3.674	1.107	2.522	- 2.523	5.218
Sandbars		- 5.13	- 1.961	8.59	- 1.375	0.182	- 0.122	- 0.123	0.287

* Roughness Class is based on RMS height in cm: $0 < \text{Smooth} \leq 2.0 < \text{Medium Rough} \leq 4.0 < \text{Rough}$. Row directions are given with respect to radar look direction.

** These algorithm coefficients are valid for incidence angles between 0° and 30°, relative to nadir.

\+ For row crops $\bar{\sigma}^o$ perpendicular = $\bar{\sigma}^o$ parallel + look direction modulation function.

TABLE 4.2 (continued)

B. Targets Modeled with no Dependence on Soil Moisture, where $g(\theta) = 0$ and $f(\theta) \neq$ constant.

Target Class	$f(\theta)$*
Water Bodies	$22.82 - 5.126\theta + 0.237\theta^2 - 3.973 \times 10^{-3}\theta^3$
Deciduous Trees	$10 \log (10^{-1.143} \times \cos\theta)$

* $f(\theta)$ for these targets is valid for $0° \leq \theta \leq 30°$.

C. Targets Modeled with no Dependence on Soil Moisture or Incidence Angle, where $g(\theta) = 0$ and $f(\theta) =$ constant.

Target Class	Constant Value (dB)
Railroads	10.0
Bridges	10.0
Buildings	10.0

Mg = gravimetric soil moisture

The use of M_{FC} in Equation 4.11 serves to minimize the dependence of σ^o on soil texture at a given gravimetric or volumetric soil moisture. In Figure 4.1, each symbol represents a different soil texture for bare soil with RMS roughness $\leq$ 2.0 cm. The result of the net linear regression result shown for θ = 10°,

$$\sigma^o = -17.53 + 0.16\ M_{FC} \qquad (4.14)$$

is not significantly different from the result obtained for any single soil texture regressed alone.

In addition, only data for moisture conditions less than M_{FC} = 150 were used in algorithm development since M_{FC} greater than 150 represents flooded soil conditions. When moisture conditions exceed saturation, the linear algorithm model given by Equation 4.11 for a given incidence angle becomes invalid at a given angle since the electromagnetic behavior of the target becomes similar to that of a smooth water surface.

Other target classes show no dependence upon soil moisture in establishing a mean σ^o response. Deciduous trees, roads, and water bodies are modeled with a dependence only on incidence angle and hence $g(\theta) = 0$. Cultural targets are modeled with a constant $\bar{\sigma}^o$ for all incidence angles and soil moisture conditions.

4.2.1 Bare Soil Algorithms

The generalized bare soil algorithms given in Table 4.1 are for three classes of surface roughness conditions. For the bare soil case, surface roughness is considered for randomly distributed soil aggregates

on a planar surface where roughness is defined by the RMS height in cm of the aggregates. For convenience, the range of probable RMS values within the simulation test site was subdivided into three roughness classes which correspond to distinct phases of soil tillage:

1) 0 < RMS height $\leq$ 2.0 cm for smooth bare soil,
2) 2.0 cm < RMS height $\leq$ 4.0 cm for medium rough bare soil, and
3) 4.0 cm < RMS height for rough bare soil.

Within the simulated area, a smooth soil surface would exist for fallowed fields, especially wheat fields, and would be most prevalent just prior to seed bed preparation in the spring. A smooth surface also describes that usually existent under certain crop canopies: pasture, alfalfa, and wheat. For the simulated area, the rough bare soil condition with RMS height exceeding 4.0 rarely occurs under normal circumstances and then only as an immediate consequence of a tillage operation such as plowing or cultivation. The rough bare soil condition tends to exist only until a precipitation event which reduces RMS height to the medium rough class. Thus RMS height > 4.0 cm is transitory and tends to exist only in association with dry to moist soil conditions. The medium rough soil condition describes the soil surface most prevalent within the simulated area. This condition is typical of the soil surface beneath the canopies of most row crops: corn, milo, and soybeans.

A variety of soil textures also are included in the development of the bare soil algorithms. The choice of M_{FC} as the soil moisture descriptor effectively minimizes $\bar{\sigma}^{o}$ estimate error due to soil texture effects. Table 4.3 lists RMS values and soil textures of the experimental data used to develop the bare soil algorithms given in Tables 4.1 and 4.2.

TABLE 4.3

RMS Surface Roughness and Soil Textural Classification of Experimental Data Used to Develop Bare-Soil Algorithms

Roughness Class	Soil Textural Class	RMS Height (cm)	Number Of Data Points
Smooth	clay	0.88	13
	loam	1.1	16
	loam	1.8	17
	*sandy loam	1.32	20
	*silty clay loam	1.03	20
	*silty clay	0.70	20
Medium Rough	clay	2.6	13
	loam	2.2	17
	loam	3.0	19
Rough	clay	4.3	14
	loam	4.1	15

* Data available at 10° and 20° incidence angles only.

4.2.2 Vegetation-Covered Soil Algorithms

The form of the general algorithm for crops given by Equation 4.11 assumes negligible two-way attentuation of the soil backscatter component by the vegetation canopy. This assumption has been shown [14] to be valid for radar operating at frequencies less than 8 GHz and incidence angles less than 20°. The breakdown of this assumption at higher angles of incidence for increasing canopy mass and transmission path length explains, in part, the decrease in least-square linear correlation coefficient with increasing incidence angle as documented in Table 4.1. This decrease is especially apparent for wheat and milo which have predominantly vertical canopy geometries.

In lieu of extensive data sources for σ^o as a function of moisture for pasture and alfalfa at 4 to 5 GHz, the general algorithms given in Table 4.2 for these crops are derived from data for wheat. In addition, and for the same reason, the general algorithms for sand bars and mown pasture are assumed equivalent to that for smooth bare soil.

The source data for the linear regression results given in Table 4.1 are derived from measurements made over the full phenologic development of each crop and thus represent time-independent or mean canopy conditions. Also, the source data for each crop generally includes data from more than one experimental test field and more than one soil texture.

All of the source data for the results shown in Table 4.1 were obtained from measurements made with no preferred radar look direction relative to crop row direction. As such, $f(\theta)$ as given in Table 4.2 includes no effects due to periodic row geometry.

From prior row-experiment measurements [43,44] for corn and soybeans a simple look-direction modulation function is introduced to ac-

count for periodic soil structure underlying these crop canopies and milo [13]. It is assumed that $\bar{\sigma}^0_{//}$ from a look-direction parallel to crop row direction is equivalent to $\bar{\sigma}^0$ from a vegetated surface without row patterns. The look-direction modulation function is defined by [13]:

$$M(dB) = \sigma^0_{\perp} - \sigma^0_{//} \tag{4.15}$$

where

$\sigma^0_{\perp}$ = σ^0 in dB for radar look direction perpendicular to periodic ridge/furrow row structure, and

$\sigma^0_{//}$ = σ^0 in dB for radar look direction parallel to periodic ridge/furrow row structure.

For corn and soybeans, whose mean values of M(dB) are 0.0 dB, 0.5 dB, 1.0 dB, and 0.5 dB at incidence angles of 0°, 10°, 20°, and 30° respectively, a third order polynomial fit gives M(dB) as a function of incidence angle. Thus,

$$M(\theta) = 0.0167\theta + .005\theta^2 - 0.167 \times 10^{-3}\theta^3, \text{ dB} \tag{4.16}$$

between 0° and 30° incidence angles.

In Table 4.2 and for row crops with rows oriented perpendicular to radar look direction $f(\theta)_{\perp}$ is the sum of Equation 4.16 and $f(\theta)_{//}$ for the same crop aligned with row structure parallel to sensor look direction

$$f(\theta)_{\perp} = f(\theta)_{//} + M(\theta), \text{ dB} \tag{4.17}$$

For simplicity, the above approach to row direction effects assumes:

1) no dependence of $M(\theta)$ on soil moisture,

2) $\sigma^{\circ}_{//}$ is equal to σ° for a soil with no periodic row structure, and

3) all three row crops have equivalent row structures and thus equivalent $M(\theta)$.

In addition, $M(\theta)$ defined by Equation 4.16 applies only to dryland farming characteristic of the simulation test site and characteristic of the source data.

4.2.3 Target Classes with No Dependence on Soil Moisture

Target classes from which radar backscatter at 4 to 5 GHz exhibit no dependence on soil moisture include deciduous tree canopies, open water bodies, and cultural targets. For the purposes of this simulation, and in the absence of a comprehensive source data base, all cultural targets such as railroads, bridges, roads, and buildings are modeled as having a constant $\bar{\sigma}^{\circ}$ which will effectively saturate the simulated imagery. This approach is consistent with Seasat imagery for urban areas.

Based upon data acquired by the University of Kansas [45], spring and summer deciduous tree canopies are considered to effectively attenuate the backscatter component from the underlying soil at 4 to 5 GHz. Radar backscatter response to deciduous trees is therefore modeled as a function of $\cos\theta$ for σ° in natural units (m^2/m^2) and

$$\bar{\sigma}^{\circ} \text{ trees} = 10 \log (10^{-1.143} \times \cos\theta), \text{ dB} \qquad (4.18)$$

Radar backscatter from small water bodies is modeled after data acquired by the University of Kansas MAS 1-8 system in the spring of 1980.

These data were obtained at a frequency of 4.9 GHz for a pond roughly 1.5 acres in size with winds varying between 10 and 25 mph. The wind conditions are representative of conditions common to the simulated test area and produced waves of 1- to 2-cm in amplitude. A third-order polynomial fit to data acquired at 0°, 10°, 20° and 30° is assumed to be valid for wave conditions on the rivers and streams within the simulation.

$$\bar{\sigma}^{o} \text{ water} = 22.82 - 5.126\theta + 0.237\theta^{2} - 3.973 \times 10^{-3}\theta^{3}, \text{ dB} \qquad (4.19)$$

4.2.4 Angular Dependence of $\bar{\sigma}^{o}$ for Given Moisture Conditions

For each target class, local incidence angle θ_{ℓ}, and soil moisture condition generated within the image simulations, a given scene element is characterized by a $\bar{\sigma}^{o}$ from Equation 4.11 and Table 4.2 as influenced by signal scintillation. Figures 4.2 and 4.3 illustrate the behavior of $\bar{\sigma}^{o}$ for select target classes as a function of θ for M_{FC} equal to 10.0 and 150.0 respectively. M_{FC} = 10 is the driest moisture condition permitted in the simulation and is roughly equivalent to the hygroscopic coefficient of a given soil, while M_{FC} = 150 is the wettest moisture condition allowed and approximates a saturated soil condition.

4.3 Simulation Data Base Construction

The simulated data base corresponds to an 11 x 12 mile (17.7 km x 19.3 km) rectangular area immediately to the east of Lawrence, Kansas. The Kansas River flows across the northern half of the simulated region. This region was mapped into a matrix of approximately 1,000 x 1,000 pixels

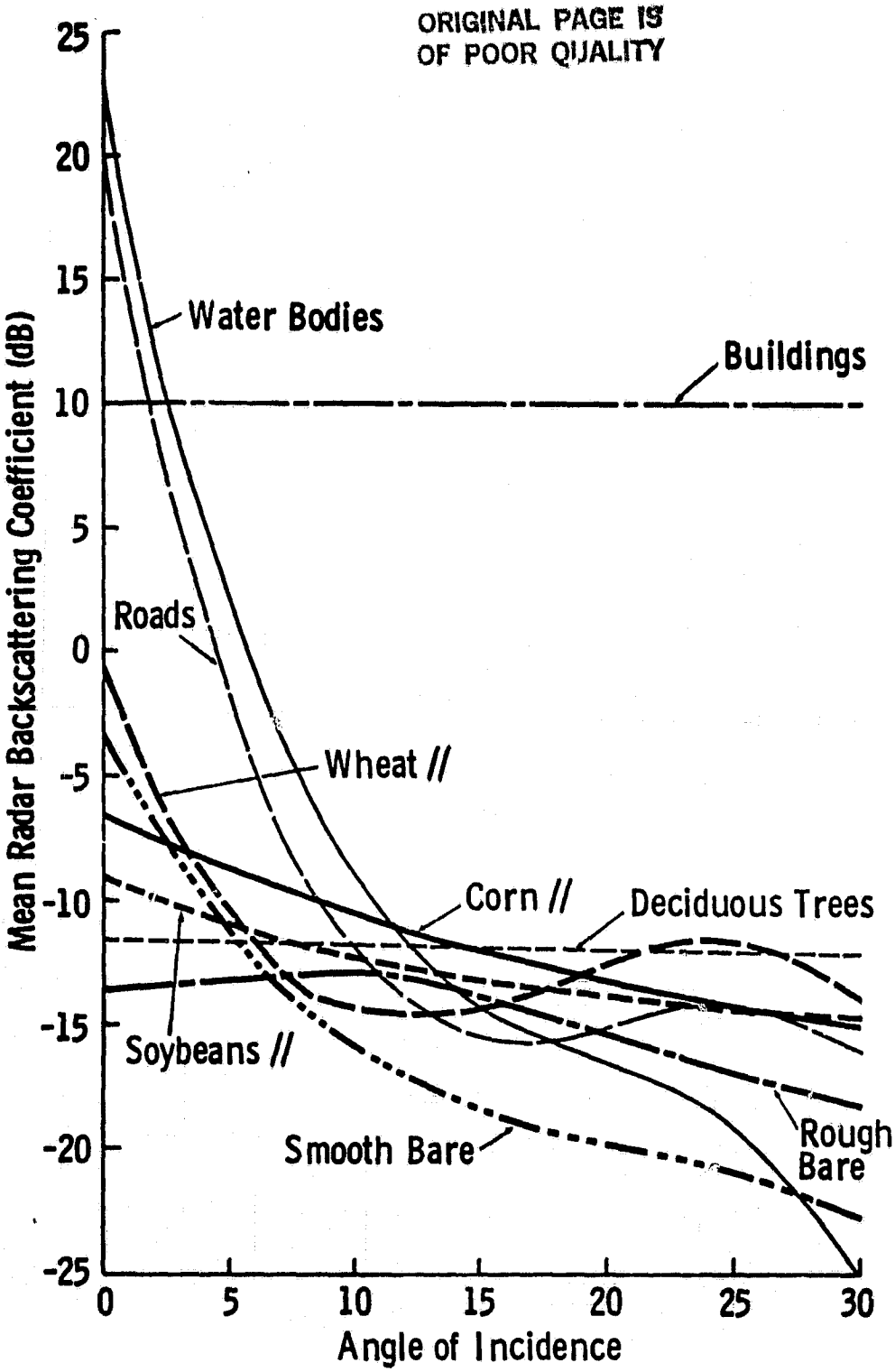

Figure 4.2 Mean Backscattering Coefficient of Several Target Classes as a Function of Angle of Incidence for Very Dry Soil Moisture Conditions, M_{FC} = 10.0%

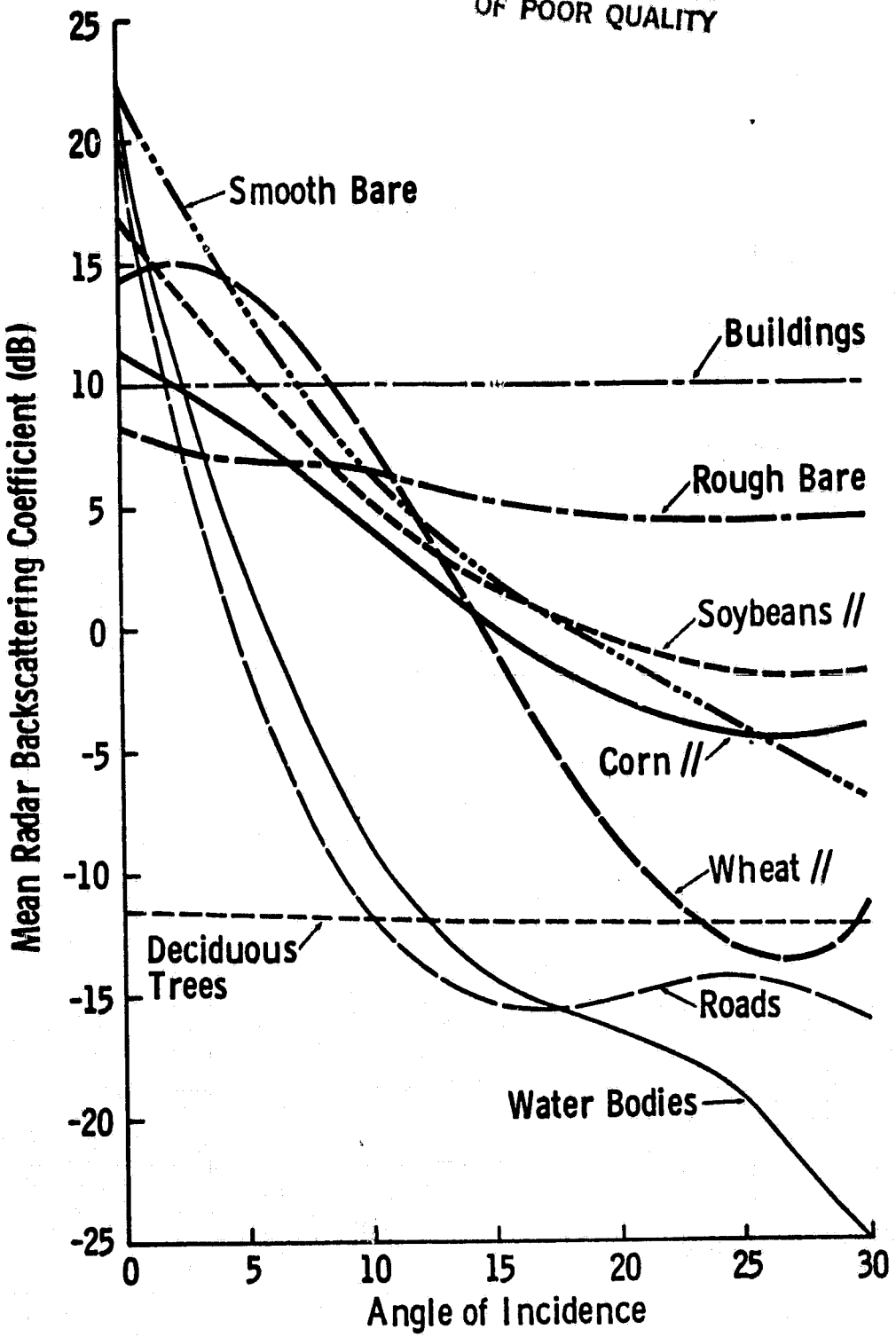

Figure 4.3 Mean Backscattering Coefficient of Several Target Classes as a Function of Angle of Incidence for Saturated Soil Moisture Conditions, M_{FC} = 150.0%

where each matrix element represents a ground resolution of 18 x 18 meters. A separate matrix was constructed for each of the following target parameters considered in the simulation: target category (Table 4.2), underlying soil texture, surface elevation, and incident rainfall from a simulated thunderstorm.

4.3.1 Target Categories

Target class data was extracted from color infrared U-2 imagery acquired in May, 1978. A positive color transparency of the 11 x 12 mile area was rephotographed into four quadrants as black and white negatives. Each quadrant could then be digitized into a 512 x 512 matrix on a CRT by use of a video camera.

Manual interpretation of the U-2 imagery as augmented by low altitude USDA/SCS imagery allowed assignment of a target class to each of the 512 x 512 pixel elements on each quadrant. A list of target categories used to characterize land use within the data base is given in Table 4.2. Figure 4.4 shows the U-2 imagery used in interpretation and Figures 4.5 to 4.7 show the data base as classified for various target categories.

Table 4.4 gives the percentage of the total 11 x 12 mile area assigned to each target class in the data base. Pasture comprises the largest single crop class in the data base and is followed closely by corn, bare soil, deciduous trees, and soybeans. The percents of the total planted area for each crop class in the data base are compared in Table 4.5 to those reported for Douglas County, Kansas [46] as a whole in 1977 and 1978.

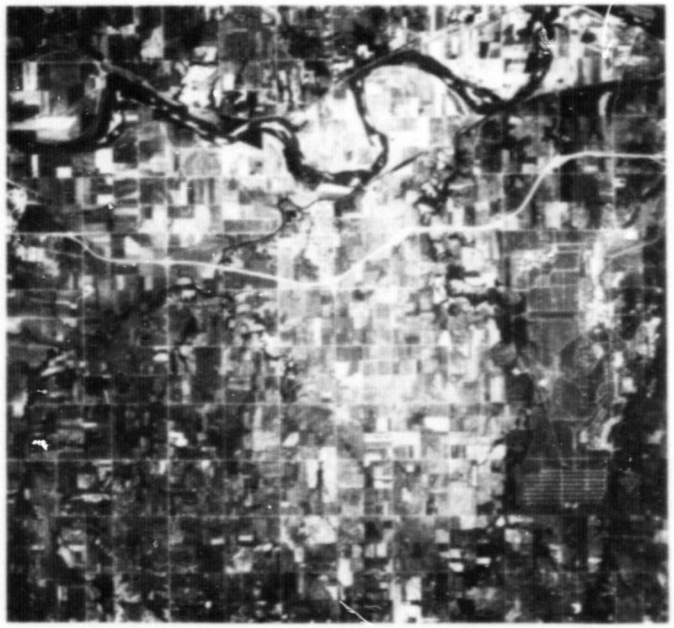

Figure 4.4 High altitude infrared imagery obtained May 15, 1978 and used to classify land use categories and field boundaries within the date base.

Figure 4.5 Location of non-agrigultural features within the simulation data base. Trees, highways, and secondary roads are shown in black; water bodies, railroads, bridges, and buildings are shown in white.

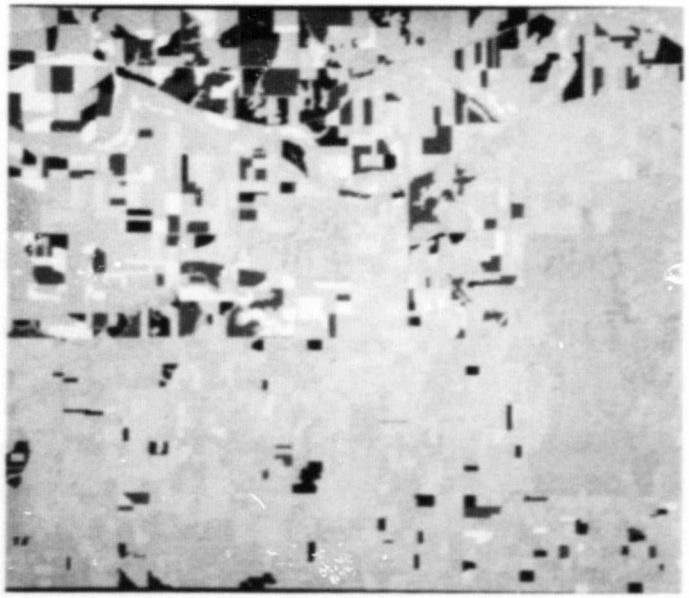

Figure 4.6 Location of bare soil fields within the simulation data base. Random surface roughness conditions from smooth to rough are proportional to image intensity.

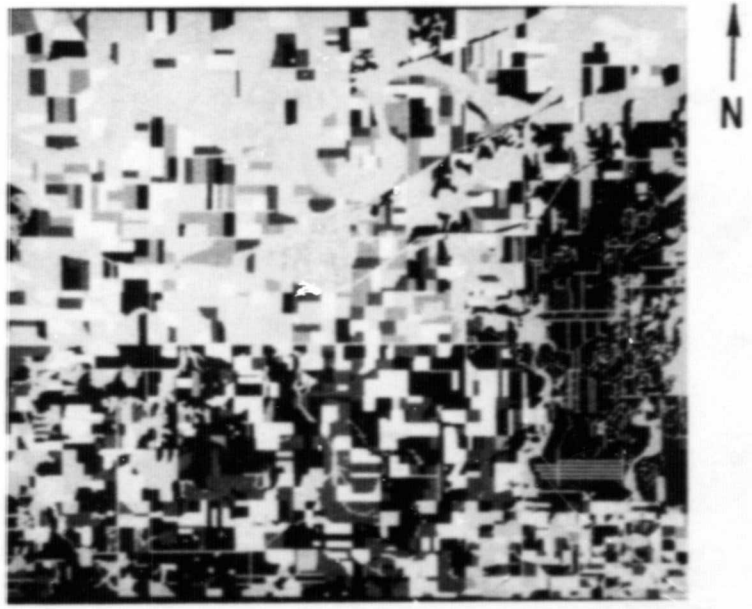

Figure 4.7 Location of vegetated fields within the simulation data base. Hay, pasture, soybeans, milo, corn, and wheat are shown with ascending image intensity.

TABLE 4.4

Area Percent of Total Data Base
Assigned to Each Target Class

Target Class	Percent of Total Area	
Roads	3.76	
Railroads	0.12	
River Bridges	0.01	
City Structures	0.85	
Rivers	2.19	2.67
Lakes, ponds, impondments	0.48	
Smooth Bare Soil	6.63	14.30
Medium Rough Bare Soil	4.92	
Rough Bare Soil	2.75	
Mown Pasture	7.06	
Pasture	15.93	
Alfalfa	4.15	
Wheat	6.65	
Sandbars	0.35	
Deciduous Trees	13.03	
Soybeans N/S Rows	5.46	11.08
Soybeans E/W Rows	5.62	
Milo N/S Rows	2.76	5.03
Milo E/W Rows	2.27	
Corn N/S Rows	8.32	14.93
Corn E/W Rows	6.61	

* N/S refers to crops planted with rows running north to south.
* E/W refers to crops planted with rows running east to west.

TABLE 4.5

Comparison of Data Base Composition with Historical Records for Douglas County, Kansas

Crop Class	% of Total Area Planted		
	Douglas County, Kansas [46]		Simulation Data Base
	1977	1978	
Corn	12.47	16.05	30.53
Milo	24.93	16.32	10.29
Soybean	12.47	25.57	22.66
Alfalfa	4.50	7.07	8.49
Wheat	23.55	9.07	13.60
Hay (Mown Pasture)	22.09	25.93	14.44

For the two years shown, the crop-mix of the data base compares favorably to that reported for all of Douglas County with certain exceptions. 30% of planted acreage in the data base is corn, while only 12% to 16% is reported for the county in 1977 and 1978. Conversely, only 10% of the planted acreage in the data base is milo while 16% to 25% is reported for the county as a whole. These discrepancies are expected since the Kansas River floodplain comprises a large portion of the data base. Much of the county's corn acreage is concentrated within the floodplain, while most of the milo acreage is in the upland areas typical of most of the county.

4.3.2 Soil Textural Classification

A digital matrix of soil textural class was constructed for all 18 x 18 meter pixel elements in the data base. United States Department of Agriculture Soil Conservation Service county soil surveys of Douglas, Jefferson, Johnson, and Leavenworth Counties in Kansas were the data sources [47,48,49,50]. A photo-mosaic of SCS imagery interpreted by SCS for mapping units of soil series and phase was re-interpreted on an acetate overlay for A-horizon soil textural class. Each SCS soil phase was classified as having one of the 10 soil textural classes or complexes given in Table 4.6. The acetate overlay was then photo-reduced into quadrants and digitized on the CRT. Figure 4.8 shows the digitized soil textural overlay for the simulation data base.

Each soil textural class was assumed to have characteristic sand, silt, and clay components as given in Table 4.6. These textural components were then used to determine a characteristic 1/3-bar water

TABLE 4.6

Soil Textural Classes, Their Area Percent, and Characteristic 1/3-Bar Water Contents Within the Simulation Data Base

Soil Textural Class	Textural Components			1/3-Bar Water Content* FC	Percent Area of Total Data Base
	% Sand	% Silt	% Clay		
Sand	92	5	3	.0644	0.1
Loamy sand	82	13	5	.0898	5.5
Sandy loam	65	25	10	.1365	4.3
Loam	40	40	20	.2110	18.0
Silt loam	20	65	15	.2420	35.4
Silty clay loam	10	57	33	.3076	13.1
Silty clay	7	47	46	.3375	3.3
Clay loam	33	34	33	.2543	13.0
Complex (50% loam and 50% silty clay loam)	25	48.5	26.5	.2568	0.7
Complex (50% silt loam and 50% silty clay loam)	15	61	24	.2723	6.6

*1/3-bar water content is expressed as a weight percent of dry soil.

Figure 4.8 Soil classes within the simulation test site. Pixel intensity is related to A-horizon soil texture from Table 4.6 where sand is darkest and complexes are brightest. The image represents a sampling of every other column and row of the entire data base (25% sample).

content from Equation 4.12 for each soil textural class. The area percent of the total data base represented by each soil textural class is also given in Table 4.6.

4.3.3 Surface Elevation

The distribution of surface elevation above mean sea level was encoded into the data base through procedures similar to those used for soil texture. In this case, the source data were United States Geological Survey 7.5 minute series topographic maps. An acetate overlay was made from a mosaic of the following quadrangles in Kansas:

Lawrence East Quadrangle

Baldwin City Quadrangle

Eudora Quadrangle

Edgerton Quadrangle

DeSoto Quadrangle

Gardener Quadrangle

While these quadrangles have 10-foot contour intervals, it was generally necessary to construct the overlay with 20-foot contour intervals in the hill regions enveloping the river floodplain. In order to compute a realistic range to each pixel, area of each pixel, and local angle of incidence, it was necessary to convolve the digital elevation data to produce local surface slope. The convolution procedure is treated in a later section.

Figure 4.9 gives a shaded relief presentation of the final elevation matrix after convolution. Intensity of each pixel element is related to elevation above mean sea level.

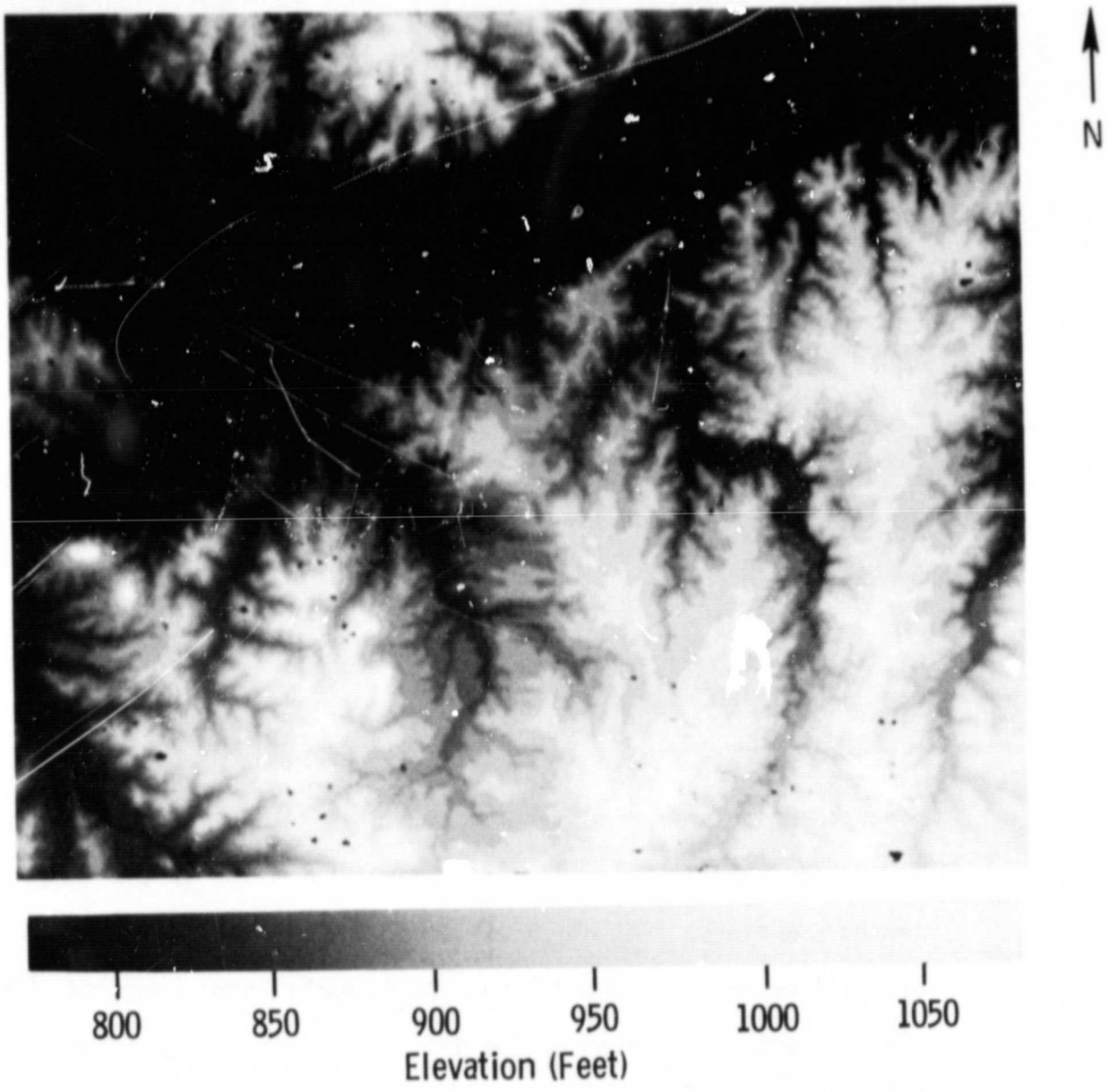

Figure 4.9 Elevation above mean sea level. Every other column and row of the total data matrix are samples to produce this image.

4.3.4 Data Base Registration

The initial digital data base consisted of matrices for target class, soil texture, and surface elevation in four quadrants each. A set of 8 to 12 registration points had been preselected within each quadrant. An nth order polymomial fit to the registration points established a warping function for mapping all soil texture and surface elevation matrices into the coordinate system of the corresponding target class matrix. This process corrected for any lack of geometric equivalence in the raw data sources and any scaling differences arising from the digitization procedure. Upon completion of the warping, all four quadrants were then mapped into a common coordinate system, aligned, and overlap data were deleted from the composite data base.

4.4 Simulation of Slope

The elevation data base which was described previously consists of discrete heights in a matrix format. This matrix is operated upon by the simulation algorithms to produce slope information in the range and azimuth dimensions, from which the local angle of incidence between the radar antenna and the ground sample location is later computed. That is, for each and every entry in the ground-truth data base a facet orientation is generated, with the terrain slopes between sample points modeled by linear interpolation of elevations in range and azimuth.

If we define the angle of the slope in azimuth as ρ and the angle of the slope in the range directions as ψ, then the local angle of incidence θ_ℓ is given as

$$\theta_\ell = \cos^{-1} \frac{\tan\psi \sin\theta + \cos\theta}{\sqrt{\tan^2\rho + \tan^2\psi + 1}} \qquad (4.20)$$

assuming a side looking antenna. The angle of incidence θ is defined as previously, in section 4.1.3, as the earth curvature corrected incidence angle.

Taking several examples, we see that if ψ and ρ are both small (level terrain cases), then $\theta_\ell \simeq \theta$. If the ground is hilly, then foreslopes (ψ positive) and backslopes (ψ negative) are present. For ψ positive and ρ small, the local angle of incidence can approach zero degrees and the foreslope backscatter can become quite large. For ψ negative and ρ small, the local angle of incidence can approach grazing ($\theta_\ell \simeq 90°$) and the backscattered signal has a small amplitude. The shadow case arises when a backslope has a value of $|\psi| > \theta$, and no signal is backscattered from the shadowed terrain.

In the situation of general terrain, the local slope treatment can be summarized by saying that a facet model slope in range and azimuth is calculated, based upon linear interpolation between elevation samples. Since power backscattered is computed on the basis of the resolution of the data base (as opposed to the sensor resolution, which may be greater than the 20-m data base resolution achieved herein) then the facets are smaller than the resolution cells of the sensor in general.

A random model for tree heights was employed to achieve realistic conditions of natural growth. In the geometry calculations the random tree heights were incorporated such that the presence of taller trees could give rise to layover and shadow, which is commonly seen in very high resolution radar imagery. That is, the random tree heights were calculated before processing of other geometric effects took place.

4.5 Simulation of Rainfall and Soil Moisture Conditions

In order to produce realistic simulations, four hypothetical soil moisture distributions were developed for the 0-5 cm soil layer. These distributions cover the full range of potential moisture conditions from saturation of the soil to a drought-like condition. With respect to time, the hypothetical moisture conditions cover a 35-day time span with simulated satellite overpasses on Days 4, 5, 15, and 35.

4.5.1 Soil Moisture Conditions

For each satellite overpass, the "actual" moisture M_{FC_N} of each 18 x 18 meter pixel element in the data base is established from a hypothetical rainfall and evaporative history. The objective is to establish a set of moisture conditions for each radar simulation that is a reasonable facsimile of common "real world" conditions. In order to simplify the calculations, and because of a lack of adequate source data, several assumptions are made. First, the hydraulic conductivities of all soil textural classes in the data base are assumed to be equivalent. The bulk densities of all soils are assumed to be 1.0 g/cm^3 within the 0-5 cm soil layer. In addition, the evaporation rates from all soils and crop classes are assumed to be equal although still time dependent. In actuality of course, bulk density, evaporation rate, and hydraulic conductivity all vary as functions of many variables including soil texture, crop class, and soil moisture.

For each 18 x 18 meter pixel, soil moisture M_{FC_N} is computed from the general expression:

$$M_{FC_N} = M_{FC_{(N-1)}} + 100(M_{V_N}/FC_{vol}) \qquad (4.21)$$

where

M_{FC_N} = % of 1/3 bar water content for the N^{th} simulation

M_{V_N} = the change in volumetric water content since the time of the (N-1) simulation, g/cm^3

FC_{vol} = estimated 1/3 bar water content, g/cm^3.

Since soil bulk density is assumed to be 1.0 g/cm^3, then

$$FC_{vol} = 1.0 \times FC \tag{4.22}$$

for values of FC given in Table 4.6 for each soil texture. In addition, M_{V_N} is dependent upon incident rainfall, surface and subsurface drainage, and evaporation.

$$M_{V_N} = M_{V_{(N-1)}} + M_{rain} - M_{evap} \tag{4.23}$$

where

$M_{V_{(N-1)}}$ = initial volumetric soil moisture

M_{rain} = net increase in M_V due to precipitation, g/cm^3

M_{evap} = net loss in M_V due to evaporative demand, g/cm^3

Since soil bulk density is assumed equal to 1.0 g/cm^3, M_{rain} and M_{evap} can be calculated from incident rainfall and evaporation rate by:

$$M_{rain} = (\text{Precipitation} - \text{Drainage})/\text{Soil Depth} \tag{4.24}$$

and

$$M_{evap} = (\text{Evaporation rate} \times \text{elapsed time})/\text{Soil Depth} \tag{4.25}$$

where precipitation, drainage, and soil depth are in cm and evaporation rate is in cm per day.

4.5.2 Postulated Rainfall and Evaporative History

During the first day of the 35-day time span, a steady and heavy rain is assumed to have produced saturated soil moisture conditions over the entire data base. Over the next three days, water in excess of field capacity (as estimated by the water retention of a given soil at 1/3 bar) is assumed to have drained from the upper 5 cm of soil throughout the data base. Thus a satellite overpass on Day 4 observes all soils with M_{FC} equal to 100% of 1/3-bar water content.

Less than a day after the first simulated radar overpass, a hypothetical convectional thunderstorm passes from west to east across the data base. The storm deposits a Gaussian rainfall distribution with maximum incident rainfall of 2.5 cm along the center of the storm track and with a minimum approaching 0.0 cm along the northern and southern edges of the data base. Limited hydraulic conductivity of the soil causes all incident rainfall in excess of 1.25 cm to drain laterally from the soil as surface runoff. Any incident rainfall less than 1.25 cm is assumed to percolate rapidly into the upper 5 cm of soil. Thus, immediately after passage of the thunderstorm, maximum M_{rain} is 0.25 g/cm^3 from Equation 4.24. A satellite overpass of the data base several hours after passage of the thunderstorm could be expected to observe a soil moisture distribution similar to the one defined above for Day 5 and used in the second radar simulation.

During the following 10 days the upper 5 cm of soil dries due to evaporation at a rate of 0.1 cm of water per day. There is no additional rainfall. Thus M_{evap} is a constant 0.2 g/cm^3 over the data base from Equation 4.25. In addition, it is assumed that for any given pixel element $M_{FC_N} \geq 25.0\%$ of 1/3-bar water content on Day 15. This assump-

tion reflects the capacity of most soils to replenish some portion of daytime evaporative loss during the night through capillary recharge and vapor flow. A lower limit of 25% on surface moisture also functions to prevent unnaturally dry moisture conditions in the simulation which otherwise could approach or exceed "oven dryness" at 0% M_{FC} for sandy soils in the data base which have small volumetric water retentions at 1/3 bar. Thus, a simulated radar overpass on Day 15 observes soil moisture conditions with a maximum M_{FC} of approximately 90% and a minimum defined at 25%.

From the third simulation until the end of the 35-day period there is no additional precipitation, hence M_{rain} equals 0.0 g/cm^3. Since, at low surface-moisture conditions, evaporative rate is limited by the availability of near-surface water, the evaporation rate for this 20-day period is assumed to be reduced to 0.05 cm of water per day. As a result, M_{evap} in Equation 4.25 becomes 0.2 g/cm^3. In order to prevent M_{FC} of sandy soils from becoming zero, a lower limit of M_{FC} = 10% is assumed to be valid on Day 35. Moisture conditions of 10% of 1/3-bar water retention approximates the hygroscopic coefficient of many soils and moistures less than this value are not readily attained under natural field conditions. Thus, a simulated radar overpass on Day 35 observes moisture conditions which range between 32% and 10% of the 1/3-bar water retention in the 0-5 cm layer. Such moisture levels are typical of those observed within the data base region during droughts in 1975 and 1976.

The given moisture conditions for the four simulations as described above are tabulated in Table 4.7. Figures 4.10 to 4.13 show an image presentation of the moistures input into the simulations. Roads, build-

TABLE 4.7

Values of Rainfall and Evaporation Used to Derive the Hypothetical Soil Moisture Conditions

Simulation Number N	Day Number	Rainfall (cm)	M_{rain} g/cm³	Mean Evaporative Rate cm/day	Number of Elapsed Days	M_{evap} g/cm³	M_{FC_N}, % of 1/3-Bar Water Content	Estimate M_{FC_N}	
								Max.	Min.
1	4	Not Determined	>>FC	Not Determined	3	-	$M_{FC_1} = 100.0$	100.0	100.00
2	5	≤ 2.5	≤0.25	Not Determined	0	0.0	$M_{FC_2} = M_{FC_1} + 100(M_{rain}/FC)$ and $M_{FC_2} \leq 150.00$	150.0	100.0
3	15	0	0	0.1	10	0.2	$M_{FC_3} = M_{FC_2} - 20/FC$ and $M_{FC_3} \geq 25.0$	90.7	25.0
4	35	0	0	0.005	20	0.2	$M_{FC_4} = M_{FC_3} - 20/FC$ and $M_{FC_4} \geq 10.0$	31.5	10.0

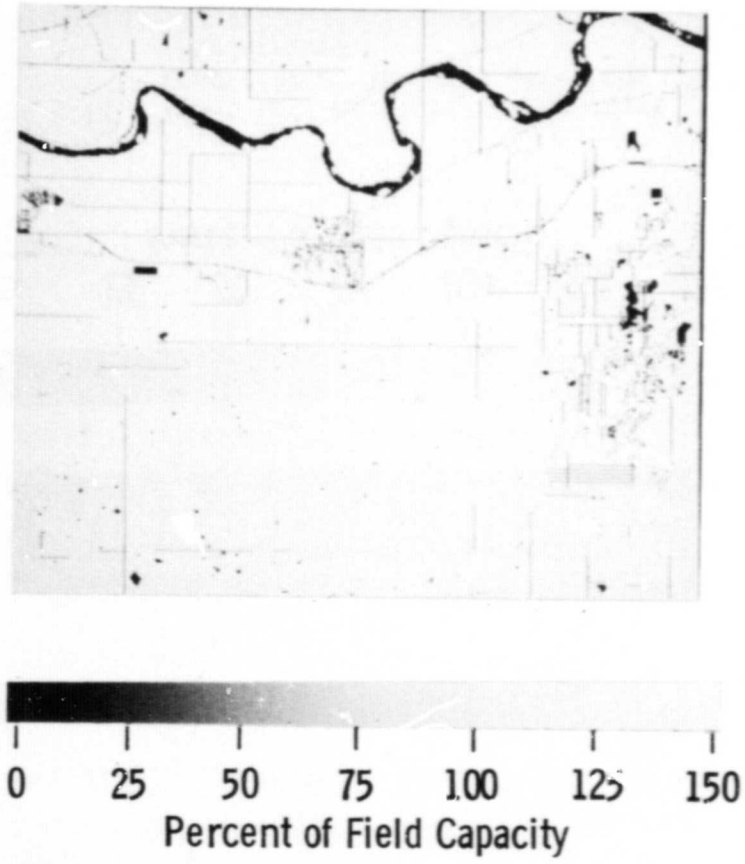

Figure 4.10 Input soil moisture for Moisture Condition 1, three days after a saturating rain. All soils are at 100% of field capacity.

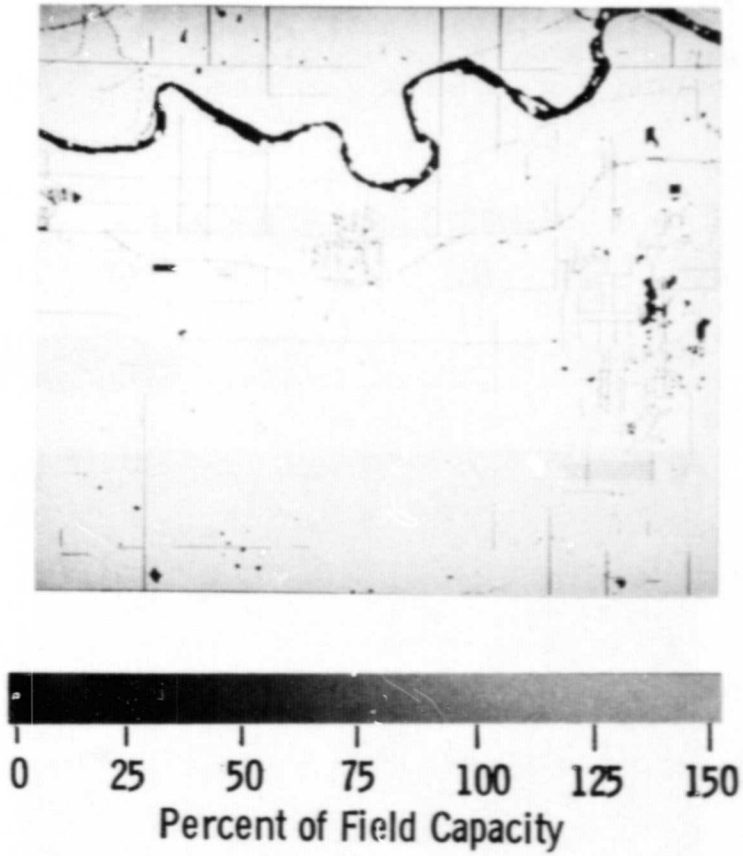

Figure 4.11 Input soil moisture for Moisture Condition 2, immediately after passage of a thunderstorm. Surface soil moisture ranges from field capacity to saturation.

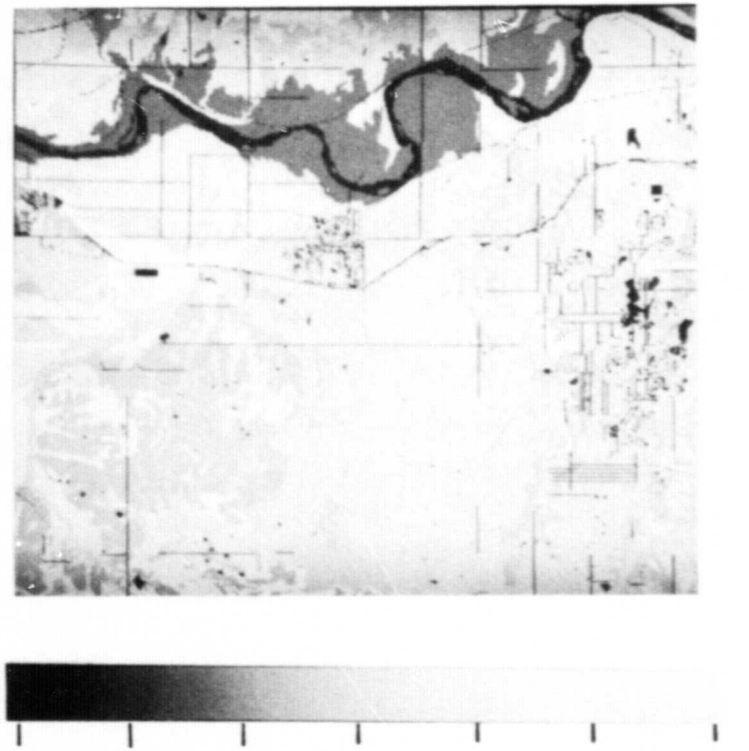

Figure 4.12 Input soil moisture for Moisture Condition 3, ten days after the thunderstorm.

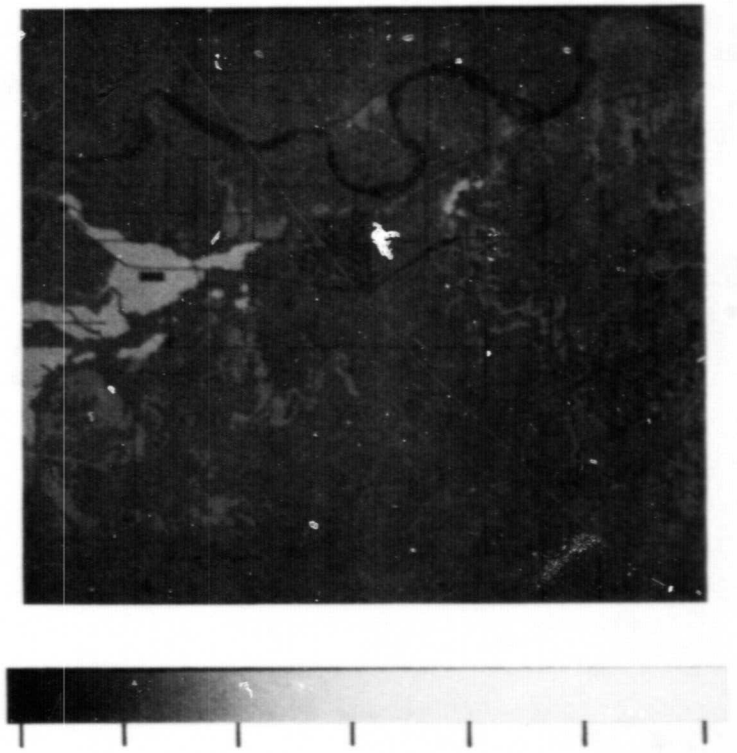

Figure 4.13 Input soil moisture for Moisture Condition 4, thirty days after the thunderstorm, drought conditions.

ings, and water bodies are shown in black on these figures since soil moisture is undefined for these categories and greytone level is proportional to M_{FC}.

4.6 Generation of Radar Images - Summary of Computer Algorithms and Images

The computer algorithms that produce the simulated radar images, given the backscatter data, ground truth data base, and sensor parameters, are broken into four major packages. They handle the following aspects of the process: (1) measuring the average value of the received power for each range gate, (2) Monte Carlo simulation of the fading, (3) averaging to trade spatial for radiometric resolution, and (4) scaling of the image data. We shall discuss these four steps briefly; the reader is further directed to [28] for greater detail.

The simulation package mimics portions of the operation of a SAR for which digital processing is to be used. As such, a certain number of range gates are set up; in this case we wished to produce a ground range simulated image, so the gates are not of equal length across the image. (They monotonically increase in size with increasing incidence angle.) Next, the facet orientation calculations are performed for each point in the data base, and range to each facet is obtained. In order to determine whether a location is in shadow, it is necessary to make neighborhood elevation comparisons, and this is done next.

The "start" and "stop" ranges which mark the beginnings and endings of each range gate, having been determined previously, are available for approximating how much of each facet's return power will fall into a certain range bin. As the software exists at present, if the range to a

certain data base location equals the ending range of bin "K," then its power is equally divided between bins K and K + 1, and so forth for other proportions. The power referred to here is the average power determined by the radar equation [29] which accounts for antenna gains, diffraction losses, scattering cross-section, and wavelength of illumination.

Through the explicit computation of range bin stop and start ranges (or equivalently, times), the geometry/propagation factors of earth curvature, foreshortening, and layover are automatically incorporated. An efficient binary search routine is actually used to determine when a facet's power will be received.

There are certain measurable system parameters including transmitted power, antenna gain, wavelength, Doppler weightings, incidence angle, scale and bias factors, etc. in the SAR data processing that perhaps could be removed in effect from the radar imagery that would allow one to use a soil moisture algorithm directly on the digital SAR image. Thus, the decision was made that the average received power would be calculated as

$$\bar{P}_R = \frac{c\,\sigma^{0}(\theta_\ell)\,A}{R^4} \tag{4.26}$$

where c incorporates all the factors excluded from the radar equation [29], and, furthermore, a reference range to the fourth power, to prevent $\bar{P}_R$ from being very small.

The above description has treated the problems of average power and geometry considerations, and concludes the discussion of the first of four packages of the simulation algorithms, as tailored to this particular project.

The second of the four packages accounts for fading, which is the major source of noise for small time-bandwidth product sensors. The model derived in [33] is used to generate received power from average received power through Monte Carlo simulation as

$$P_R = \frac{\bar{P}_R}{2N} \cdot y \tag{4.27}$$

where $y \sim \chi^2_{2N}$, that is, y is described by a chi-square distribution with 2N degrees of freedom. When a small number of independent samples is desired, (say, $N < 5$) Equation (4.27) provides a simple route for simulation of the faded received power (the sum of the squares of the in-phase and quadrature voltage signals received). However, when large N images were needed, spatial domain smoothing to sacrifice resolution for looks was applied to a small N image. The spatial domain implementation of the continuous scanning mixed integration process [28] was used for these types of images. For N = 12 images a Gaussian approximation to the multiplicative model of Equation (4.27) was used to produce values of P_R.

$$P_R = \bar{P}_R \left(1 + \frac{Z}{\sqrt{N}}\right) \tag{4.28}$$

where $Z \sim \mu(0,1)$, that is, Z is distributed as a Gaussian with mean zero and unity variance.

The third of four packages of the simulation performs smoothing in either or both of the dimensions of the radar images. In several cases it was possible to use the same image several times, at its finest possible resolution and small N, and then at degraded resolutions and larger values of N. In all cases, the convolution weightings were obtained by

derivation of the filters whose structures are described and justified in [28].

The fourth package of the simulation software simply took the values of power produced by Packages 1, 2 and 3, and converted them to densities through a logarithm operation, i.e., $D = 10 \log P_R$. This step was incorporated simply to make the simulated images compatible with the soil moisture estimation algorithm.

A summary of the simulated images is given in Table 4.8. In all, a set of 24 images was produced for 3 resolutions x 2 angular ranges x 4 moisture conditions. Samples of these images are given in Figures 4.14 to 4.22 for selected conditions. Image graytone G_I is scaled from 0 to 255 and is proportional to received power in dB over a 50 dB dynamic range from -25 dB to +25 dB.

$$G_I = 5(10 \log P_R + 25) + 3 \qquad (4.29)$$

Simulated images for the 20-meter resolution case over the 7.5° to 9.3° angular range are shown in Figures 4.14 to 4.17 for moisture conditions of field capacity, saturation, drying, and drought, respectively. The drying condition (Moisture Condition 3, 10 days after the hypothetical thunderstorm) is used as a case example of the effects of changing resolution and angular range in Figures 4.18 to 4.22. Because of matrix-size constraints on the video display screen, all images show a 25% sample of the total data base, wherein every other column and row of the total digital matrix is imaged. As a result, certain linear features such as roads may appear to be discontinuous on the images.

5.0 EVALUATION OF RESULTS

The simulated satellite radar data was evaluated for its capacity to correctly estimate the actual data-base moisture conditions given in Section 4.5. Each of 24 simulations (2 angular ranges x 3 resolutions x 4 moisture conditions) were interpreted by a generalized moisture

TABLE 4.8

Summary of Simulated Radar Images

N of Looks	Radar Pixel at Mid-Range Angle $r_a \times r_y$ (m x m)	Angular Range θ
12	20 x 20	7.5°-9.3°
12	20 x 20	11.1°-12.8°
23	93 x 100	7.5°-9.3°
27	93 x 60	11.1°-12.8°
2250	1,000 x 1,000	7.5°-9.3°
2800	900 x 600	11.1°-12.8°

All cases have simulated soil moisture conditions of: field capacity, saturation, drying, and drought.

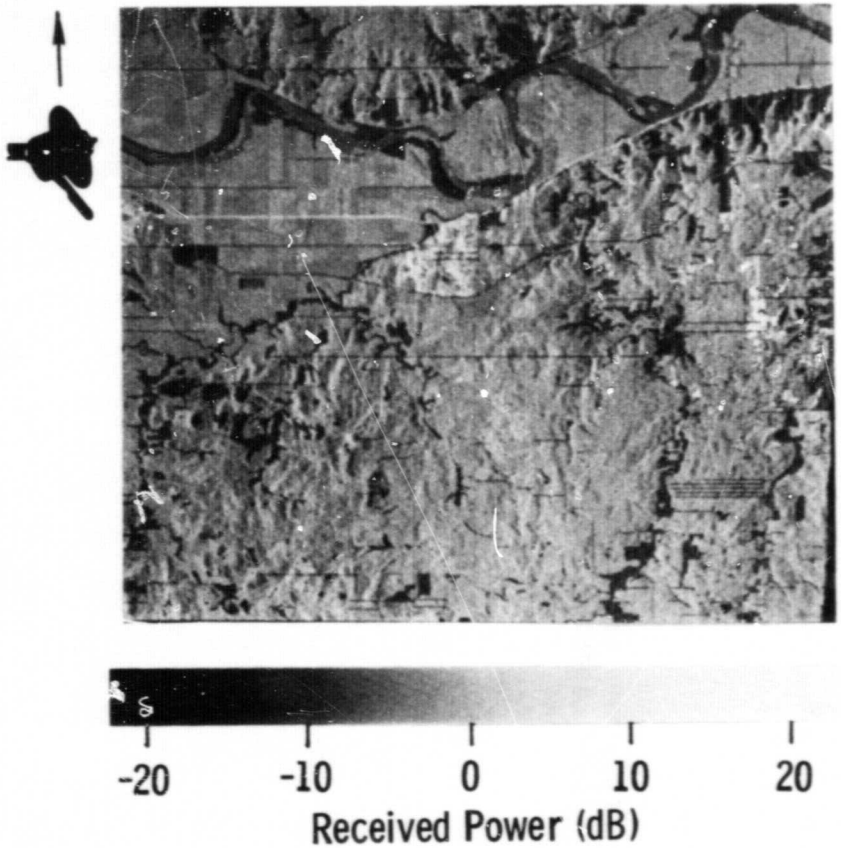

Figure 4.14 Radar simulation with 20-meter resolution and 7.5° angle of incidence for Moisture Condition 1, all soils at field capacity.

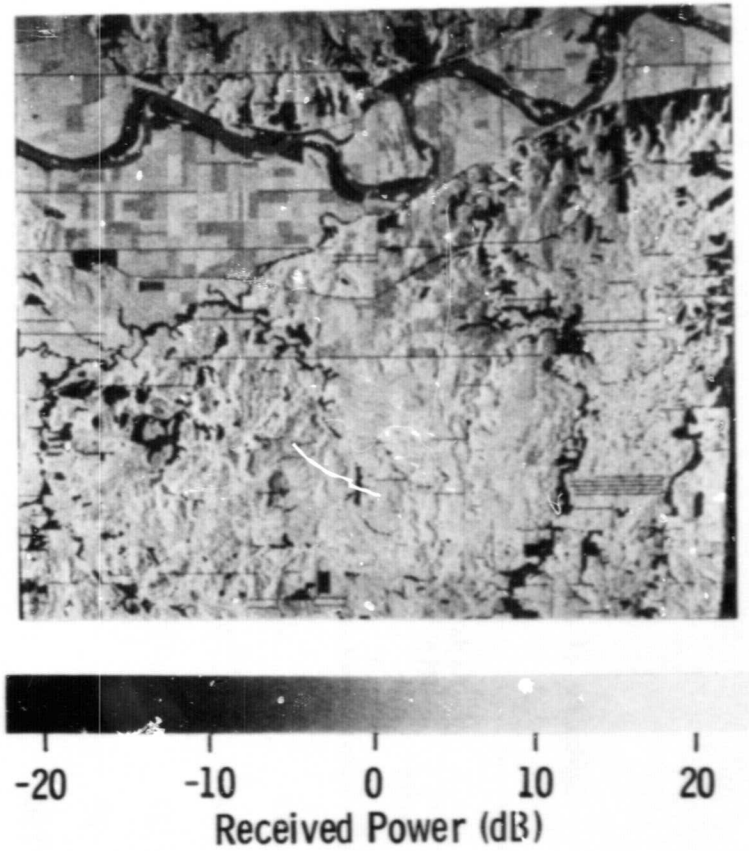

Figure 4.15 Radar simulation with 20-meter resolution and 7.5° angle of incidence for Moisture Condition 2, immediately after a thunderstorm.

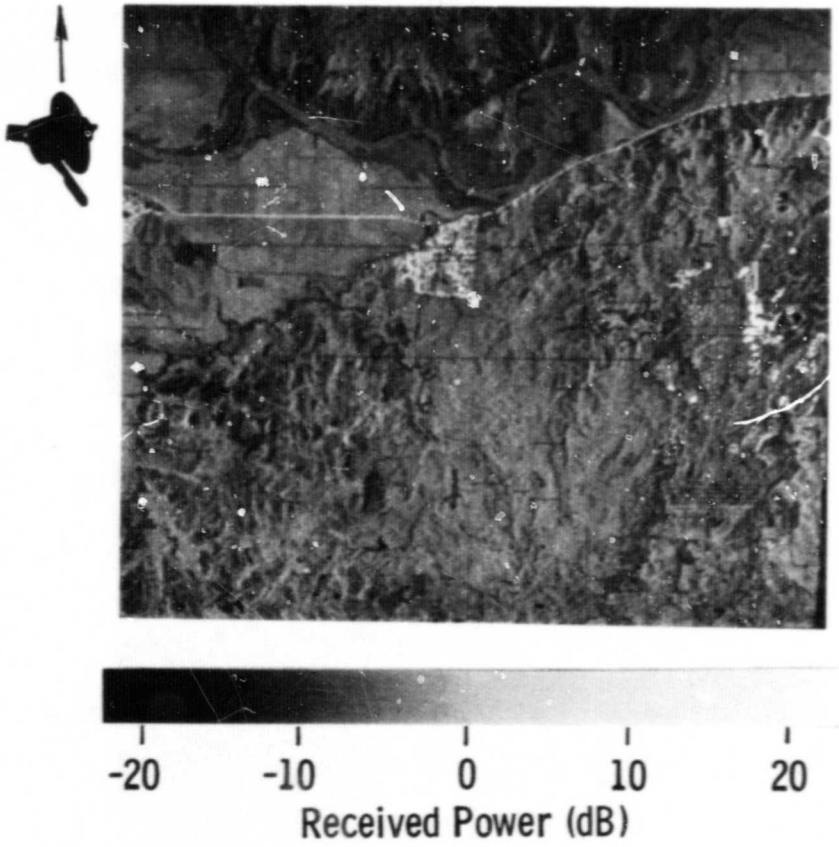

Figure 4.16 Radar simulation with 20-meter resolution and 7.5° angle of incidence for Moisture Condition 3, 10 days after the thunderstorm.

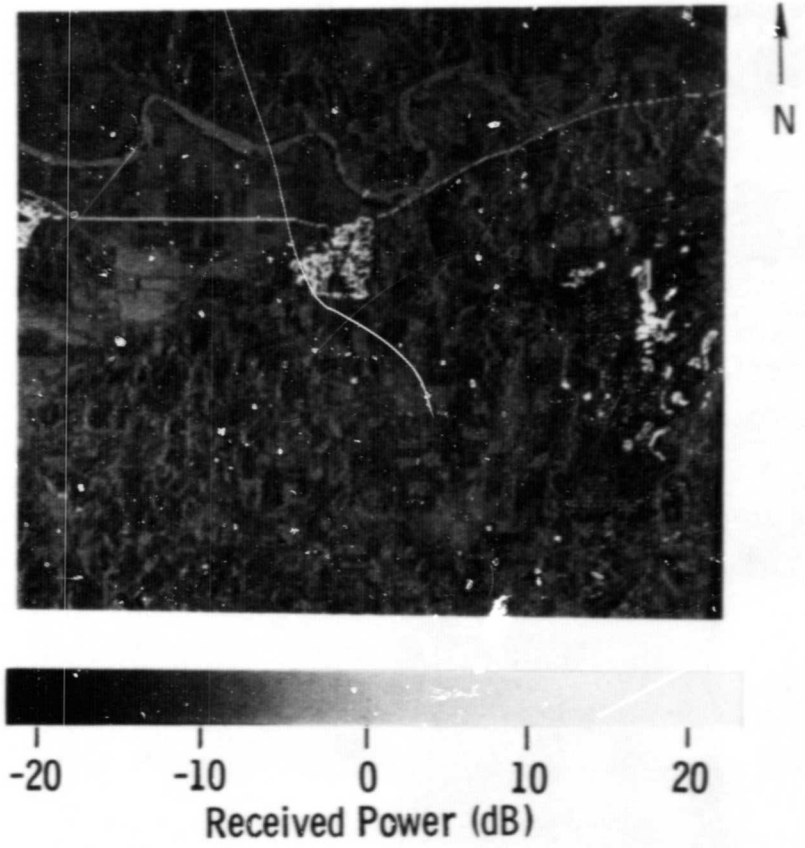

Figure 4.17 Radar simulation with 20-meter resolution and 7.5° angle of incidence for Moisture Condition 4, 30 days after the thunderstorm.

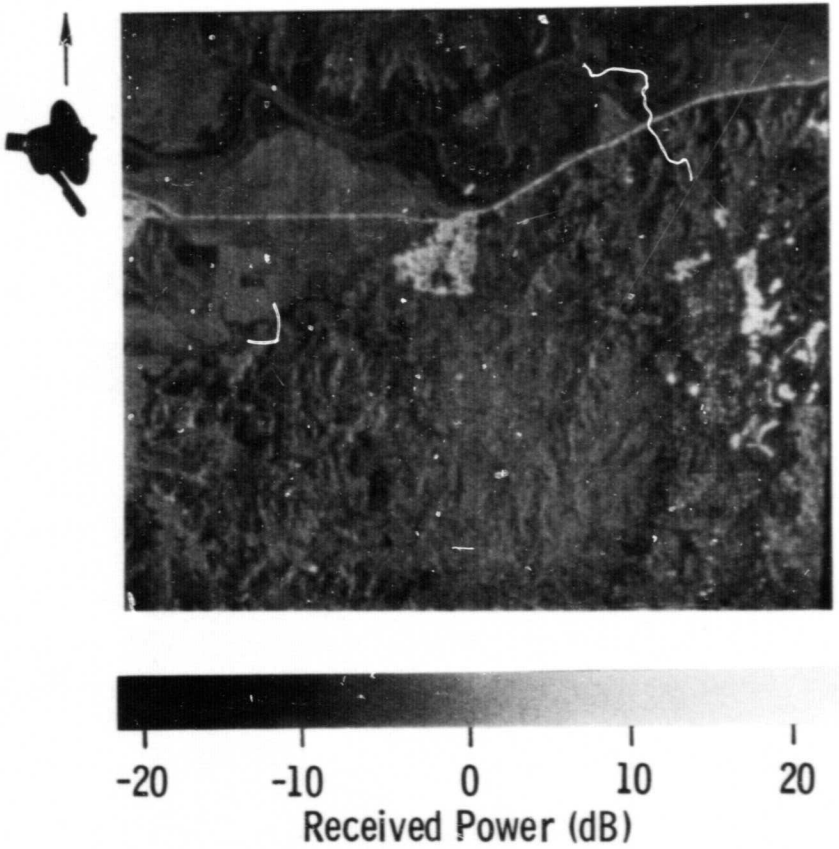

Figure 4.18 Radar simulation with 100-meter resolution and 7.5° angle of incidence for Moisture Condition 3, 10 days after the thunderstorm.

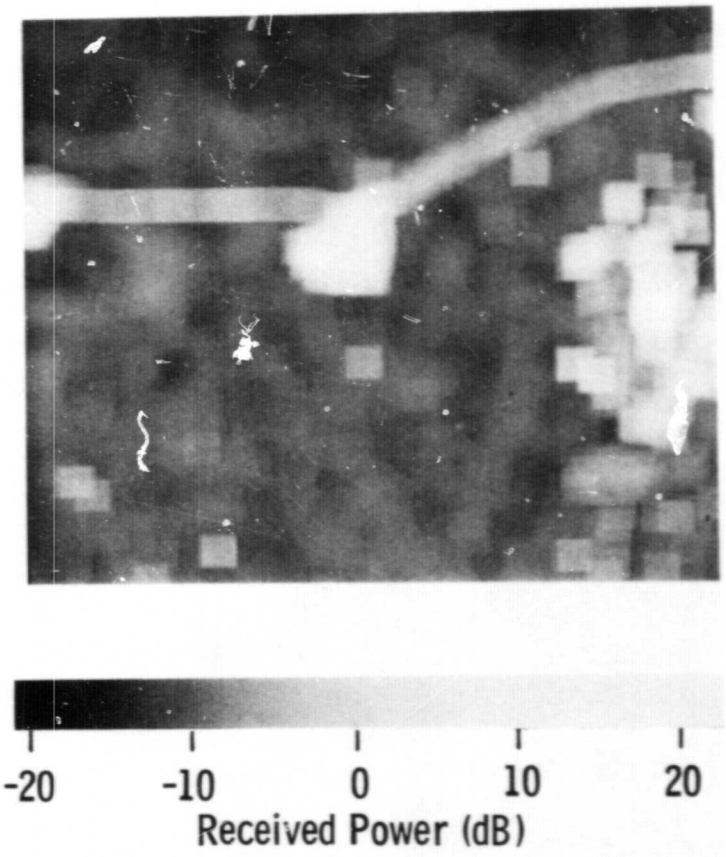

Figure 4.19 Radar simulation with 1-kilometer resolution and 7.5° angle of incidence for Moisture Condition 3, 10 days after the thunderstorm.

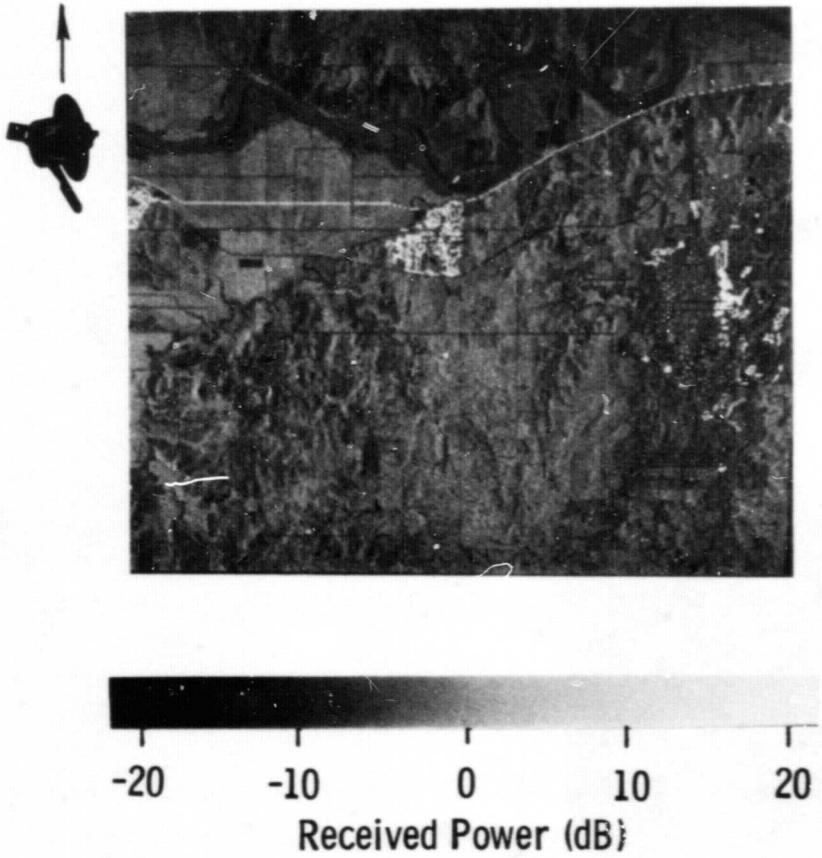

Figure 4.20 Radar simulation with 20-meter resolution and 11.1° angle of incidence for Moisture Condition 3, 10 days after the thunderstorm.

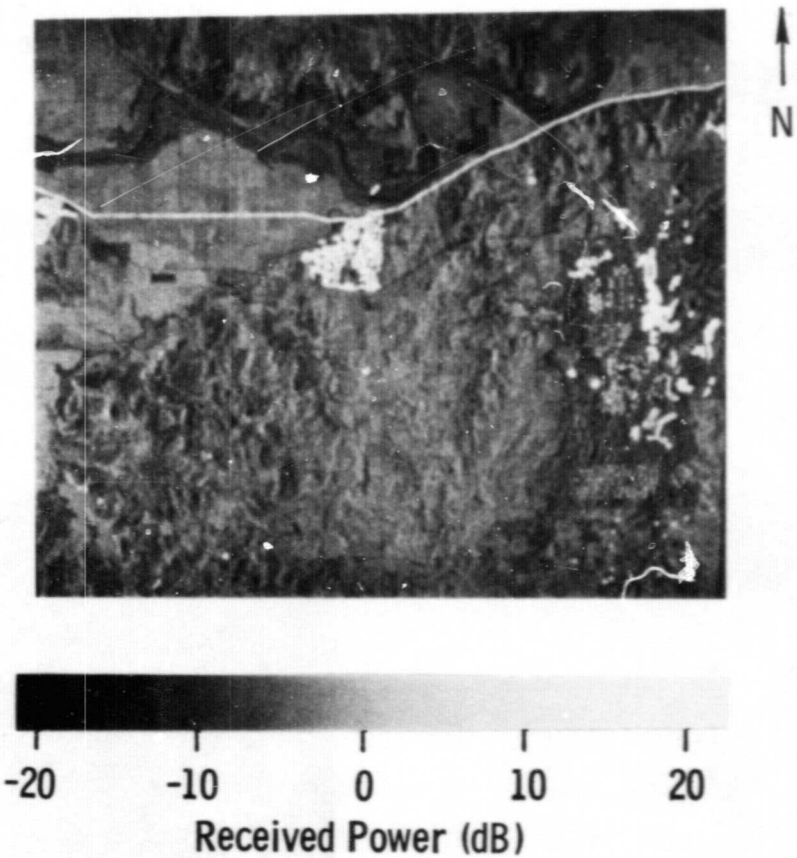

Figure 4.21 Radar simulation with 100-meter resolution and 11.1° angle of incidence for Moisture Condition 3, 10 days after the thunderstorm.

Figure 4.22 Radar simulation with 1-kilometer resolution and 11.1° angle of incidence for Moisture Condition 3, 10 days after the thunderstorm.

algorithm $A(\theta)$ to estimate $\hat{M}_{FC}$ for each resolution cell. Estimated moisture $\hat{M}_{FC}$ was then correlated with actual moisture M_{FC} to establish estimate accuracy for a given simulation. This was accomplished using a digital processing scenario for the simulated radar data, although image processing of the quantized radar data should produce similar results.

Evaluation of sensor performance in terms of moisture estimate accuracy proceeded at several levels dependent upon the assumed availability of ancillary data. Ancillary data includes:

1. known location of water bodies, buildings, roads, and bridges;
2. *a priori* information about whether an agricultural scene is bare soil or covered with a crop canopy.

Knowledge of position and extent of water bodies, buildings and roads could be the product of a manually or machine-interpreted image from one of the simulated radars, some other image source, or digital map data base. Agricultural crop-cover information may be obtained through the use of local crop calendars or may be obtained from crop discrimination from Landsat and/or a satellite radar operating at $\tilde{\sim}$ 14 GHz with 50° incidence angle.

For the simple case where there is no ancillary data concerning the imaged area, the simulated backscatter data is interpreted using a blind classifier to estimate moisture $A(\theta)$. In this case, all simulated image elements are interpreted by the generalized algorithm as containing valid surface soil moisture information.

In the second case, where the positions of water bodies, buildings, and roads are assumed to be known, the pixel elements representing these features are filtered from the simulated backscatter data and therefore

not assigned a soil moisture estimate $\hat{M}_{FC}$. In this approach, the evaluation of estimate-accuracy is less biased by the misinterpretation of cultural features and water bodies as agricultural scenes, since the generalized moisture algorithm pertains only to agricultural scenes and soil moisture is undefined for water bodies and hard targets.

The third case, in its simplest form, permits the division of agricultural-scene data into that representing bare soil and that representing any crop canopy. Of course, if complete crop discrimination were assumed as auxiliary data then the return from each identifiable crop cover category could be treated independently. The simulation evaluation procedure treated herein covers only the first two cases and the simple form of the third where two generalized algorithms are used to interpret the backscatter data, one algorithm $B(\theta)$ for generalized bare soil conditions and one algorithm $C(\theta)$ for generalized crop canopy conditions.

5.1 Generalized Moisture Interpretation Algorithms

The generalized moisture algorithm $A(\theta)$ was developed for an amalgamation of all agricultural-scene data from sources as listed in Table 4.1. The available data were at frequencies between 4.25 GHz and 4.9 GHz and incidence angles between 0° and 30°. In addition, these same data sources were used to develop general moisture interpretation algorithms for all bare soil classes $B(\theta)$ as considered separately from all crop canopy classes $C(\theta)$.

The amalgamated data at each angle (0°, 10°, 20°, and 30°) was submitted to least-squares linear regression to establish the linear

dependence of σ^o on M_{FC}. The regression results are shown in Table 5.1 for all classes combined, bare soil classes only, and vegetation canopy classes only.

Scattergrams of σ^o as a function of M_{FC} for all agricultrual scene data combined are shown in Figures 5.1 and 5.2 for 10° and 20° incidence angles respectively. Linear correlation coefficient θ is observed to decrease from 0.88 at 10° to 0.65 at 20° and is felt to be caused by the increasing impact of canopy attenuation and canopy geometry at angles of 20° and greater.

Assuming normal distributions of σ^o and M_{FC} in Figure 5.1, the 90% confidence interval about $\hat{\sigma}^o$ is computed to vary from +/- 0.20 dB at M_{FC} = 75 to a maximum of +/- 0.53 dB at M_{FC} = 0 or 150. This means that 90% of the time $\hat{M}_{FC}$ should be within +/- 1.5% of the measured M_{FC} when $\hat{M}_{FC}$ = 75% and $\hat{M}_{FC}$ should be within +/- 3.9% of the measured M_{FC} when $\hat{M}_{FC}$ equals 150% or 0%. In a similar fashion, calculation of the 90% confidence interval about the linear regression at 20° (Figure 5.2) yields a .9 probability that measured M_{FC} is within ±3.2% of $\hat{M}_{FC}$ for $\hat{M}_{FC}$ = 75% and within +/- 8.7% of $\hat{M}_{FC}$ for the moisture extremes where $\hat{M}_{FC}$ = 0% or 150%.

Scattergrams of all bare soil cases are shown in Figures 5.3 and 5.4 for 10° and 20° respectively. These plots include 181 data points from 11 test fields where roughness ranges from RMS heights of 0.9 cm to 4.3 cm and soil texture ranges from sandy loam to clay (Table 4.3). Table 5.1 shows that for bare soil cases considered alone, linear correlation coefficient maximizes at 10° and decreases markedly at nadir

TABLE 5.1

Results of Least-Square Linear Regressions Used to Establish the General Interpretation Algorithms for: (1) All Classes, (2) Bare Soil Classes, and (3) Crop Canopy Classes

Target Classes	Sample Size	Incidence Angle, °	Regression Coefficients		Linear Correlation Coefficient
			Intercept, dB	Slope dB/1.0% M_{FC}	
All Classes Combined	268	0	- 9.67	0.162	.651
	324	10	-14.34	0.133	.883
	324	20	-14.80	0.078	.653
	268	30	-16.01	0.068	.505
All Bare Soil Classes	124	0	-10.92	0.170	.486
	181	10	-15.96	0.148	.849
	181	20	-17.86	0.114	.700
	124	30	-20.61	0.121	.588
All Vegetation Canopy Classes	144	0	- 9.38	0.165	.855
	143	10	-13.84	0.133	.921
	143	20	-13.03	0.048	.590
	144	30	-14.33	0.047	.525

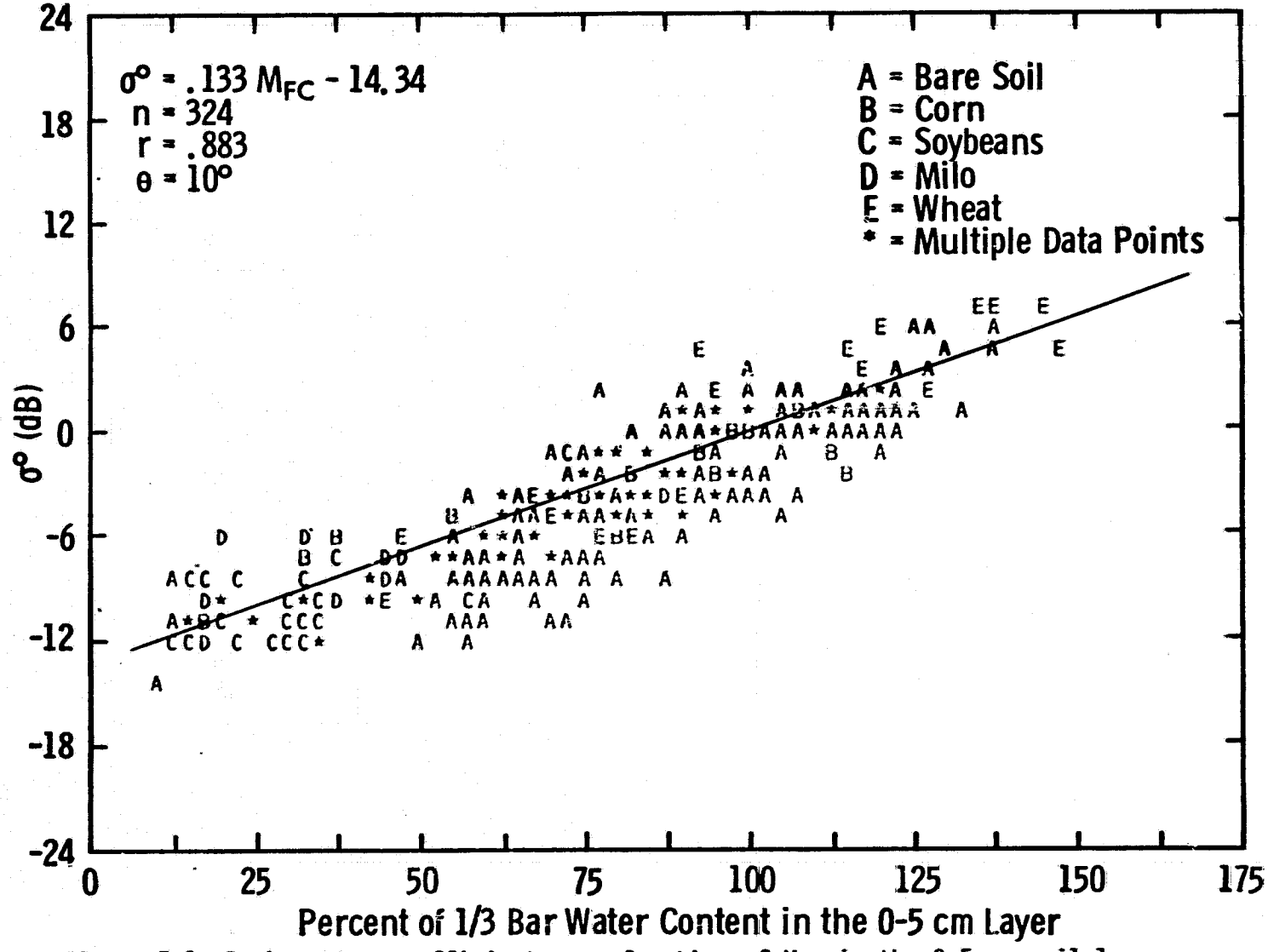

Figure 5.1 Backscatter coefficient as a function of M_{FC} in the 0-5 cm soil layer for 324 observations of bare and vegetated soils at 4.5 GHz, HH polarization, and 10° incidence angle.

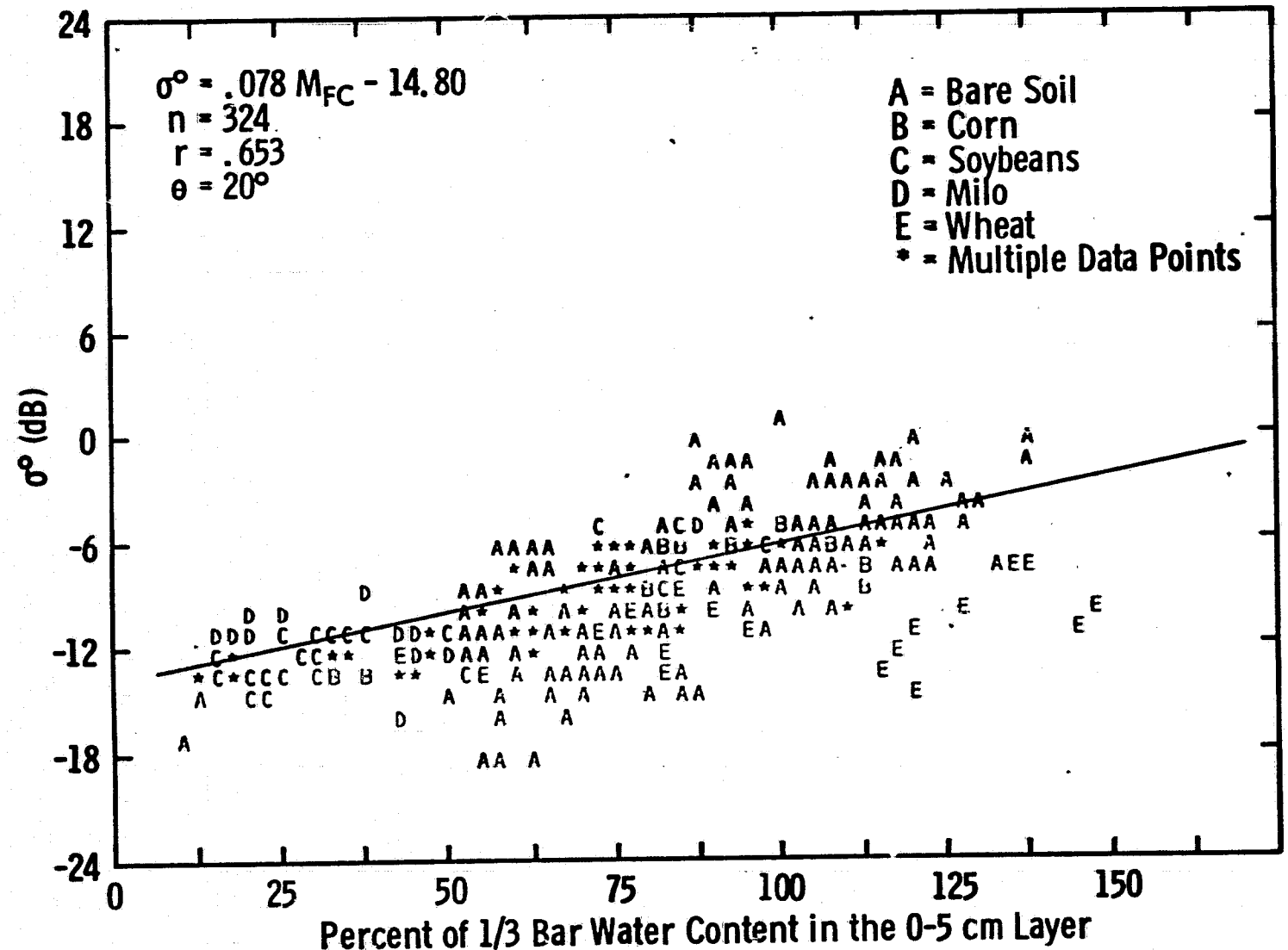

Figure 5.2 Backscattering coefficient as a function of M_{FC} in the 0-5 cm soil layer for 324 observations of bare and vegetated soils at 4.5 GHz, HH polarization and 20° angle of incidence.

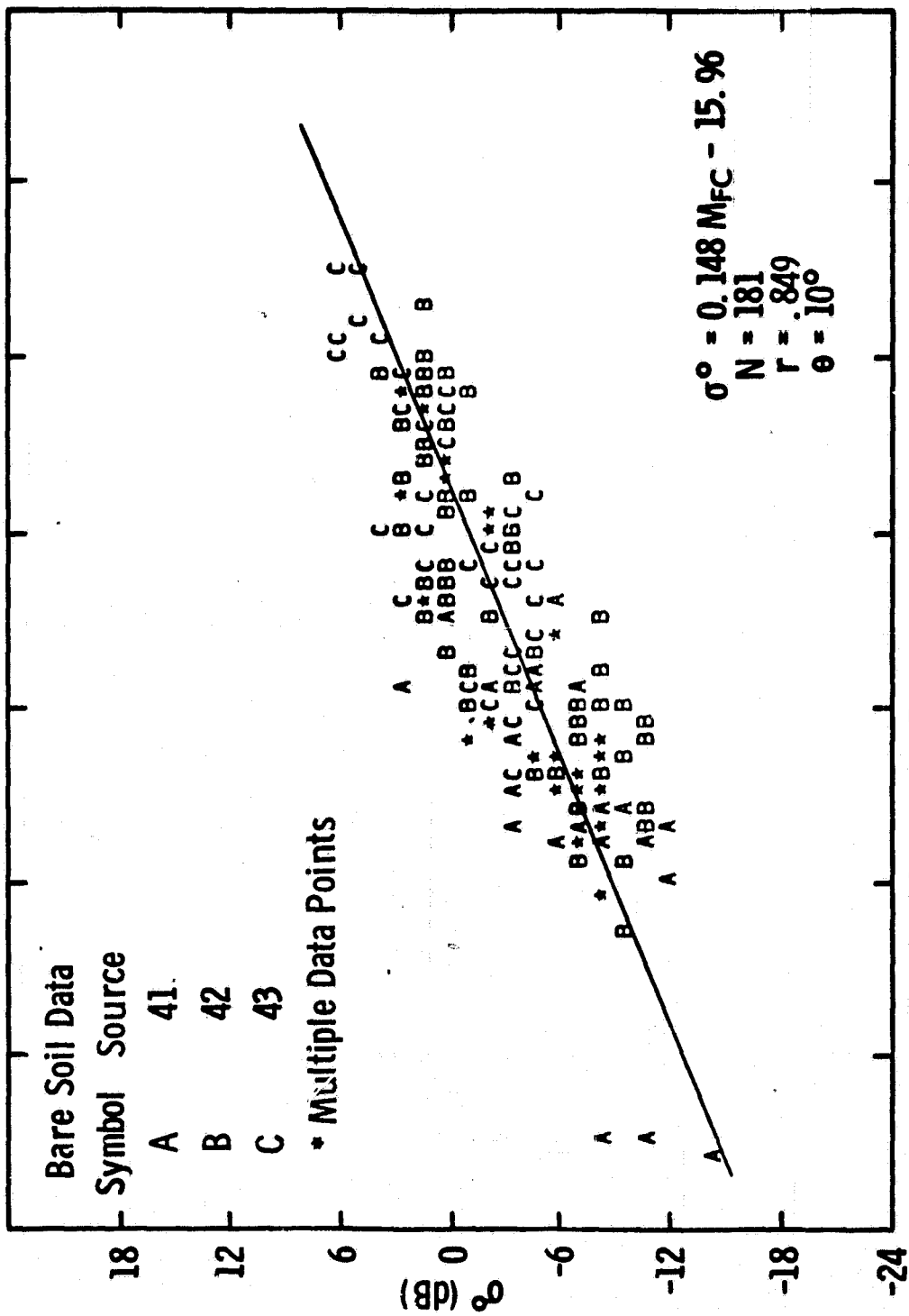

Figure 5.3 Backscattering coefficient as a function of M_{FC} in the 0-5 cm soil layer for 181 observations of bare soil at 4.5 GHz, HH polarization, and 10° angle of incidence.

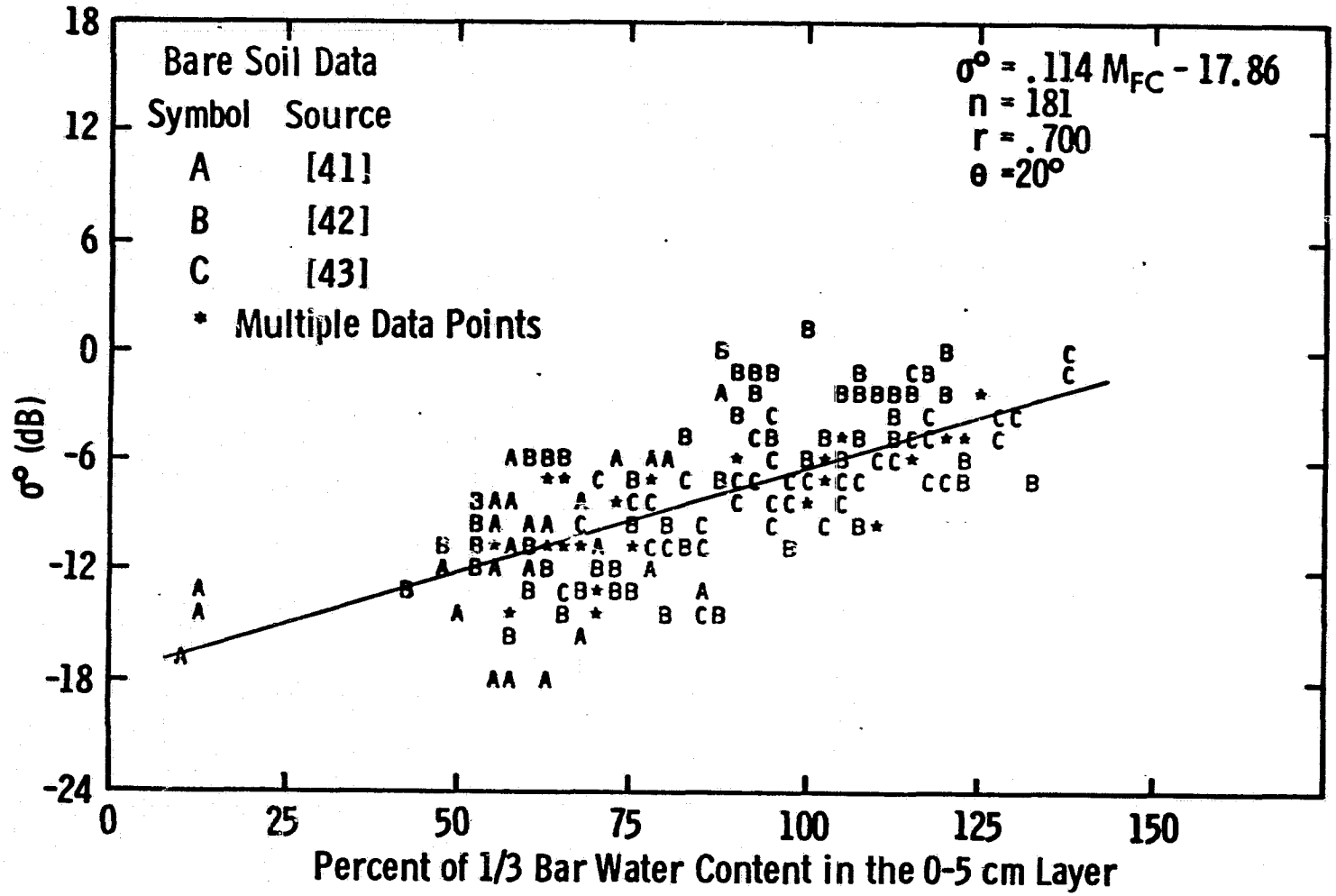

Figure 5.4 Backscattering coefficient as a function of M_{FC} in the 0-5 cm soil layer for 181 observations of bare soil at 4.5 GHz, HH polarization, and 20° angle of incidence.

and as incidence angle approaches 30°. This behavior is caused by the effects of surface roughness near nadir and at high incidence angles. Assuming normal distributions, the 90% confidence interval for the bare soil data plotted in Figures 5.3 and 5.4 gives:

$\hat{M}_{FC}$	90% Confidence Interval dB	
	10°	20°
25	+/- .74	+/- .94
75	+/- .31	+/- .39
100	+/- .33	+/- .42
150	+/- .78	+/-1.0

Scatterplots of 143 data points from fields of corn, soybean, milo, and wheat are shown in Figures 5.5 and 5.6 for 10° and 20°, respectively. For each crop these data cover the full range of crop growth stages and also represent different soil textures and roughness conditions (Table 4.3). The linear correlation coefficient decreases from 0.92 at 10° to 0.59 at 20° because of increasing interclass variance at higher angles due to surface roughness and canopy attenuation differences and also because of higher intraclass variance within the cases of wheat and milo. Ninety percent confidence intervals for crop canopy data alone in Figures 5.5 and 5.6 are similar to those given above as computed for bare soil at 10° and 20°.

For each of the three sets of agricultural scene classes (all classes, bare soil only, crop canopy only), the linear regression coefficients

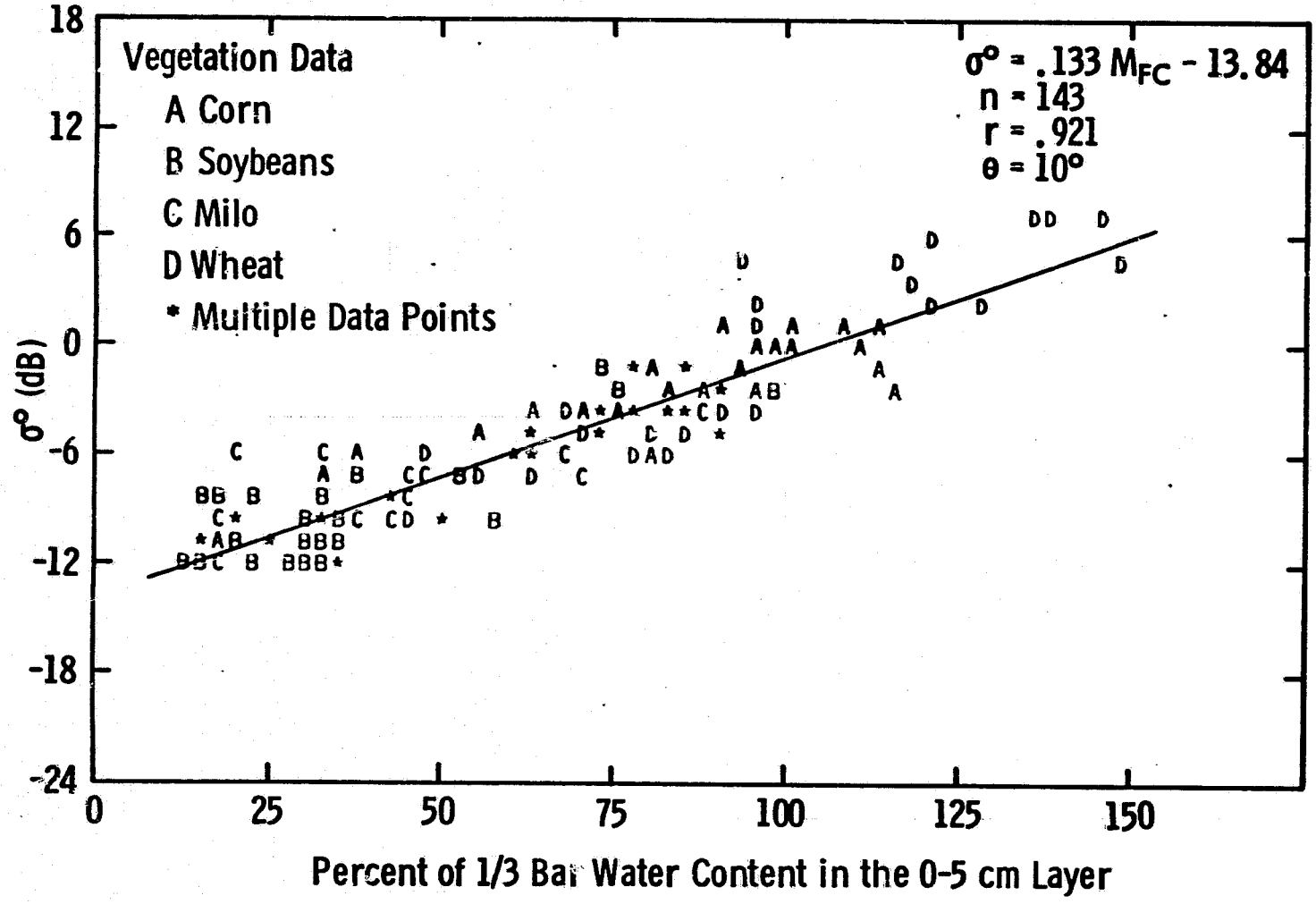

Figure 5.5 Backscattering coefficient as a function of M_{FC} in the 0-5 cm layer for 143 observations of various crops at 4.5 GHz, HH polarization, and 10° angle of incidence.

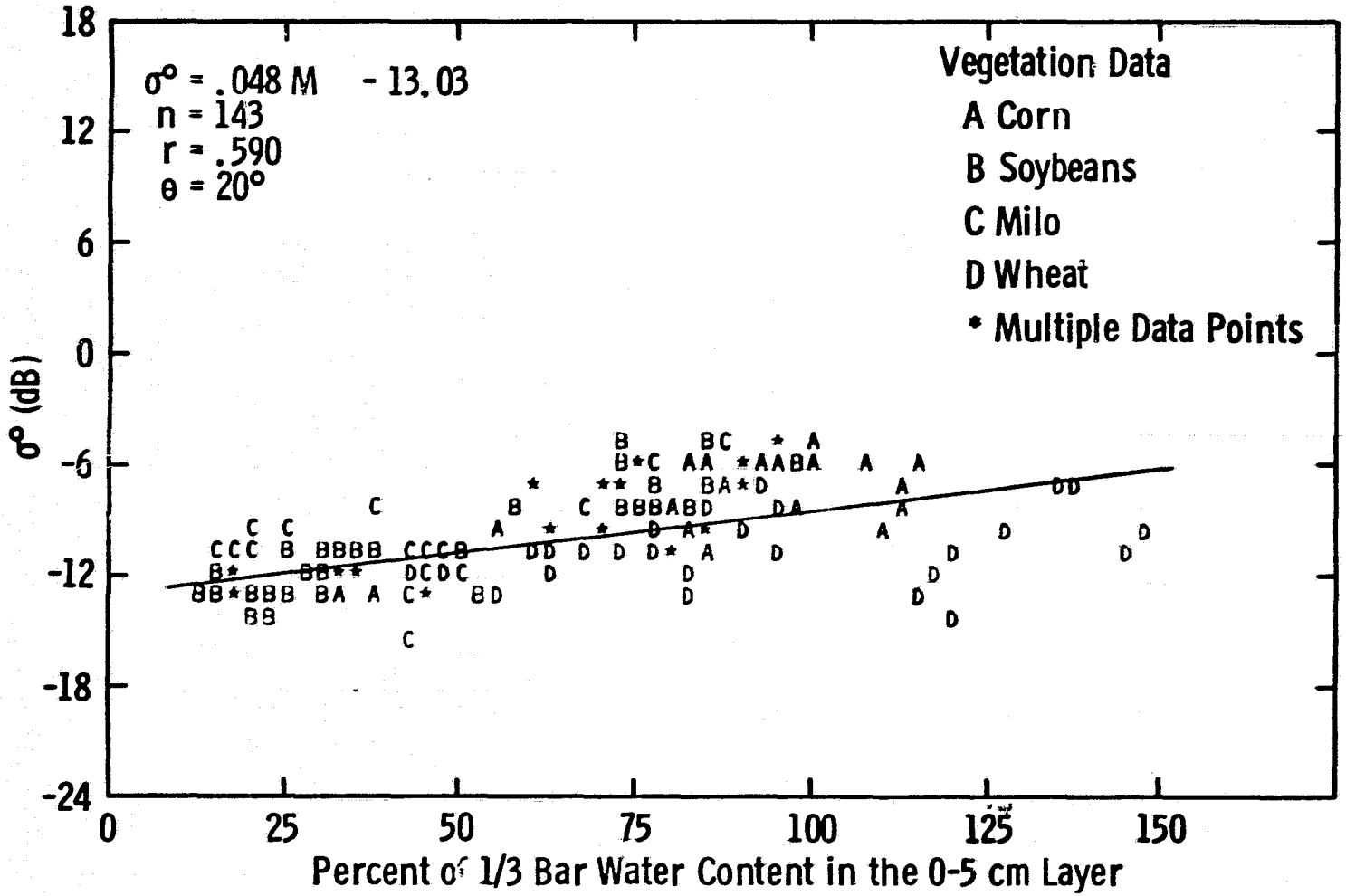

Figure 5.6 Backscattering coefficient as a function of M_{FC} in the 0-5 cm layer for 143 observations of various crops at 4.5 GHz, HH polarization, and 20° angle of incidence.

given in Table 5.1 were fitted with a third-order polynomial function of incidence angle. Thus, intercept and slope for each general scene class are expressed in terms of $f(\theta)$ and $g(\theta)$ respectively as given in Table 5.2 and shown in Figures 5.7 and 5.8. These general equations of the form:

$$\sigma^o = f(\theta) + g(\theta)M_{FC} \tag{5.1}$$

are then inverted to estimate M_{FC} as a function of simulated σ^o.

$$\hat{M}_{FC} = (\sigma^o - f(\theta))/g(\theta) \tag{5.2}$$

Thus, for the general case where all agricultural scene data is considered simultaneously,

$$A(\theta) = (\sigma^o + 9.67 + 0.84\theta - 4.59 \times 10^{-2}\theta^2 + 8.27 \times 10^{-4}\theta^3)/$$
$$(0.161 + 9.38 \times 10^{-4}\theta - 4.97 \times 10^{-4}\theta^2 + 1.21 \times$$
$$10^{-5}\theta^3) \tag{5.3}$$

where

$A(\theta)$ = estimated moisture $\hat{M}_{FC}$ as a function of incidence angle θ relative to the satellite radar.

$A(\theta)$ is used to estimate M_{FC} from simulated satellite radar data in the case where no ancillary data is available and also in the case where the locations of roads, buildings, and water bodies are assumed to be known.

In the case where ancillary data allows differential treatment of agricultural scene data into that from crop canopies and that from bare soil surfaces, moisture is estimated from $B(\theta)$ and $C(\theta)$, respectively.

TABLE 5.2

Third-Order Polynomial Fits of Linear Regression Coefficients As a Function of Incidence Angle Between 0° and 30° for (a) All Agricultural Scene Data, (b) Bare Soil Data Only, and (c) Crop Canopy Data Only

$$\sigma^o = f(\theta) + g(\theta)\, M_{FC}$$

Agricultural Scene Classes	$f(\theta)$, intercept in dB	$g(\theta)$, slope in dB/1.0% M_{FC}
All agricultural scene data	$-9.666-8.432\times10^{-1}\theta+4.587\times10^{-2}\theta^2-8.272\times10^{-4}\theta^3$	$.1615+9.383\times10^{-4}\theta-4.975\times10^{-4}\theta^2+1.207\times10^{-5}\theta^3$
Bare soil data only	$-10.92-8.366\times10^{-1}\theta+4.0635\times10^{-2}\theta^2-7.838\times10^{-4}\theta^3$	$.1697+6.017\times10^{-4}\theta-3.755\times10^{-4}\theta^2+1.003\times10^{-5}\theta^3$
Crop canopy data only	$-9.377-9.572\times10^{-1}\theta+6.339\times10^{-2}\theta^2-1.233\times10^{-3}\theta^3$	$.1653+5.997\times10^{-3}\theta-9.47\times10^{-4}\theta^2+2.273\times10^{-5}\theta^3$

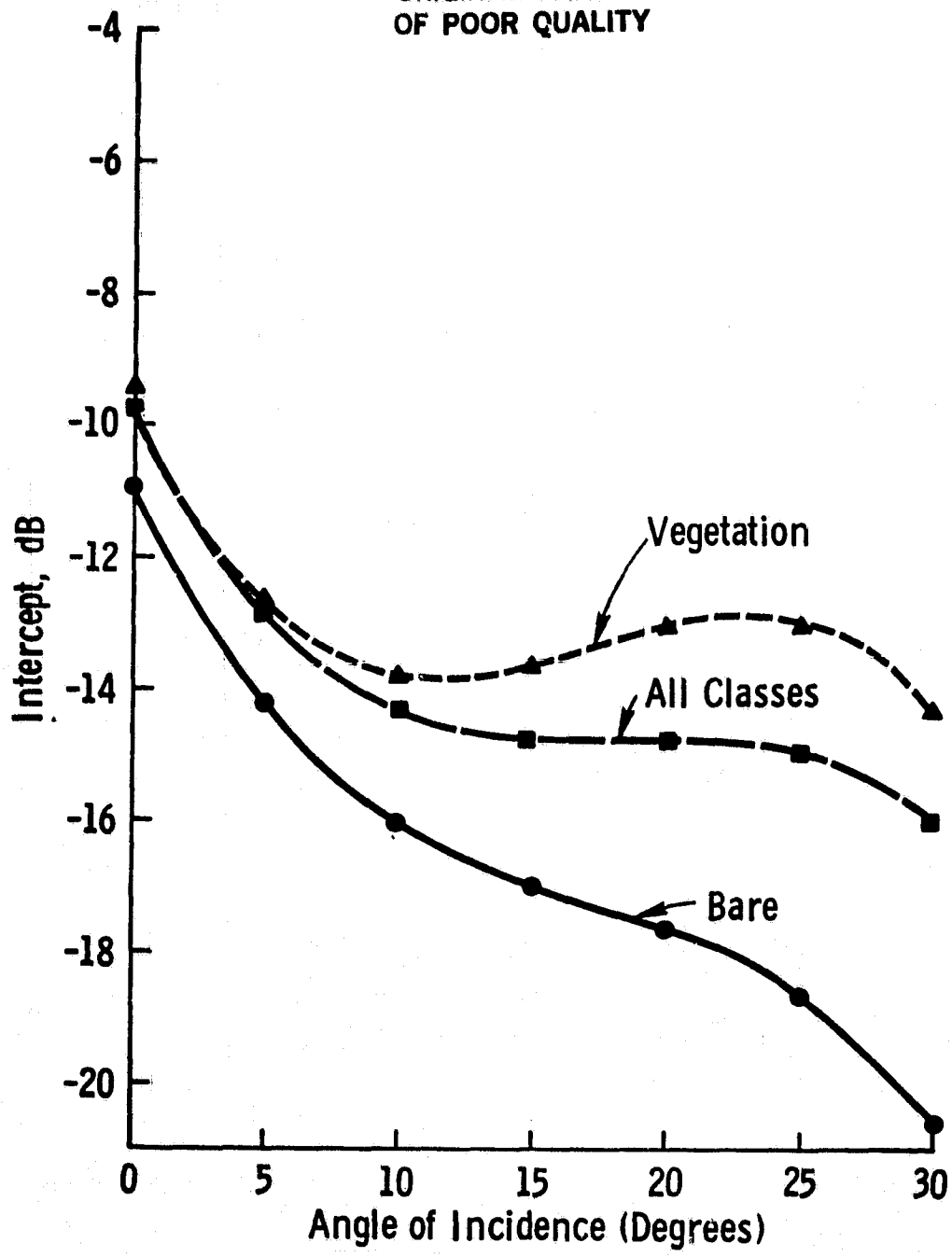

Figure 5.7 Intercept of generalized algorithms as a function of angle of incidence between 0° and 30°. $f(\theta)$ is shown for (a) all agricultural scene data combined, (b) bare soil data only, and (c) crop canopy data only.

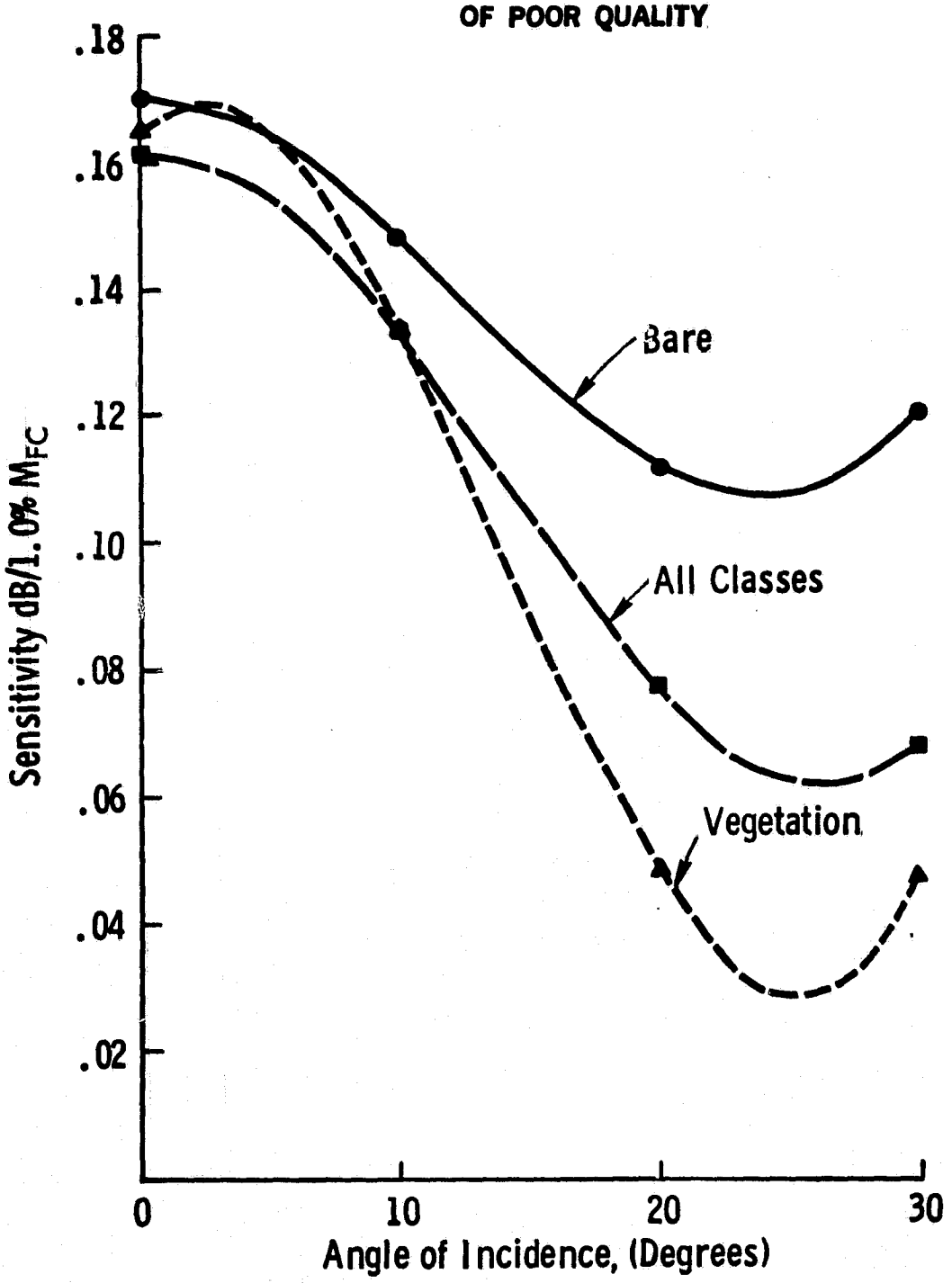

Figure 5.8 Slope of generalized algorithms as a function of angle of incidence between 0° and 30°. $g(\theta)$ is shown for (a) all agricultural scene data combined, (b) bare soil data only, and (c) crop canopy data only.

$$B(\theta) = (\sigma^{o} + 10.92 + 8.37 \times 10^{-1}\theta - 4.06 \times 10^{-2}\theta^{2} + 7.84 \times 10^{-4}\theta^{3})/(0.17 + 6.02 \times 10^{-4}\theta - 3.76 \times 10^{-4}\theta^{2} + 1.00 \times 10^{-5}\theta^{3}) \quad (5.4)$$

$$C(\theta) = (\sigma^{o} + 9.38 + 9.57 \times 10^{-1}\theta - 6.34 \times 10^{-2}\theta^{2} + 1.23 \times 10^{-3}\theta^{3})/(0.165 + 4.0 \times 10^{-3}\theta - 9.47 \times 10^{-4}\theta^{2} + 2.27 \times 10^{-5}\theta^{3}) \quad (5.5)$$

where

$B(\theta)$ = estimated moisture $\hat{M}_{FC}$ in the 0-5 cm layer of bare soil

$C(\theta)$ = estimated moisture $\hat{M}_{FC}$ in the 0-5 cm layer beneath crop canopies.

No attempt is made to account for the effects of crop type or row direction effects in $C(\theta)$.

5.2 Interpretation of Simulated Radar Images

The general interpretation procedure is outlined in Figure 5.9. For a given radar simulation (angle swath, resolution, and moisture condition) the range information associated with each σ^{o} value is used to calculate an effective incidence angle θ relative to the radar. This computation assumes spherical earth geometry, constant orbital altitude relative to mean sea level, and a constant mean elevation of the data base. Estimated soil moisture in the 0-5 cm layer $\hat{M}_{FC}$ was

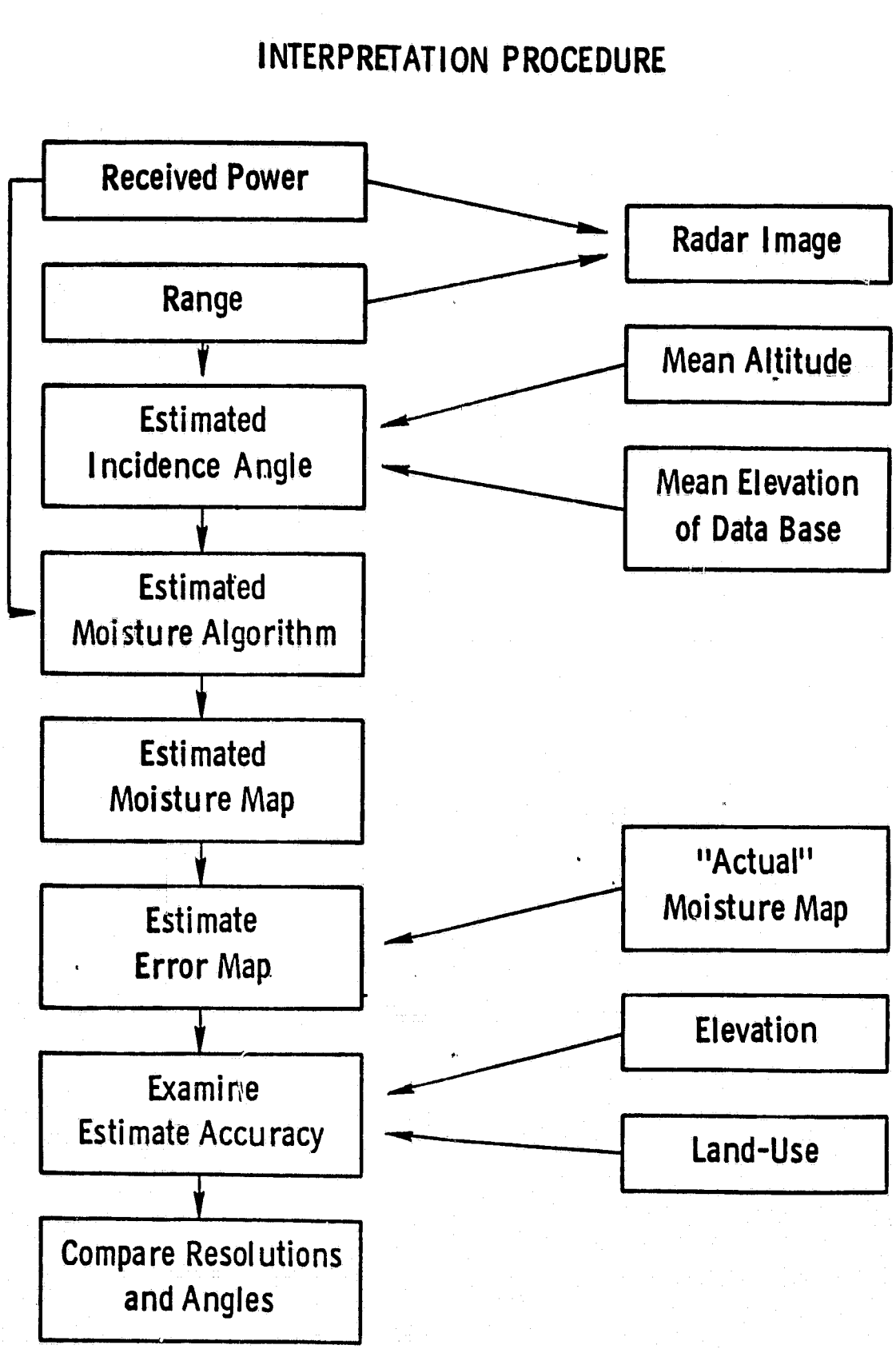

Figure 5.9 General interpretation procedure for evaluating soil moisture estimate accuracy.

calculated from the general interpretation algorithm (Equation 5.3) given σ° and θ for each simulated radar image pixel element. Estimated moisture images were produced for each simulation by converting $\hat{M}_{FC}$ to graytone level by:

$$G_M = 3/2\ \hat{M}_{FC} + 16 \qquad (5.6)$$

where

G_M = graytone level between 0 and 255.

Equation 5.6 also describes the scaling used to produce the "actual" moisture images in Section 4.5.

Examples of estimated moisture images at the 7.5° to 9.3° angular range and for each resolution and moisture condition are shown in Figures 5.10 to 5.15. All images have equivalent hue, intensity, and saturation scaling. The estimated soil moisture M_{FC} is shown in Figures 5.10 to 5.15 as derived from Equation 5.3 assumes no natural limits on estimated moisture, whereas real-world conditions limit "actual" soil moisture to $0\% \leq M_{FC} \leq 150\%$. In addition, Equation 5.3 represents a blind moisture classifier since it requires no *a priori* knowledge of local slope, land-use category, crop canopy, crop row orientation, or surface roughness.

5.3 Evaluation of Moisture Estimate Accuracy Using Blind Classifier

Precise evaluation of soil moisture estimate accuracy was complicated by the geometric relief displacements inherent in the radar imaging process. While the relatively small vertical relief and slope of the data base produced insignificant layover and shadowing in the resultant images,

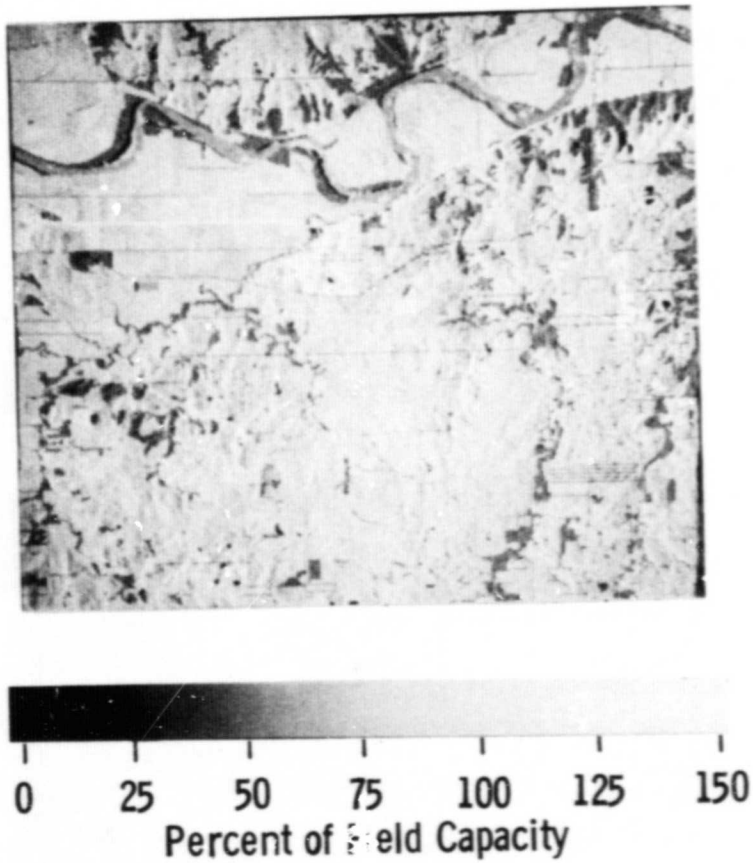

Figure 5.10 Predicted moisture map estimated by general algorithm from radar simulation with 20-meter resolution and 7.5° angle of incidence for Moisture Condition 1.

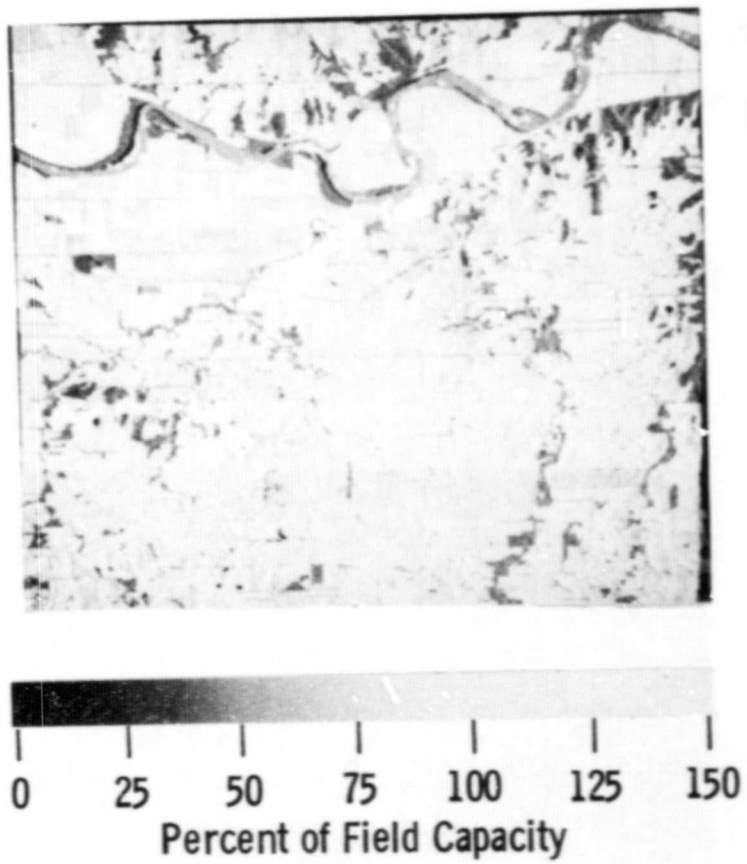

Figure 5.11 Predicted moisture map estimated by general algorithm from radar simulation with 20-meter resolution and 7.5° angle of incidence for Moisture

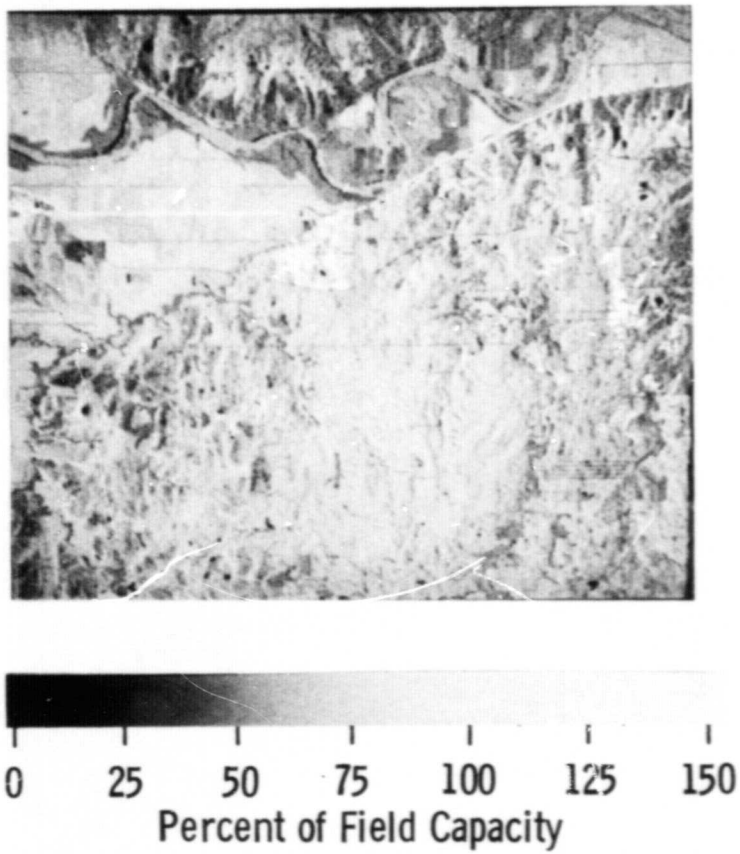

Figure 5.12 Predicted moisture map estimated by general algorithm from radar simulation with 20-meter resolution and 7.5° angle of incidence for Moisture Condition 3.

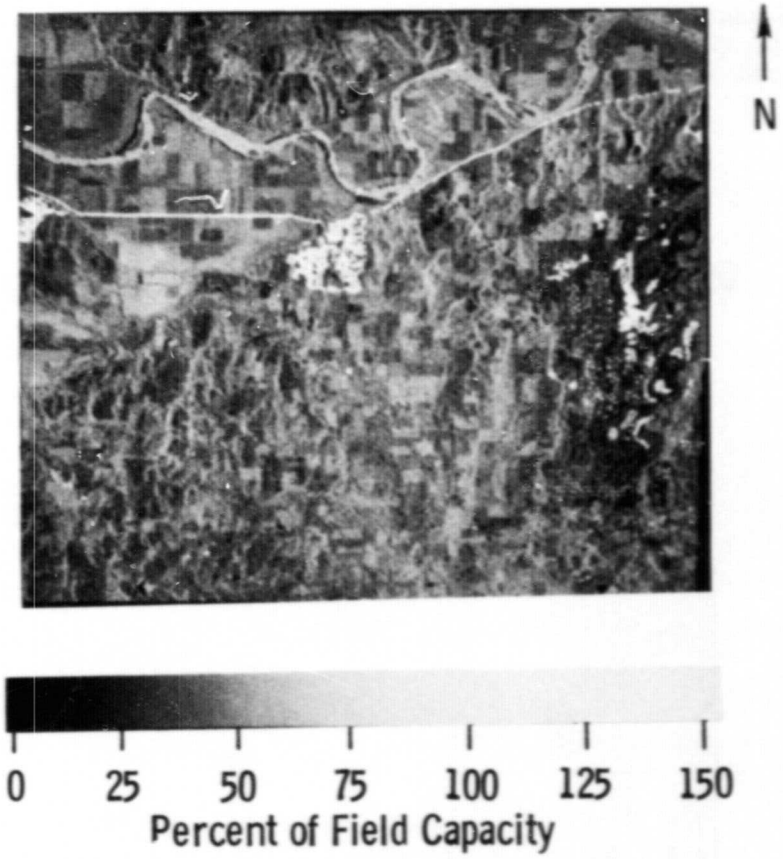

Figure 5.13 Predicted moisture map estimated by general algorithm from radar simulation with 20-meter resolution and 7.5° angle of incidence for Moisture Condition 4.

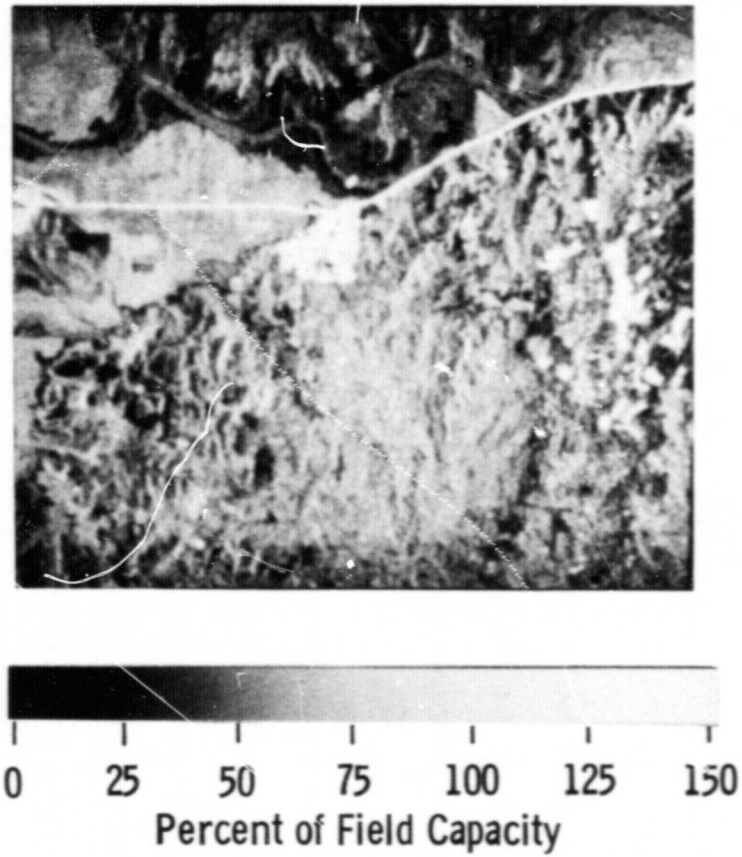

Figure 5.14 Predicted moisture map estimated by general algorithm from radar simulation with 100-meter resolution and 7.5° angle of incidence for Moisture Condition 3.

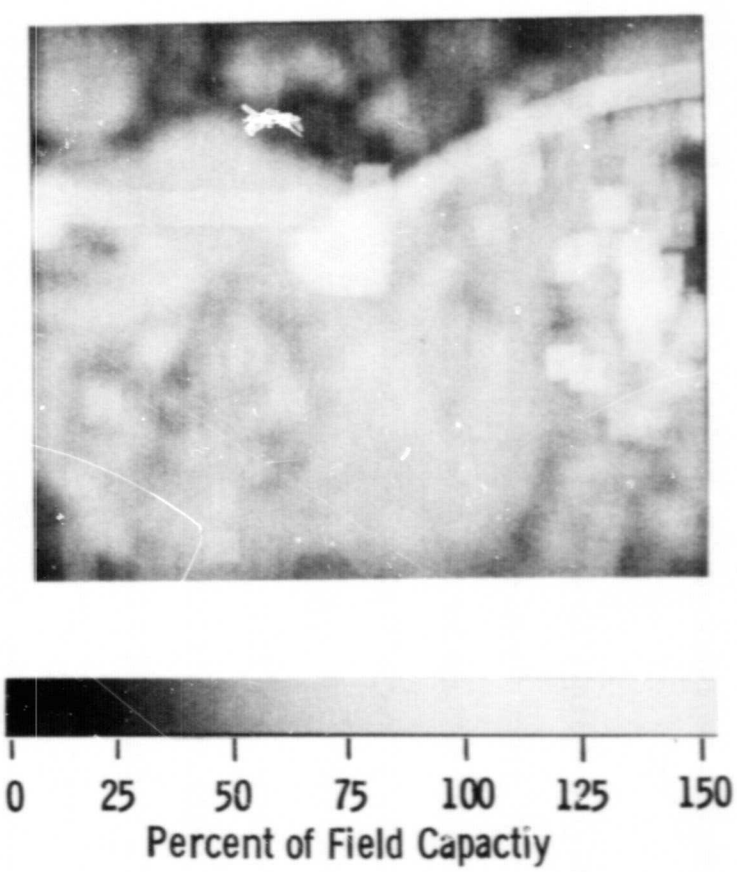

Figure 5.15 Predicted moisture map estimated by general algorithm from radar simulation with 1-kilometer resolution and 7.5° angle of incidence for Moisture Condition 3.

foreshortening produced a geometric displacement of upland surfaces by as much as 100 meters relative to the surface defined by the river floodplain.

Quantitative evaluation of moisure estimate accuracy by machine assumes that the radar image can be accurately mapped back into the coordinate system defined by the original data base. Because of the complexity of image rectification to account for range creep caused by foreshortening in the radar images a dual appraoch was followed to establish estimate accuracy. In the first and "worst-case" approach, moisture estimate error is examined for the entire data base and is subject to errors associated with imaging geometry problems and the effects of unknown local slope. In the second approach, moisture estimate accuracy will be considered only for the relatively flat region defined by the river floodplain where elevation of the data base is less than or equal to 820 feet. Both analytic approaches utilized a common set of moisture estimate error maps.

Estimate error maps were produced by the following procedure. A set of five control points were identified on the simulated radar imagery for recognizable features on the floodplain. These same features were located on the data base. The mean distance between the control points as identified on the radar imagery and those on the data base was used to translate the coordinate system of the estimated moisture image without rotation or warping. The resultant estimated moisture matrix was then compared to the "actual" moisture matrix from the data base with a mean registration error of +/- 20 meters on the floodplain and +/- 100 meters on the upland surfaces due to uncorrected range creep. Thus for a given

resolution and moisture condition, the estimated $\hat{M}_{FC}$ and "actual" M_{FC} could be compared on a pixel by pixel basis relative to the 18 x 18 meter resolution cells of the data base.

Figures 5.16 to 5.19 show the difference between estimated and actual moisture for each resolution and moisture condition.

$$G_{E_{ij}} = \hat{M}_{FC_{ij}} - M_{FC_{ij}} + 128 \qquad (5.7)$$

where

G_E = image graytone level between 0 and 255

$\hat{M}_{FC}$ = estimated percent of field capacity in the 0-5 cm layer

M_{FC} = "actual" percent of field capacity in the 0-5 cm layer

ij = image position of a given pixel element

Thus, for a given image $G_E = 128$ (medium gray) represents zero difference between estimated and actual moisture, bright pixel elements with $G_E >> 128$ represent a large overestimate of moisture, and dark pixel elements with $G_E << 128$ correspond to large underestimates of "actual" moisture.

For any of the three simulated resolutions, some general observations can be made regarding estimate error as a function of certain data-base characteristics.

1. Pixels with Zero Moisture in the Data Base. By definition, all target classes in the data base for which "actual" moisture is undefined and arbitrarily set to zero will result in large moisture estimate errors. Bridges, buildings, and railroads with a constant mean σ^o of 10.0 will always produce a moisture estimate >> zero. For

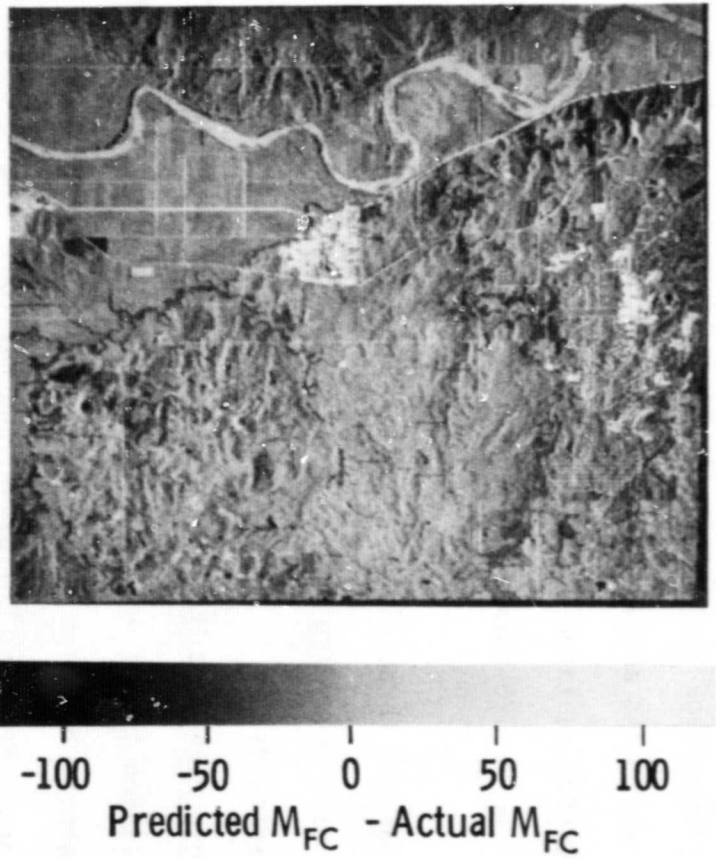

Figure 5.16 Soil moisture estimate error, predicted M_{FC} minus input M_{FC}, from radar simulation with 20-meter resolution and 7.5° angle of incidence for Moisture Condition 3.

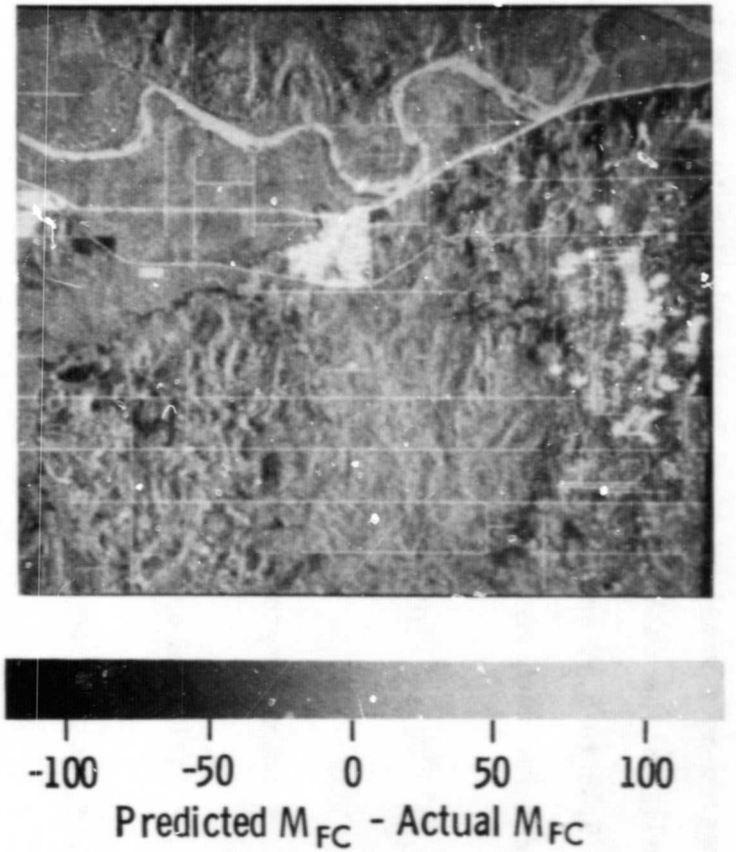

Figure 5.17 Soil moisture estimate error, predicted M_{FC} minus input M_{FC}, from radar simulation with 100-meter resolution and 7.5° angle of incidence for Moisture Condition 3.

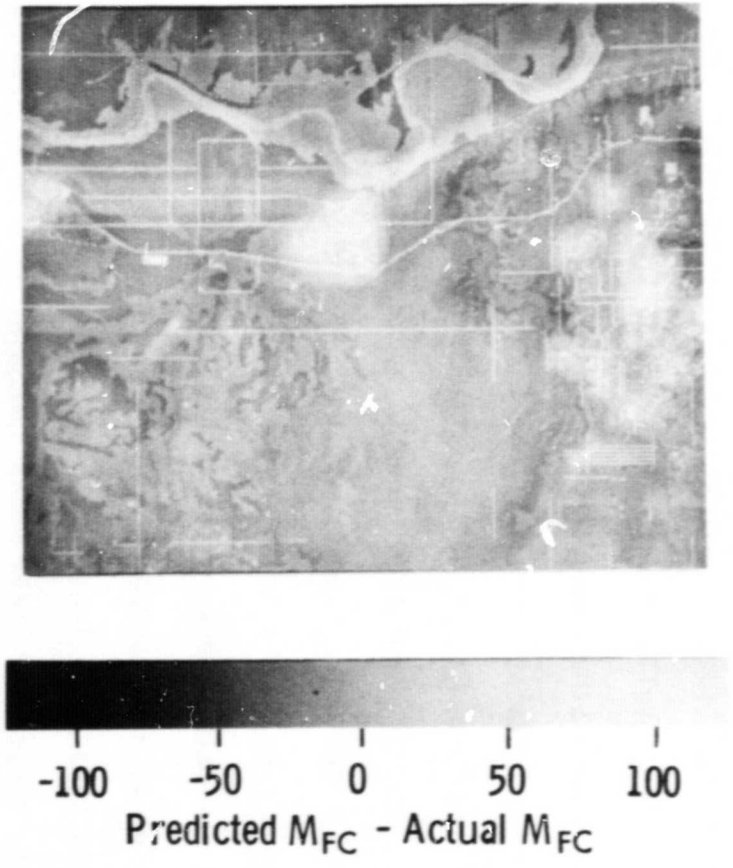

Figure 5.18 Soil moisture estimate error, predicted M_{FC} minus input M_{FC}, from radar simulation with 1-kilometer resolution and 7.5° angle of incidence for Moisture Condition 3.

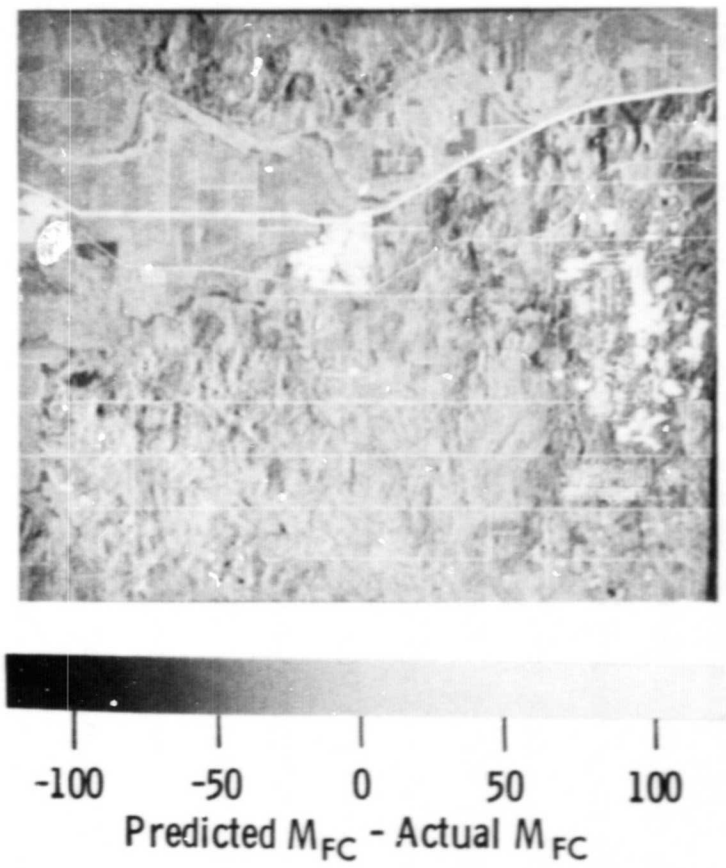

Figure 5.19 Soil moisture estimate error, predicted M_{FC}, minus input M_{FC}, from radar simulation with 100-meter resolution and 11.1° angle of incidence for Moisture Condition 3.

water bodies and roads, "actual" moisture is undefined and set equal to zero, while estimated moisture for these target classes is always greater than zero for θ near nadir. Thus, such targets are generally bright on the error maps (Figures 5.16 to 5.19). These targets comprise 7.4% of the data base.

2. Tree Canopies. Tree canopies are assumed to completely attenuate the backscatter contribution from the underlying soil at the simulated frequency. Thus, estimated moisture is generally far less than "actual" moisture except for the very dry conditions simulated for Moisture Condition 4 (30 days after the thunderstorm). Deciduous trees comprise 13.0% of the data base.

3. Local Slope Effects. Since Equation 5.3 is a blind classifier of the radar image, a predictable error component is introduced into the error maps because of the high sensitivity of σ^o to θ_ℓ near nadir.

In general, moisture is overestimated for west-facing local slopes (those toward the satellite) while moisture is underestimated for east-facing local slopes (those away from the satellite). As would be expected, these effects are most noticeable for the dissected upland areas to the north and south of the river floodplain and for 20-meter resolution. Coarser resolution tends to average many of these errors associated with the effects of local slope.

4. Range Creep. The translation of features on the radar imagery relative to the data base as a function of elevation by foreshortening produces a double error component on the error maps. Since radar image to data base rectification was performed to minimize position errors on the floodplain, this error component is most noticeable in the dissected upland region in the lower right side of the error maps.

Moisture estimate errors in this region resemble "ghost images," especially for linear features such as roads. The "ghost" errors are approximately equal in magnitude but opposite in sign and are separated by one to five pixel elements. These double estimate errors are artifacts of the comparison methodology and relate to the position of a feature such as a road on the data base and its offset location on the interpreted radar imagery.

Figures 5.20 to 5.22 are the result of color slicing the graytone scale on the error maps shown in Figures 5.16 to 5.18 at the levels given in Table 5.3. The error map pixels encoded in yellow correspond to an estimate error of +/- 20% of the "actual" input percent of 1/3-bar water content. This level of error in percent of field capacity represents an equivalent uncertainty in gravimetric moisture of +/- 1.8%, +/- 4.2%, and +/- 5.1% for loamy sand, loam, and clay loam respectively from Table 5.3.

The moisture estimate accuracy as presented in Figures 5.20 to 5.23 can also be related to initial estimates of accuracy level required by agronomists and hydrologists. Tables 5.4 and 5.5 present the accuracy requirements identified for the soil moisture information user community [51]. The approximate relationship between accuracy levels in Tables 5.4 and 5.5 and estimate error in percent of field capacity is given in Table 5.6.

5.4 Analysis of Moisture Estimate Accuracy Over the Total Data Base

The relationships between absolute estimate error and cumulative percent of the 800,000 pixels in the total base are presented in

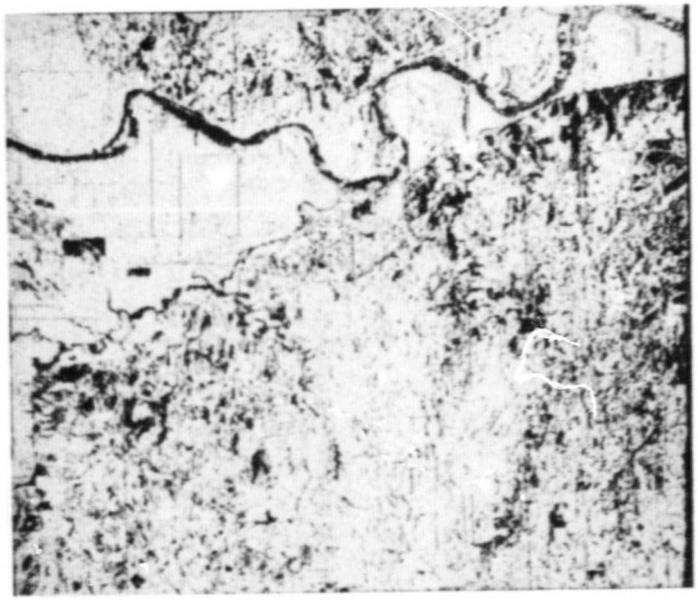

Figure 5.20 Soil moisture estimate error level-sliced at accuracy levels 3 and 4 from radar simulation with 20-meter resolution and 7.5° angle of incidence for Moisture Condition 3.

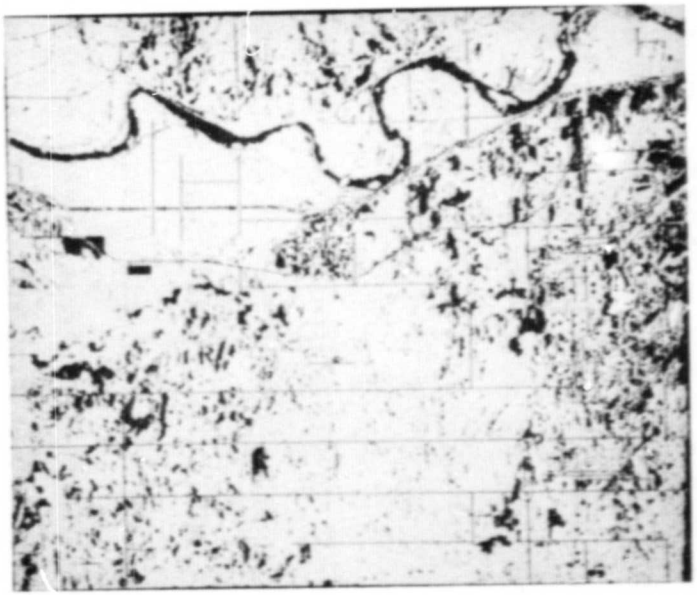

Figure 5.21 Soil moisture estimate error level-sliced at accuracy levels 3 and 4 from radar simulation with 100-meter resolution and 7.5° angle of incidence for Moisture Condition 3.

N

ORIGINAL PAGE
BLACK AND WHITE PHOTOGRAPH

Figure 5.22 Soil moisture estimate error level-sliced at accuracy levels 3 and 4 from radar simulation with 1-kilometer resolution and 7.5° angle of incidence for Moisture Condition 3.

TABLE 5.3

Interpretation of Soil Moisture Estimate Error Maps

$$E = \hat{M}_{FC} - M_{FC}$$

where E = error in % of 1/3-bar water content

$\hat{M}_{FC}$ = % of 1/3-bar water content as estimated from radar image using Equation 5.3

M_{FC} = "actual" % of 1/3-bar water content from Equation 4.21

A. Error Map Color Codes

Color	E, percent	
	E max	E min
Blue	- ∞	- 30
Green	- 30	- 20
Yellow	- 20	+ 20
Orange	+ 20	+ 30
Red	+ 30	+ ∞

B. Relationship of E to Uncertainty in Gravimetric Moisture Content

|E|	Gravimetric Moisture		
	loamy sand	loam	clay loam
30%	+/- 2.69%	+/- 6.33%	+/- 7.63%
20%	+/- 1.80%	+/- 4.22%	+/- 5.09%
10%	+/- 0.90%	+/- 2.11%	+/- 2.54%

TABLE 5.4

Soil Moisture Information and Data Requirements
at Different Crop Production Stages (from [51])

Crop Production Stage	Accuracy Level*	Frequency (Days)	Resolution (km^2)	Depth
Planning (Acreage & Yield Predictions)	3-5	7-20	1-15	profile
Ground Preparation & Planting	1-3	5	.5-1	surface layer
Germination	3	5	1-10	surface layer
Growth & Development				
Nutrient Supply	3	7-10	1-10	profile
Water Management-Irrigation	5	3	.5	profile
Water Management-Drainage	3	3-5	1-10	profile
Pest Management	5	3	.5	surface layer
Maturing-Yield Estimate	3-5	3-10	.5-1	profile
Harvest	3	3-7	.5	surface layer

* 1 = General accuracy of High, Medium, or Low
2-4 = Gradation between Accuracy Levels 1 and 5
5 = +/- 4% accuracy by value measurement

TABLE 5.5

Soil Moisture Information and Data Requirements in Hydrology (from [51])

Soil Moisture Applications and Identified Users	Accuracy Level*	Frequency (Days)	Resolution (km^2)
Runoff Potential:			
Federal Users: NOAA-NWS, USACE, SCS Design Engineers WPRS, HUD Flood Insurance Program	1**	3-7	5-25
State Users: Highway Departments & Water Resource Centers			
County and City Governments			
Private Power Companies			
Erosion Losses:			
Federal Users: Design Departments of USACE, USDI, and USDA-SCS	3	3	5-25
County Organizations of Governments	5	3	.5
Farmers' Organizations	3	3	1
Reservoir Management:			
Federal Users: USACE, WPRS	1	3-7	5-25
State and Local Users: Water Resource Centers	3	3-7	.5
Private Power Companies, Regional Planners, Recreation Industries	3	3-7	.5
Infiltration for Trafficability and Structure Design			
Federal Users: USACE, USDA-SCS	5	3	.5
State Users: Drainage Districts, Planners	5	3	.5
Private Irrigation Design Engineers, Mining Engineers, Developers	5	3	.1
Water Quality			
Pesticide and Nutrient Losses:			
Federal Users: EPA, FDA, USDA-SCS	5	3	.1
State Users: Water Resource Centers	3-5	3	.1-.5
Private Irrigators, Farm Organizations, Feed-Lot Operators, Hydrologic Engineers, Planners & Developers	1-3	3-7	5

*1 = General accuracy of High, Medium, or Low
2-4 = Gradation between Levels 1 and 5
5 = ±2% accuracy by volume measurement
** = Data useful only to the [illegible]

TABLE 5.6

Approximate Relationship Between Uncertainty in Percent of Field Capacity and User Requirements of Moisture Estimate Accuracy

User-Defined Accuracy Level [51]	Uncertainty in % of Field Capacity
1	+/- 50%
2	+/- 40%
3	+/- 30%
4	+/- 20%
5	+/- 10%

Figures 5.23 to 5.26 for Moisture Conditions 1 to 4 respectively for the 7.5° to 9.3° angular swath. Similar plots for the 11.1° to 12.8° angular swath show only slightly lower estimate accuracy for each simulated moisture condition and only Moisture Condition 3 for drying conditions is shown in Figure 5.27. These results represent a "worst case" evaluation of moisture estimation accuracy since no adjustment is made to account for errors caused by geometric registration problems, the effects of local slope, or the inclusion of data base categories where moisture is undefined.

For Moisture Condition 1 where the soil is at 100% of field capacity, a +/- 20% estimate accuracy is achieved (estimated moisture $\hat{M}_{FC}$ ranges between 80% and 120%) over 55.6%, 65.0%, and 86.6% of the data base for resolutions of 20 m, 100 m, and 1 km respectively. This trend toward increasing estimate accuracy at coarser resolutions also is apparent in Table 5.7 and 5.8 for simulation Moisture Conditions 2 and 3 (immediately after the thunderstorm and 10 days later). This result is apparently due to several considerations:

1. From Equations 4.21 to 4.25, "actual" moisture does not vary dramatically between adjacent 18 x 18 meter data base pixels, except at the boundaries of soil types,

2. the coarser resolutions average the local effects of slope, canopy cover type, row direction and surface roughness, and

3. the effects of water bodies, cultural targets, and forested areas are averaged over much larger areas.

For Moisture Condition 4, drought conditions, the lower accuracy of the 1-km resolution compared to the finer resolutions is caused by the effects of cultural targets. Categories such as buildings, bridges,

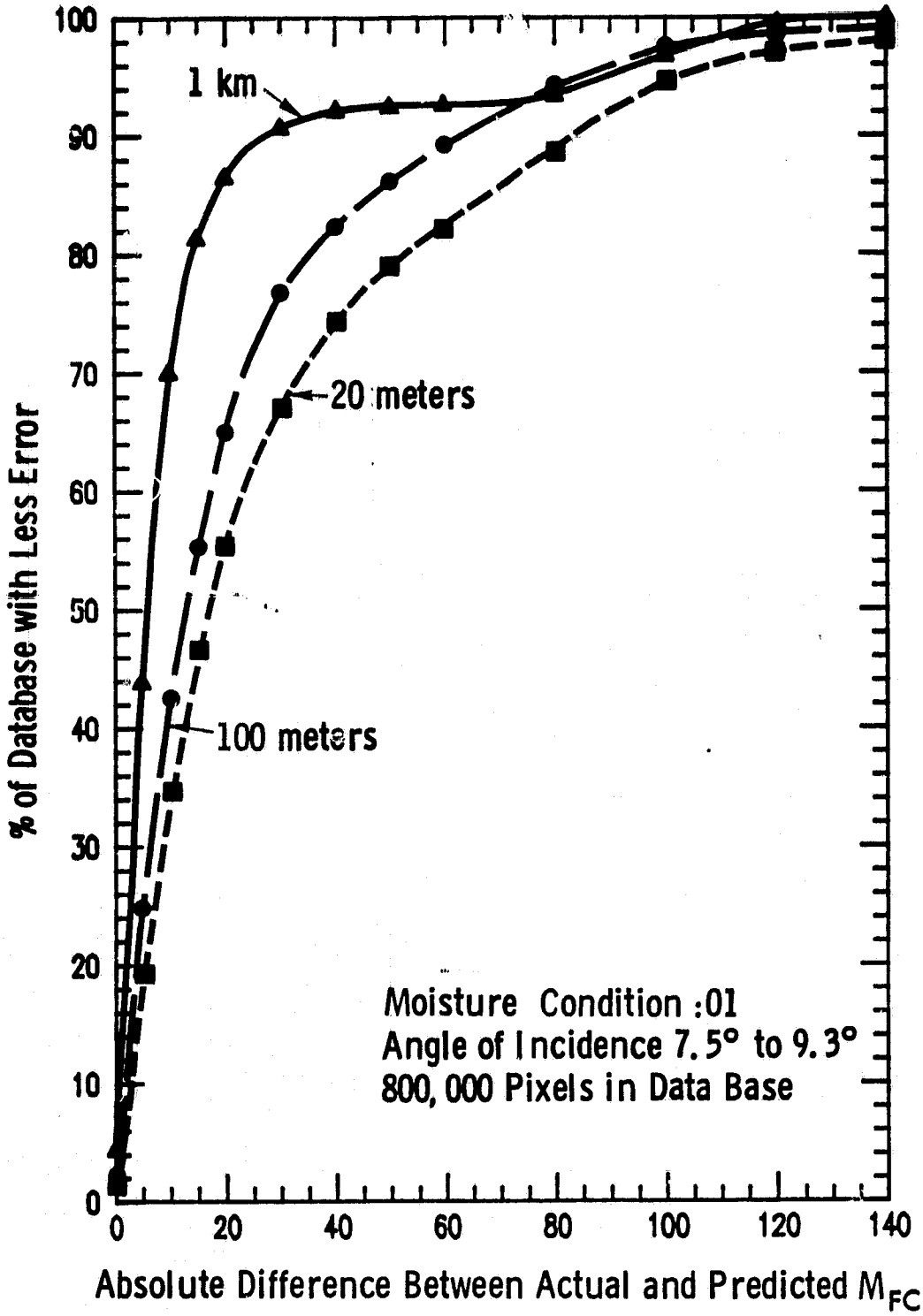

Figure 5.23. Soil Moisture Estimate Accuracy for the Entire Simulation Data Base with Moisture Condition 1, All Soil at Field Capacity, and at Angle of Incidence Between 7.5° and 9.3°.

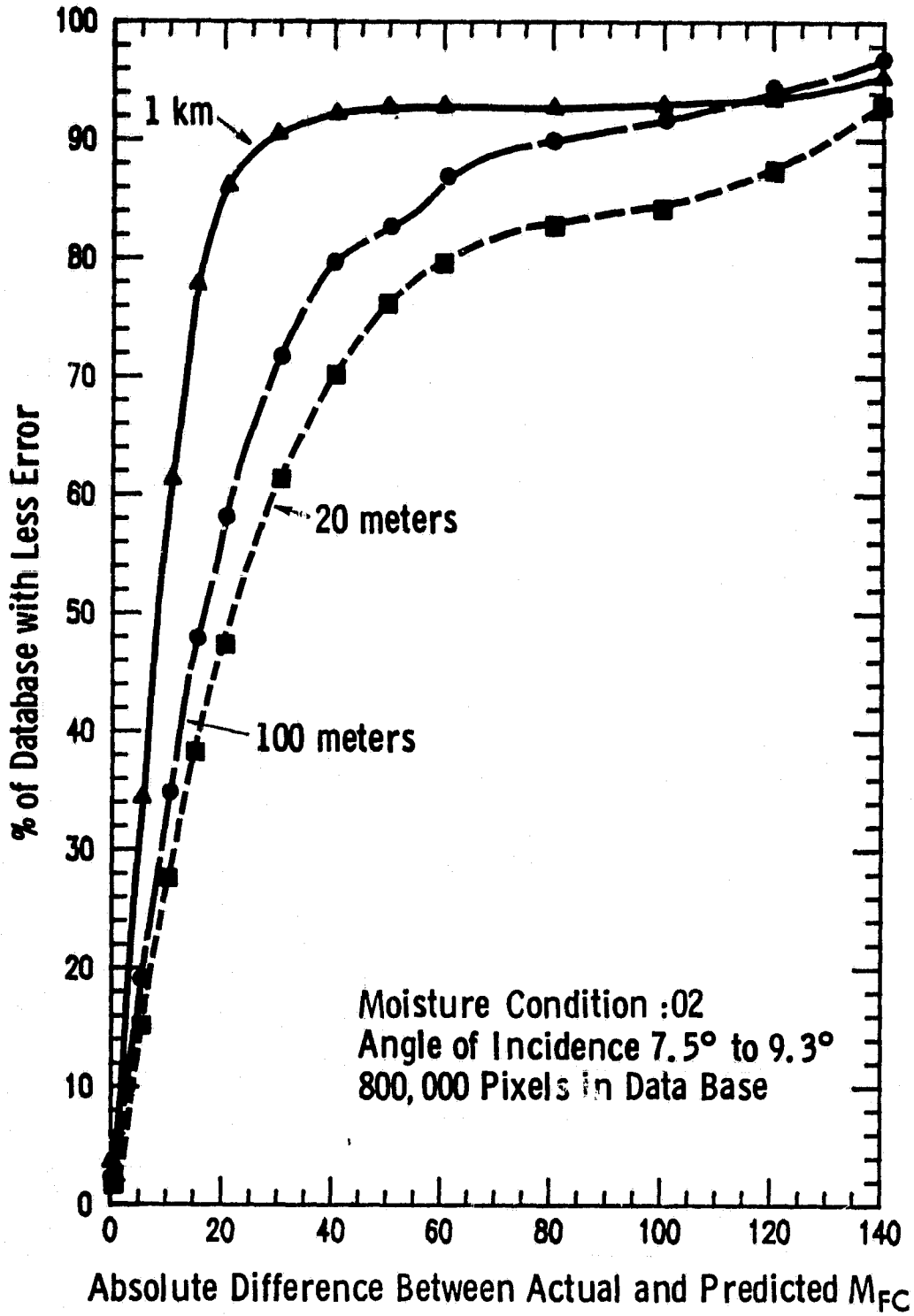

Figure 5.24. Soil Moisture Estimate Accuracy for the Entire Simulation Data Base with Moisture Condition 2, Saturated Soil, and at Angles of Incidence Between 7.5° and 9.3°.

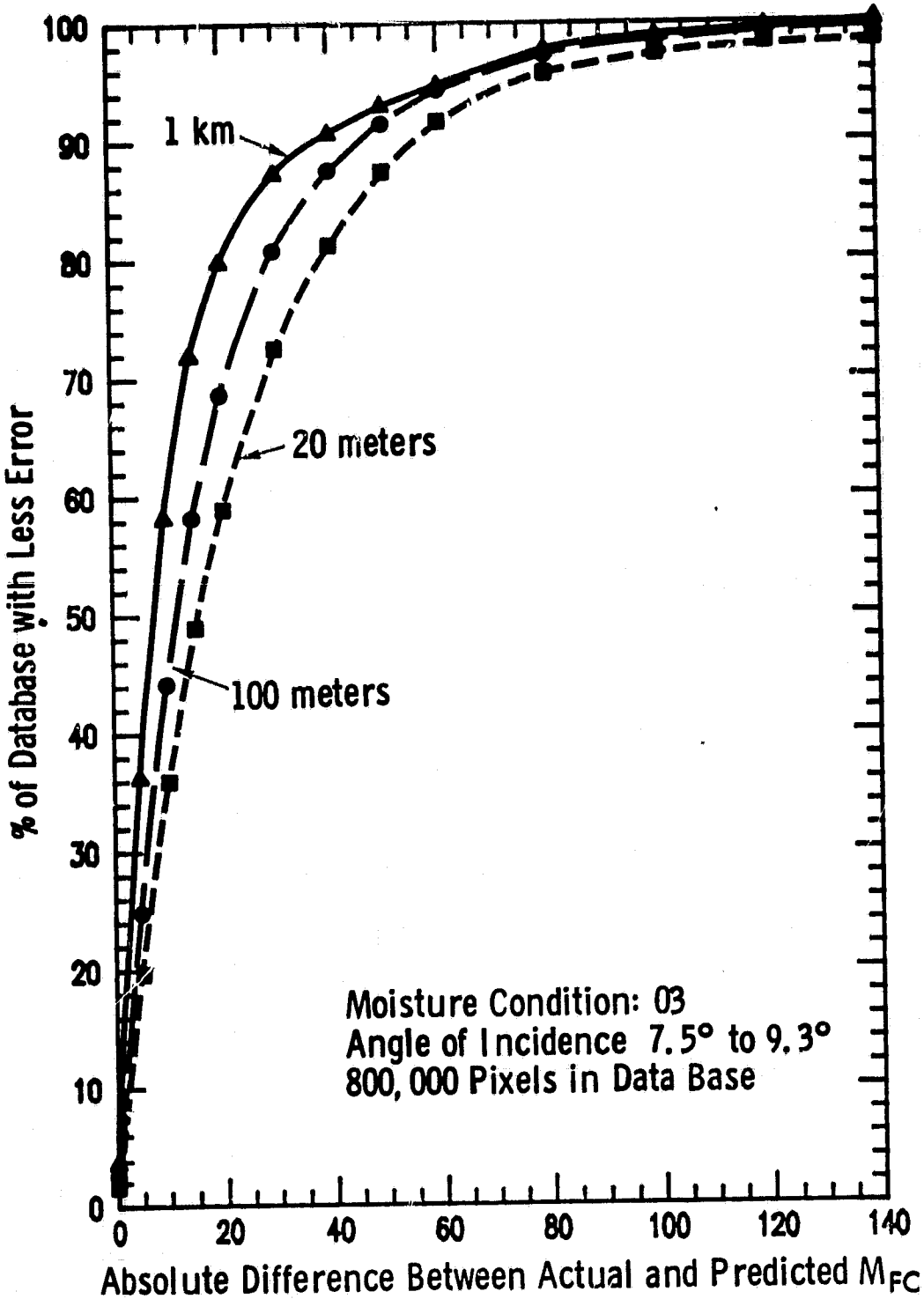

Figure 5.25. Soil Moisture Estimate Accuracy for the Entire Simulation Data Base With Moisture Condition 3, 10 Days After Thunderstorm, and at Angles of Incidence Between 7.5° and 9.3°.

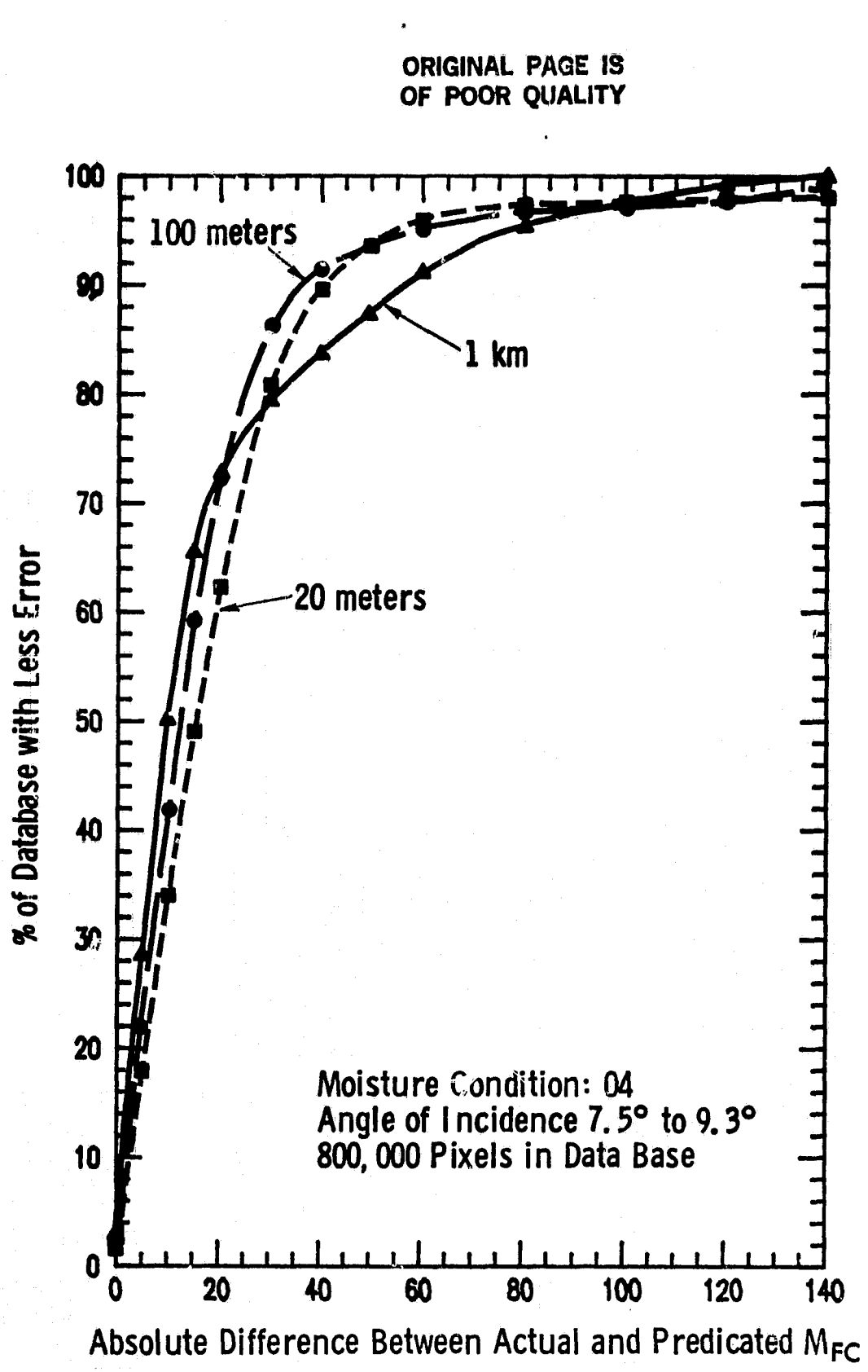

Figure 5.26. Soil Moisture Estimate Accuracy for the Entire Simulation Data Base with Moisture Condition 4, Drought, and at Angles of Incidence Between 7.5° and 9.3°.

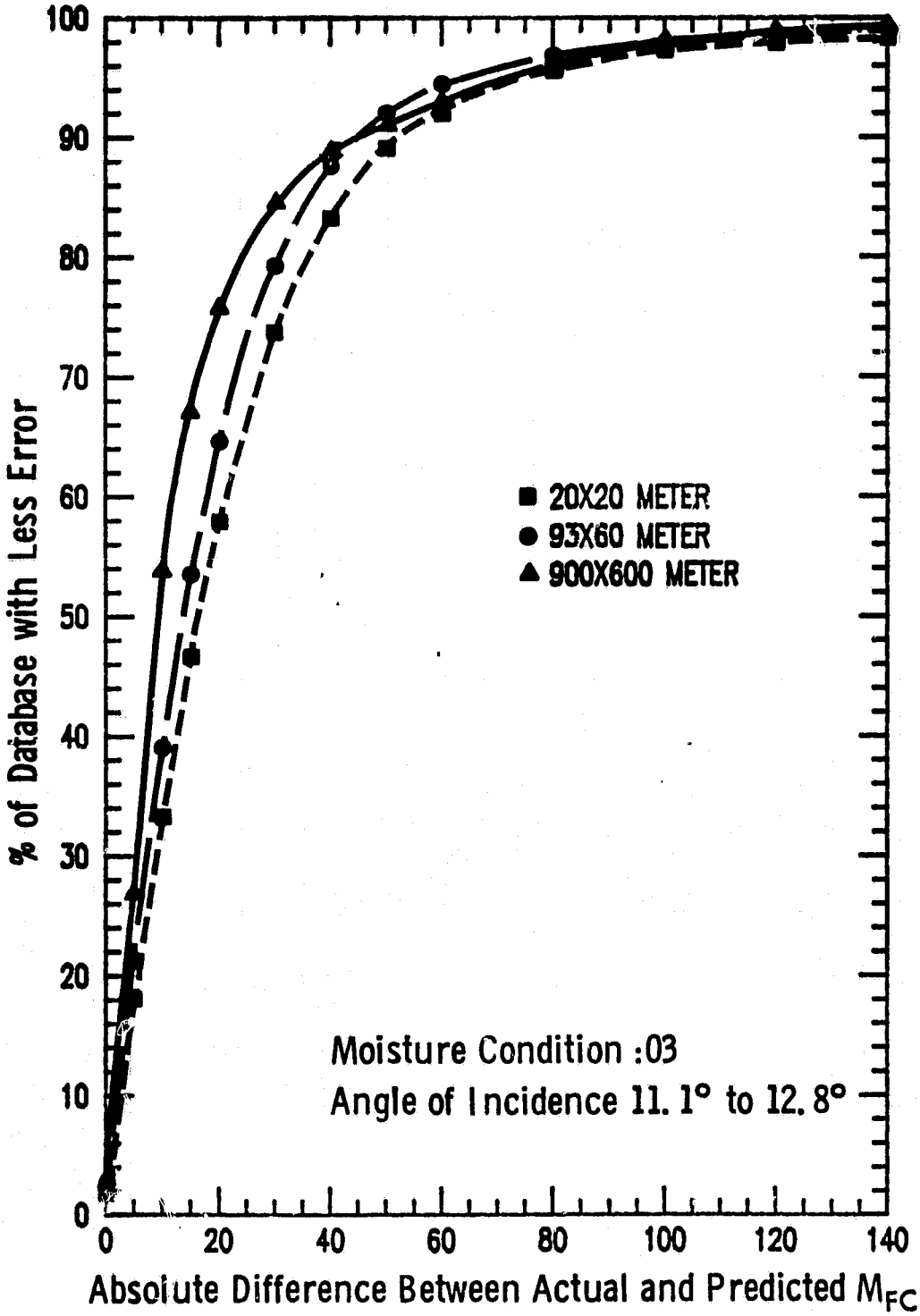

Figure 5.27 Soil moisture estimate accuracy for the entire simulation data base with Moisture Condition 3, 10 days after thunderstorm, and at angles of incidence between 11.1° and 12.8°.

TABLE 5.7

Cumulative Percent of Total Data Base Within Certain Absolute Estimate Error Limits for C-Band Simulation Results at $\theta = 7.5° - 9.3°$

Approx. User Accuracy Level [51] →		1	2	3	4	5
+/- % of field capacity →		50	40	30	20	10
Moisture Condition ↓	Resolution ↓					
1	20 x 20 m	79.2	74.5	67.2	55.6	34.8
	93 x 100 m	86.4	82.7	76.9	65.0	42.7
	1 x 1 km	92.5	92.1	90.7	86.6	70.1
2	20 x 20 m	76.3	70.3	61.3	47.6	27.6
	93 x 100 m	84.2	79.8	71.7	58.3	34.8
	1 x 1 km	92.4	92.1	90.8	85.9	61.3
3	20 x 20 m	87.5	81.3	72.5	58.9	35.9
	93 x 100 m	92.0	87.7	81.0	68.6	44.2
	1 x 1 km	92.9	91.0	87.4	80.4	58.6
4	20 x 20 m	93.8	89.6	80.9	62.3	34.0
	93 x 100 m	93.9	91.5	86.5	72.5	42.1
	1 x 1 km	87.3	83.5	79.3	72.6	50.3

TABLE 5.8

Cumulative Percent of Total Data Base
Within Certain Absolute Estimate
Error Limits for C-Band Simulation
Results at θ = 11.1°-12.8°

Approx. User Accuracy Level →		1	2	3	4	5
+/- % of field capacity →		50	40	30	20	10
Moisture Condition ↓	Resolution ↓					
1	20 x 20 m	79.0	74.2	67.2	54.9	33.0
	93 x 60 m	83.7	79.3	72.7	60.8	37.3
	900 x 600 m	91.0	89.8	87.1	80.6	62.8
2	20 x 20 m	74.8	70.1	62.2	49.3	29.2
	93 x 60 m	80.6	76.1	68.1	54.7	33.8
	900 x 600 m	91.8	91.0	88.6	81.8	55.6
3	20 x 20 m	89.0	83.1	73.6	57.8	33.1
	93 x 60 m	92.0	87.6	79.3	64.6	38.9
	900 x 600 m	91.1	88.7	84.5	75.7	53.8
4	20 x 20 m	92.4	86.8	76.0	57.8	32.7
	93 x 60 m	93.6	90.2	82.8	67.3	37.6
	900 x 600 m	83.4	81.2	79.0	74.2	49.5

and railroads have a constant $\bar{\sigma}^{\circ}$ of 10 dB and for very dry moisture conditions the backscatter from agricultural terrain adjacent to such targets is typically 20 to 25 dB less. Thus during extremely dry conditions, the large spatial averaging inherent in the 1 km resolution will cause a significant overestimation of the moisture present in agricultural scenes adjacent to cultural targets characterized by a very large $\bar{\sigma}^{\circ}$. As a consequence, it is expected that the spatial density of such targets within a given area will effectively determine the upper limit of desireable resolution for accurately sensing very dry soil moisture conditions. Thus, for agronomic regions similar to the data base, resolutions on the order of $\leq$ 1 km would be adequate for dry conditions, while for areas such as the high plains (where the density of cultural targets is lower than that simulated) resolution $\geq$ 1 km might prove adequate. On the other hand, accurate sensing of very dry moisture conditions in regions with dense distributions of hard cultural targets such as the northeastern United States and northern Europe would require a resolution less than 1 km.

The estimate accuracy of the 20 m resolution is seriously affected by local slope and crop canopy cover. The effects of local slope are most pronounced for high moistures (Moisture Conditions 1 and 2) since the sensitivity of $\bar{\sigma}^{\circ}$ to local incidence angle is greatest for high soil moisture. This is reflected in the generally lower estimate accuracy of the 20 meter resolution for Moisture Conditions 1 and 2 than for Moisture Conditions 3 and 4 where the angular dependence of $\bar{\sigma}^{\circ}$ is less pronounced.

5.5 Analysis of Moisture Estimate Accuracy Within the Floodplain

In order to minimize the analytic bias introduced by uncorrected foreshortening of the predicted moisture maps, moisture estimate accuracy

is presented in Tables 5.9 and 5.10 for each resolution and moisture condition for only those pixels on the relatively flat river floodplain. Approximately 183,000 data-base pixels comprise this region or about 23% of the data base. Geometric registration of the predicted moisture maps to the coordinate grid of the data base was optimized for this region. The floodplain was arbitrarily defined by all pixels in the data base with elevation less than or equal to 820 feet. In addition, the values given in Tables 5.9 and 5.10 exclude pixels classified in the data base as water bodies, buildings, railroads, bridges, roads, trees, and sandbars, thereby minimizing that component of net estimate error related to pixels with undefined "actual" soil moisture.

While the values in Tables 5.9 and 5.10 are significantly higher than those shown in Tables 5.7 and 5.8 for the entire data base, they reflect the same general trends with respect to moisture condition and resolution. The 1-km resolution results in the highest estimate accuracy at all accuracy levels except for the very dry moisture condition present 30 days after the thunderstorm. Also, estimate accuracy is generally lower at all resolutions for either the extremely wet or extremely dry moisture conditions (Moisture Conditions 2 and 4 respectively) than for the more typical intermediate moisture conditions. This is expected since the effects of surface roughness and crop canopy cover cause a divergence of $\bar{\sigma}^{o}$ between the target classes at the moisture extremes.

The cumulative percent of the 183,000 pixels comprising the agricultural floodplain is plotted versus maximum absolute estimate error in Figures 5.28 to 5.31 for Moisture Conditions 1 to 4, respectively, for the 7.5° to 9.3° angular swath and in Figure 5.32 for Moisture Condition 3 and the 11.1° to 12.8° angular swath. At Accuracy Level 4,

TABLE 5.9

Cumulative Percent of Agricultural Floodplain Within Certain Absolute Error Limits for C-Band Simulation Results at $\theta = 7.5° - 9.3°$

All pixels in the data base where elevation is > 820 feet are excluded and all non-agricultural pixels are excluded from analysis.

Approx. User Accuracy Level→		1	2	3	4	5
+/- % of field capacity →		50	40	30	20	10
Moisture Condition ↓	Resolution ↓					
1	20 x 20 m	96.4	94.3	89.9	79.1	52.4
	93 x 100 m	99.6	98.7	96.2	87.6	63.8
	1 x 1 km	100.0	99.9	99.4	96.3	76.8
2	20 x 20 m	93.6	88.5	79.2	64.4	39.6
	93 x 100 m	98.9	95.7	87.6	75.4	47.2
	1 x 1 km	100.0	99.9	98.8	92.8	68.7
3	20 x 20 m	97.1	95.3	91.3	80.9	53.2
	93 x 100 m	98.9	98.0	96.0	89.2	64.0
	1 x 1 km	99.0	98.2	94.6	85.9	60.6
4	20 x 20 m	97.9	95.9	89.8	71.4	39.7
	93 x 100 m	97.2	96.2	93.6	81.2	47.4
	1 x 1 km	89.0	84.4	82.7	77.6	50.5

TABLE 5.10

Cumulative Percent of Agricultural Floodplain Within Certain Absolute Error Limits for C-Band Simulation Results at θ = 11.1°-12.8°

Moisture Condition ↓	Resolution	Approx. User Accuracy Level				
		1	2	3	4	5
		+/- % of Field Capacity				
		50	40	30	20	10
1	20 x 20 m	96.6	94.7	90.4	78.3	48.9
	93 x 60 m	98.4	97.1	94.7	87.2	58.7
	900 x 600 m	99.6	99.2	98.4	94.0	73.6
2	20 x 20 m	95.0	91.3	82.8	66.5	40.3
	93 x 60 m	98.4	96.4	89.4	74.6	49.3
	900 x 600 m	99.9	99.8	98.6	93.2	73.2
3	20 x 20 m	97.0	94.5	88.9	75.5	46.4
	93 x 60 m	97.7	96.5	92.9	83.4	55.4
	900 x 600 m	97.6	96.7	92.8	81.9	54.6
4	20 x 20 m	96.40	91.97	81.1	61.0	34.1
	93 x 60 m	96.8	94.5	87.2	70.8	37.7
	900 x 600 m	83.9	83.2	82.2	78.8	53.7

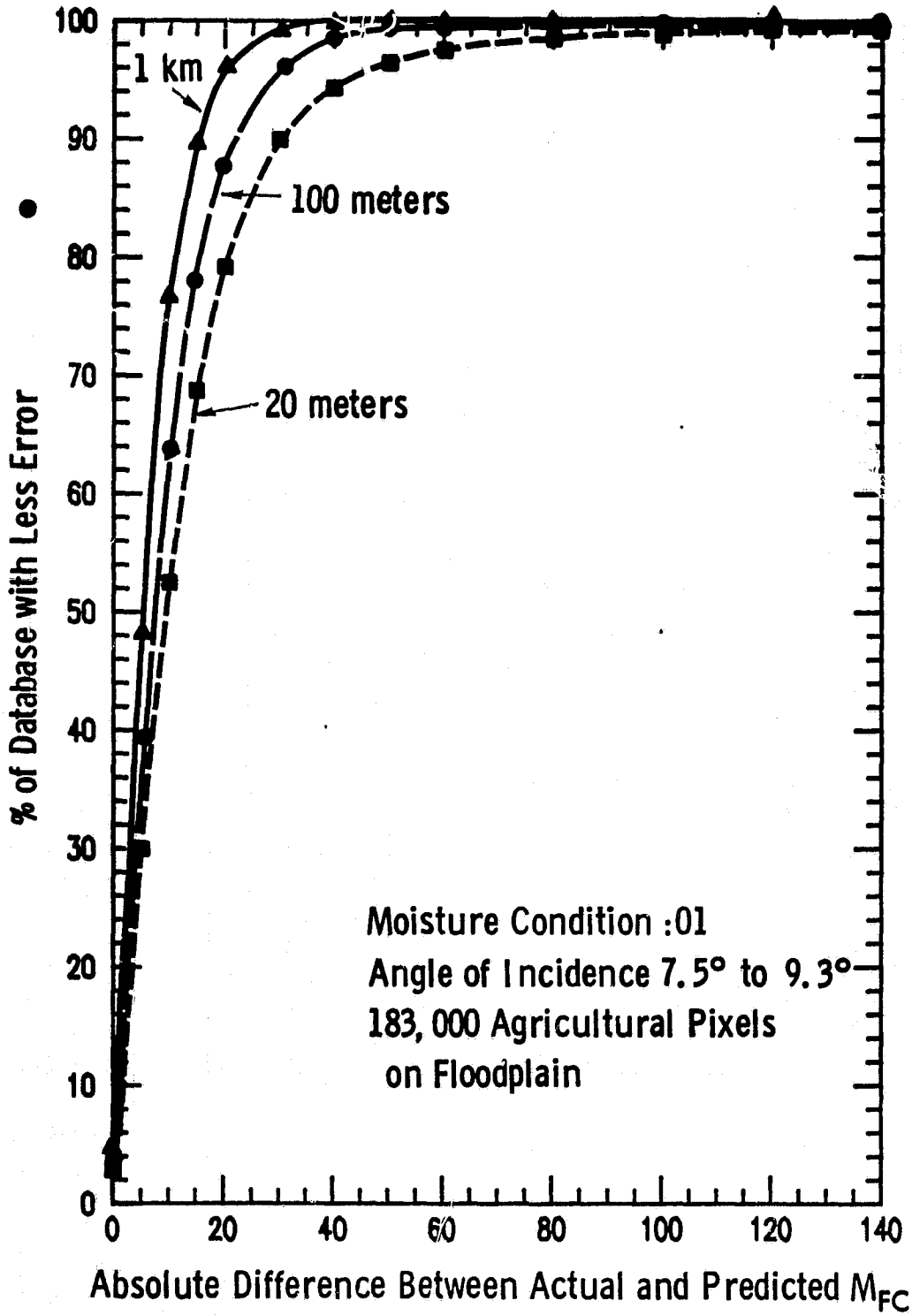

Figure 5.28. Soil Moisture Estimate Accuracy for Agricultural Categories on the Floodplain with Moisture Condition 1, all Soil at Field Capacity, and at Angles of Incidence between 7.5° and 9.3°.

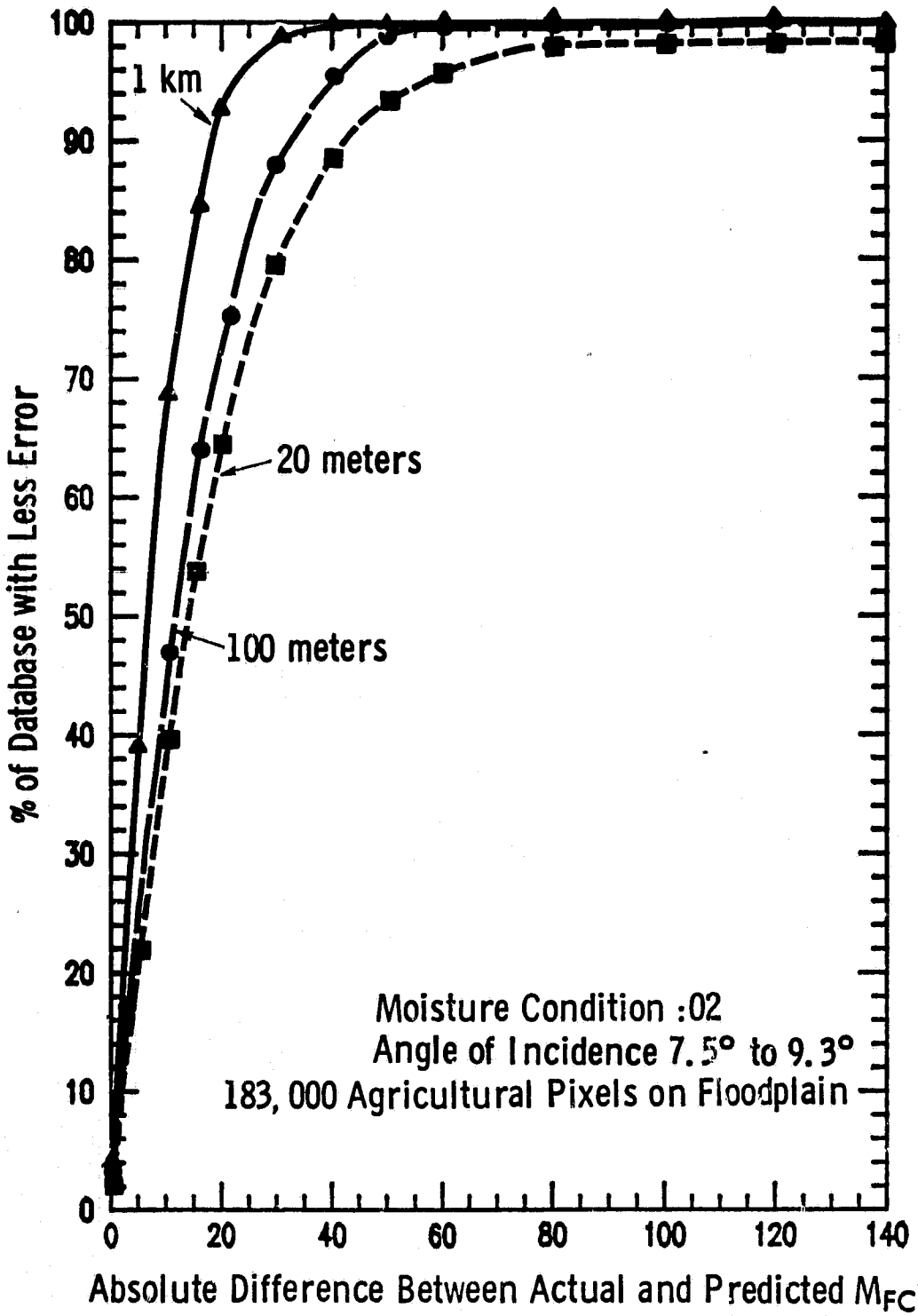

Figure 5.29 Soil moisture estimate accuracy for agricultural categories on the floodplain with Moisture Condition 2, saturated soil, and at angles of incidence between 7.5° and 9.3°.

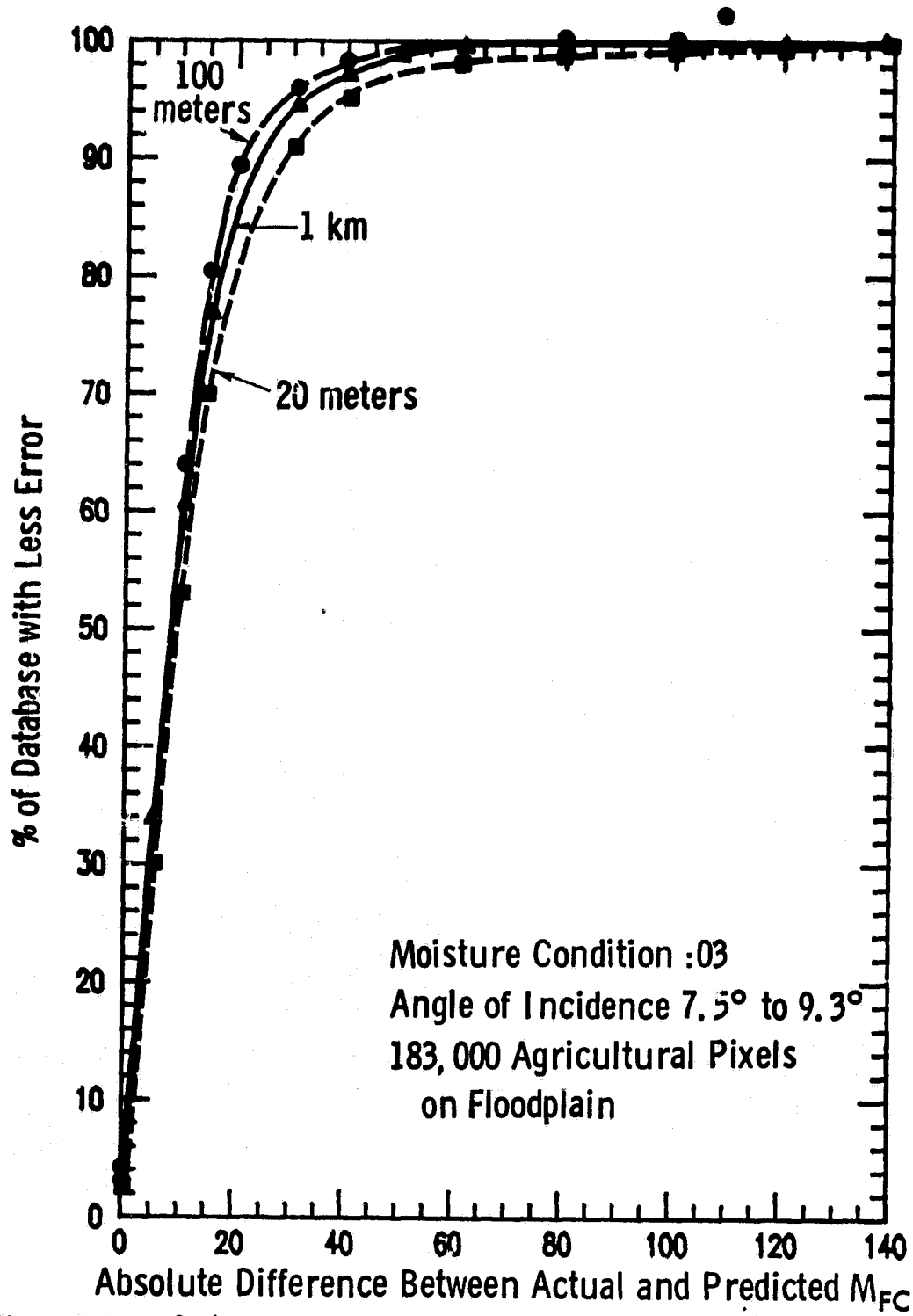

Figure 5.30 Soil Moisture Estimate Accuracy for Agricultural Categories on the Floodplain with Moisture Condition 3, 10 Days after Thunderstorm, and at Angles of Incidence between 7.5° and 9.3°.

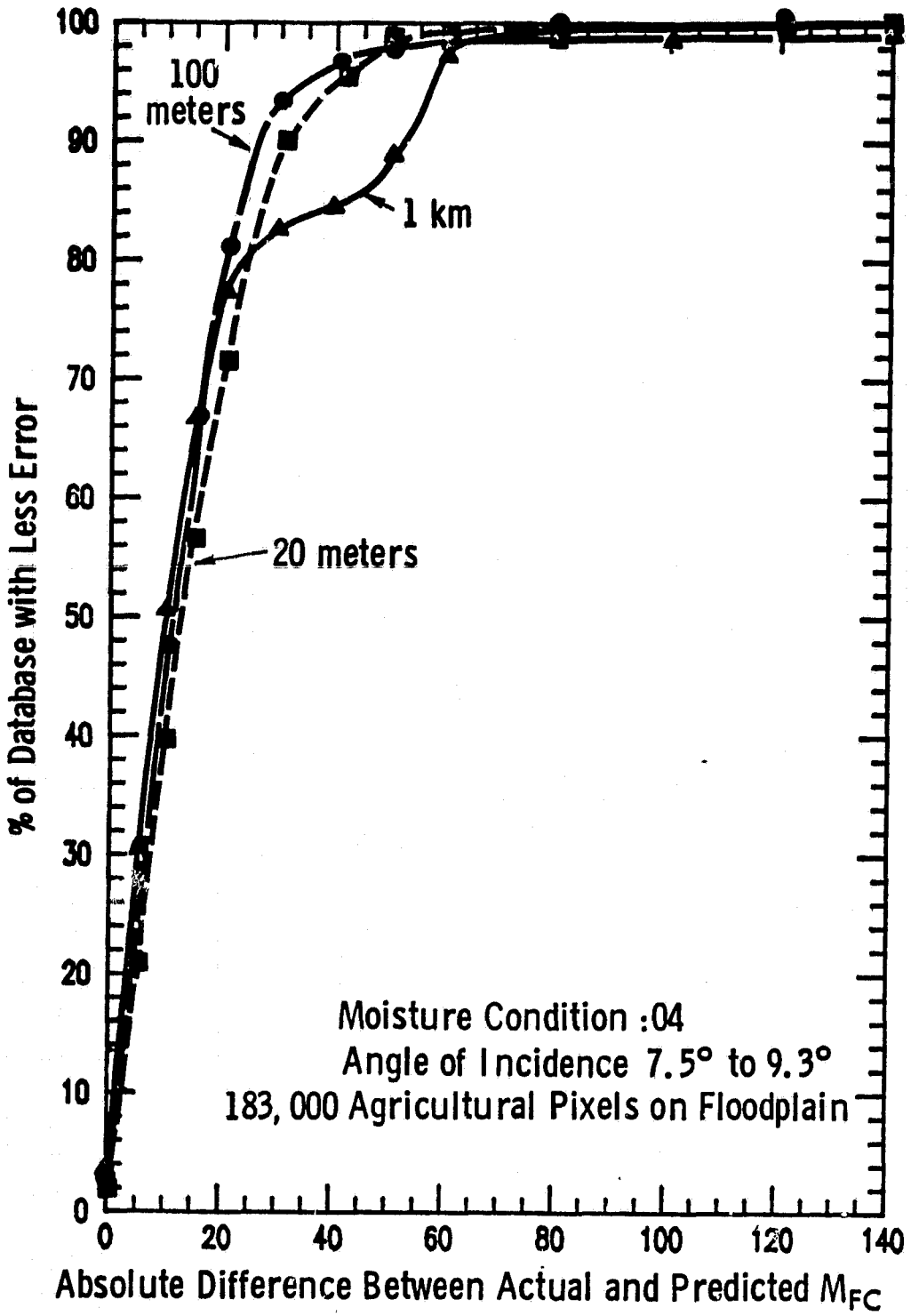

Figure 5.31 Soil moisture estimate accuracy for agricultural categories on the floodplain with Moisture Condition 4, drought, and at angles of incidence between 7.5° and 9.3°.

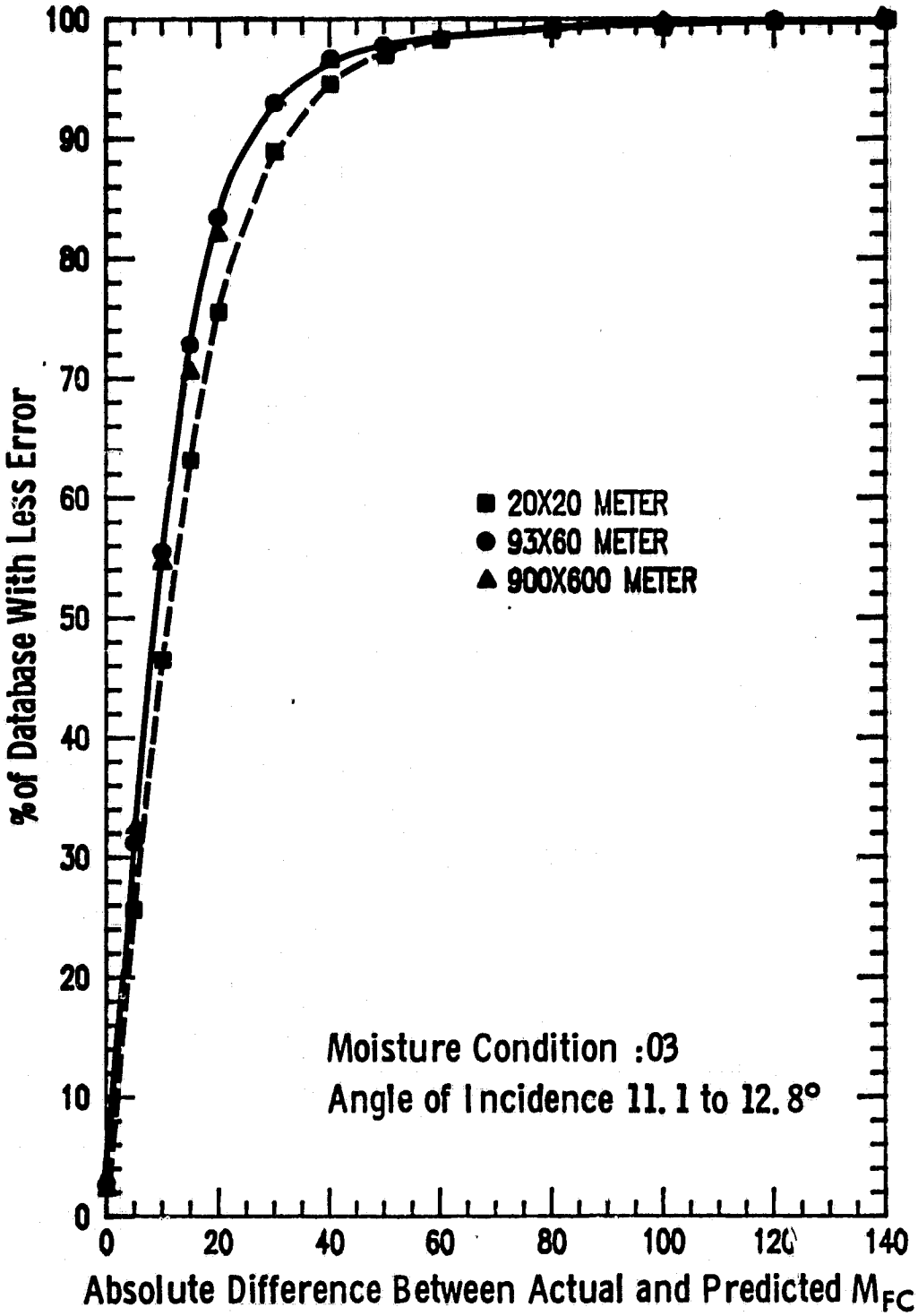

Figure 5.32 Soil moisture estimate accuracy for agricultural categories on the floodplain with Moisture Condition 3, 10 days after thunderstorm, and with angles of incidence between 11.1° and 12.8°.

$\hat{M}_{FC}$ = +/- 20% plus M_{FC}, 78% to 96% of the agricultural floodplain is accurately mapped for 0-5 cm soil moisture by the 1 km resolution radar, 81% to 89% by the 100 meter resolution system, and 64% to 81% by the 20-meter resolution system depending upon the moisture condition. The lower accuracy of the 1 km resolution in Figure 5.31 is caused by the averaging of relatively high $\bar{\sigma}^{o}$ for hard cultural targets over a larger area. In the case of the simulated floodplain region, this is primarily related to the presence of a railroad running east to west and secondarily to scattered point targets such as buildings.

The effects of resolution and moisture condition on estimate accuracy are summarized in Figures 5.33 and 5.34 for the 7.5° to 9.3° angular swath at Accuracy Levels 3 and 4 respectively. Accuracy of moisture estimation using Equation 5.3 is shown to be significantly higher on the agricultural floodplain than for the data base as a whole. Similar results were obtained for the 11.1° to 12.8° angular swath.

Effects of Crop Type, Surface Roughness, and Row Direction

The area percent of the agricultural floodplain occupied by each of 13 major agricultural categories of crops and surface roughness are given in Table 5.11. Row crops are differentiated as to row orientation relative to radar look direction. Approximately 33% of the area is comprised of bare soil and the rest is mainly cropped with corn, milo, soybeans, and wheat. The percentage of pixels for each crop class which have estimated moisture $\hat{M}_{FC}$ within +/- 20% from the actual M_{FC} are tabulated for each resolution and moisture condition in Tables 5.12 and 5.13. For the 20-meter resolution (and to a lesser extent the 100 meter

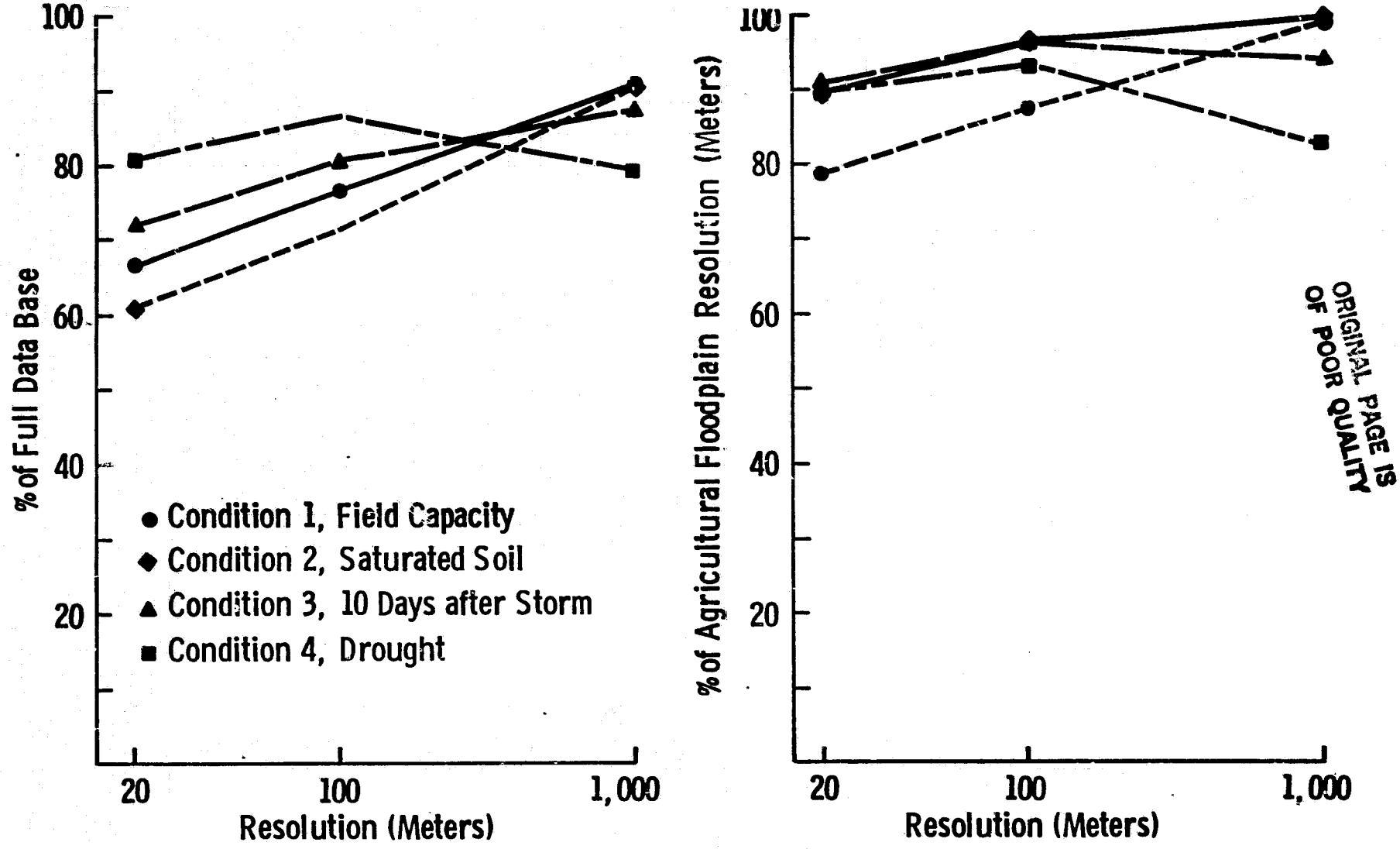

Figure 5.33 Percent of data base where estimated moisture M_{FC} is within ±30% of actual moisture M_{FC}. Angle of incidence θ is 7.5° to 9.3° relative to nadir. Accuracy level 3 is approximately ±30% of field capacity.

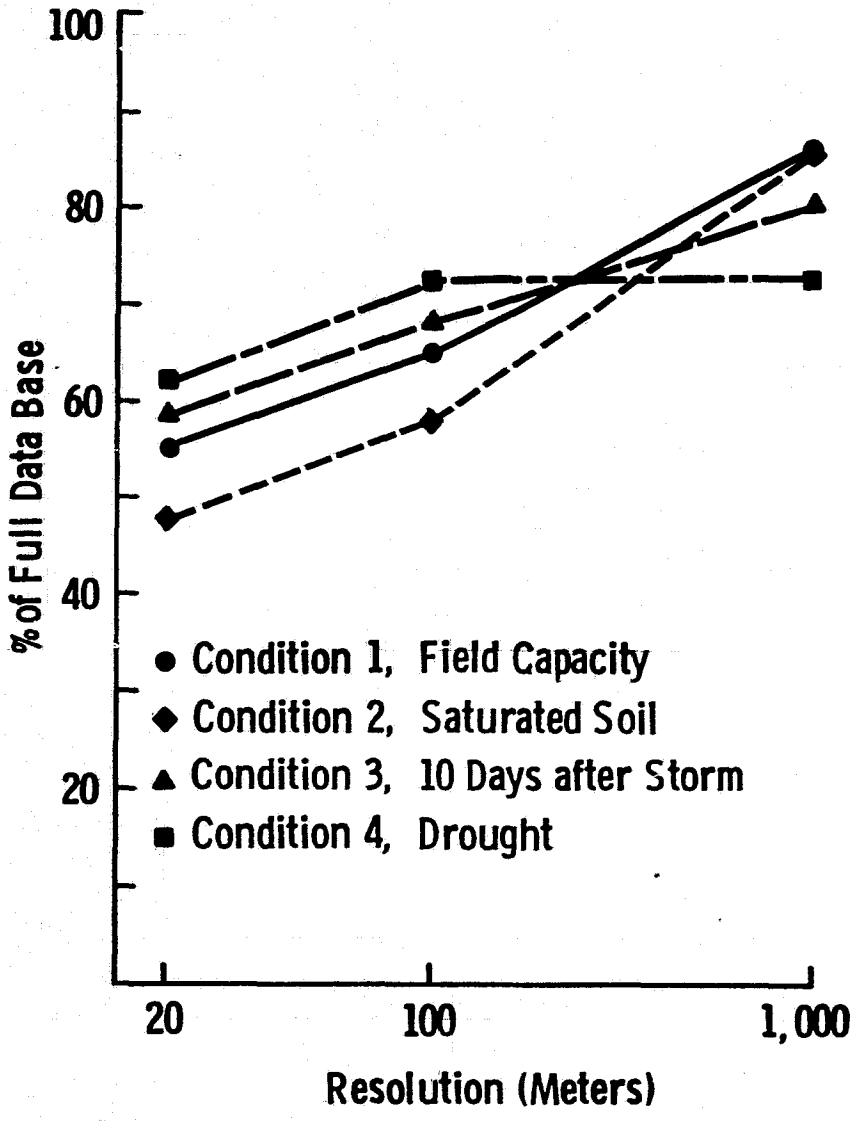

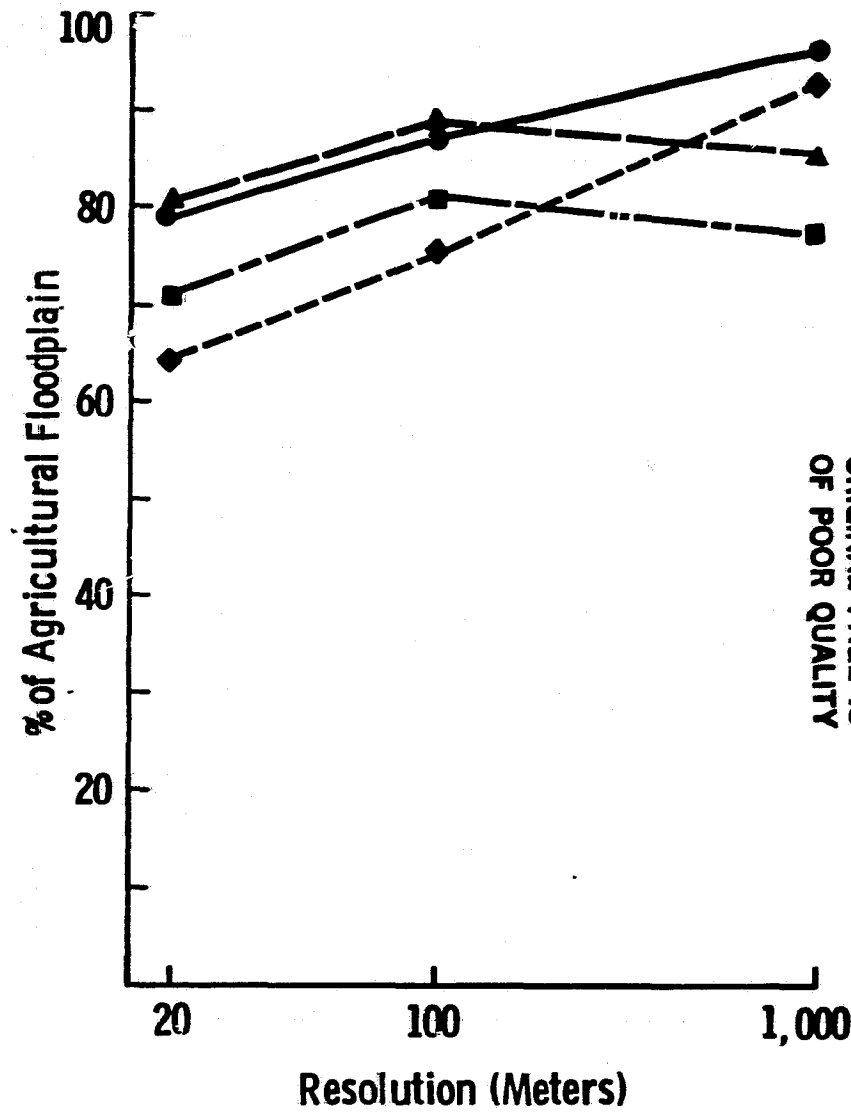

Figure 5.34 Percent of data base where estimated moisture M_{FC} is within ±20% of actual moisture M_{FC}. Angle of incidence θ is 7.5° to 9.3° relative to nadir. Accuracy level 4 is approximately ±20° of field capacity.

TABLE 5.11

Area Percent of the Agricultural Floodplain for Crop Categories; Floodplain is Defined by Elevation ≤ 820 Feet

Crop Category		Area Percent
Bare Soil -	Smooth	15.20
	Medium Rough	10.26
	Rough	7.09
	All Roughnesses	32.55
Pasture		5.13
Mown Pasture		0.51
Alfalfa		5.54
Soybeans -	Parallel	5.54
	Perpendicular	5.36
	All Soybeans	10.90
Milo -	Parallel	6.96
	Perpendicular	7.50
	All Milo	14.46
Corn -	Parallel	9.56
	Perpendicular	11.88
	All Corn	21.44
Wheat		9.47
All Crops and Pasture		67.45

TABLE 5.12

+/- 20% Accuracy Levels for Crop Categories on the Floodplain for the 7.5° to 9.3° Angular Swath

		Percent of Category Within +/- 20% Estimate Accuracy											
Moisture Condition →		1			2			3			4		
Resolution →		20m	100m	1km	20m	100m	1km	20m	100m	1km	20m	100m	1km
Crop ↓	% of Flood-plain ↓												
All Classes	100.0	79	88	96	64	75	93	81	89	86	71	81	78
Bare - Smooth	15.2	31	91	97	82	92	97	72	86	81	56	77	83
Bare - Medium Rough	10.3	86	95	95	85	95	96	82	93	90	80	93	85
Bare - Rough	7.1	86	93	94	85	91	92	87	94	82	87	95	85
Pasture	5.1	68	76	97	50	67	91	69	77	87	68	79	71
Alfalfa	5.5	79	82	86	54	71	98	81	80	71	76	75	49
Soybeans //	5.5	88	96	97	84	94	89	90	95	84	90	93	72
Soybeans ⊥	5.4	90	95	97	86	94	98	87	92	89	87	89	80
Milo //	7.0	45	55	93	5	12	71	78	88	84	84	88	64
Milo ⊥	7.5	57	68	98	9	17	91	82	91	91	76	83	74
Corn //	9.6	88	96	98	72	83	90	86	93	93	61	72	83
Corn ⊥	11.9	87	95	99	75	86	94	79	87	87	50	57	81
Wheat	9.5	85	93	99	57	74	99	86	93	89	81	91	79

TABLE 5.13

± 20% Accuracy Levels for Crop Categories on the Floodplain for the 11.1° to 12.8° Angular Swath

Crops	Percent of Floodplain	Moisture Condition											
		1			2			3			4		
		Resolution											
		20m	100m	1 Km	20m	100m	1 Km	20m	100m	1 Km	20m	100m	1 Km
All classes	100.0	78	87	94	67	75	93	76	83	82	61	71	79
Smooth Bare	15.2	74	84	93	82	91	96	50	58	78	14	25	84
Medium Rough Bare	10.3	77	91	95	48	62	98	82	93	87	74	87	86
Rough Bare	7.1	80	94	95	56	75	98	87	94	81	86	95	86
Pasture	5.1	64	68	89	60	67	83	67	74	77	76	84	72
Alfalfa	5.5	76	75	79	75	79	91	77	77	67	77	79	51
Soybeans //	5.5	88	96	93	87	94	93	88	94	80	89	95	79
Soybeans ⊥	5.4	85	93	99	85	93	99	82	91	87	79	88	81
Milo //	7.0	64	73	93	16	18	77	82	90	81	74	87	70
Milo ⊥	7.5	77	97	98	32	28	93	84	92	88	55	67	75
Corn //	9.6	87	95	96	77	87	91	84	93	91	62	74	87
Corn ⊥	11.9	83	93	98	82	90	96	70	81	82	43	48	80
Wheat	9.5	82	89	96	82	89	97	82	90	80	79	92	77

resolution) most of the estimate error is concentrated within the categories of milo, wheat, alfalfa, and corn for saturated moisture conditions and within the categories of smooth bare soil and corn for very dry moisture conditions; and the accuracy of prediction is observed to decrease at higher incidence angles (Table 5.13). For the 20-meter resolution, the concentration of a large percentage of net estimate error within a relatively few crop classes is to be expected from the use of a general estimation algorithm such as Equation 5.3 unless that algorithm is weighted by the expected percentage of crop classes for a given region. Importantly, the need for a regional and/or time-dependent general estimation algorithm appears to be mitigated in large part by the natural averaging of local canopy effects when using a coarser resolution system. Thus, the inter-class variance in estimate error is seen to be very low for the 1 km resolution at all simulated moisture conditions in Tables 5.12 and 5.13. The only exception to the preceding statement is alfalfa, where the large estimate error for Moisture Condition 4 from the 1 km resolution is an artifact of its close proximity to the previously mentioned railroad.

Because of the high moisture estimate accuracy attained for specific agricultural classes by the foregoing approach using Equation 5.3 as the estimation algorithm, the division of the data base into bare soil and vegetation-covered classes for differential estimation of soil moisture using Equations 5.4 and 5.5 was deemed unnecessary. For the simulated conditions, it seems unlikely that the use of *a priori* information other than the location of water bodies and cultural features would significantly improve estimate accuracy and be worth the added complexity in

processing. The distribution of prediction error between target classes observed in Tables 5.12 and 5.13 indicates that surface roughness and specific crop canopy type are more significant determinants of net prediction accuracy than a dichotomous division of the agricultural terrain into bare and vegetated classes.

6.0 CONCLUDING REMARKS

The validity of results derived from any simulation of a real-world situation is inherently limited by the degree of realism incorporated in the assumptions and models used in generating the simulations. In the present study, the aspect of realism is governed by three types of factors: (a) geometrical factors associated with the image formation process of a sidelooking imaging radar, (b) signal fluctuations due to Rayleigh fading (speckle effect) in radar images that contain a small number of independent samples per pixel element, and (c) the models characterizing the backscatter behavior of the various target classes contained in the simulated scene. The first two types of factors are well understood; therefore, it was possible to incorporate them in the simulation algorithm with a high degree of accuracy. This accuracy was verified in a separate study through comparisons of simulated SAR images with actual images of the same scene. The degree of realism associated with the third type of factor--the backscatter models--is very good, if considered in statistical terms. That is, the functions used to describe the dependence of the backscattering coefficient $\bar{\sigma}^o$ on the local angle of incidence θ_ℓ and moisture content M_{FC} (for agricultural categories) are based on statistical regressions applied to

experimental data obtained over the past eight years. In the majority of cases, the correlation coefficients associated with these regressions are greater than 0.8, which means that the regressions account for the majority of the observed variation in $\bar{\sigma}^o$, but some variation, part of which is due to measurement error, remains unaccounted for. Considering that the overall study is, to some extent, statistical in nature, the approach used above for modeling the backscatter behavior is certainly justified.

The major conclusions derived from this study are:

(1) Among the three resolutions considered (20 m, 100 km, and 1 km), soil moisture content was estimated with the highest accuracy by the 1-km resolution radar images for the relatively wet soil conditions (Cases 1 and 2 of Table 4.7), comparable levels of accuracy were provided by the 100 m and 1 km resolutions for Case 3 (10 days after the thunderstorm), and the 100 m resolution provided significantly better results than the 1 km resolution for the drought case (30 days after the thunderstorm).

(2) Based on the above results, it appears that a spatial resolution between 100 m and 1 km would provide optimum performance over the various soil moisture conditions. Narrowing this range down to a specific value is the object of a further phase of this investigation.

(3) This study was performed for a test site in eastern Kansas, where dry-land farming practices prevail. For such regions, the periodic structure associated with soil surfaces of row crops exercises a minor influence on the scattering behavior as a function of radar look-direction relative to row-direction (for the sensor parameters specified in this study). In regions where irrigation practices are common, the row structures usually have larger amplitudes, which would lead to greater ambiguity in the soil moisture estimation process for like-polarized

radar configurations. Research conducted to date indicates that the cross-polarized scattering coefficient is significantly less sensitive to row direction and, therefore, should be preferred for mapping soil-moisture content in irrigated regions. The major drawback to the use of cross-polarization is the fact that more transmitter power is required than for the like-polarized case. However, since the needed resolution is of the order of hundreds of meters, it may be possible to configure a cross-polarized space radar system with existing technology.

REFERENCES

[1] Ulaby, F. T., "Radar Measurement of Soil Moisture Content," IEEE Trans. on Antennas and Propagation, Vol. AP-22, No. 2, pp. 257-265, March 1974.

[2] Ulaby, F. T., J. Cihlar and R. K. Moore, "Active Microwave Measurement of Soil Water Content," Remote Sensing of Environment, Vol. 3, pp. 185-203, January 1975.

[3] Ulaby, F. T. and P. P. Batlivala, "Optimum Radar Parameters for Mapping Soil Moisture," IEEE Transactions on Geoscience Electronics, Vol. GE-14, No. 2, pp. 81-93, April 1976.

[4] Ulaby, F. T., P. P. Batlivala and M. C. Dobson, "Microwave Backscatter Dependence on Surface Roughness, Soil Moisture and Soil Texture: Part I -- Bare Soil," IEEE Transactions on Geoscience Electronics, Vol. GE-16, No. 4, pp. 286-295, October 1978.

[5] Dobson, M. C. and F. T. Ulaby, "Microwave Backscatter Dependence on Surface Roughness, Soil Moisture and Soil Texture: Part III -- Soil Tension," IEEE Transactions on Geoscience and Remote Sensing, Vol. GE-19, No. 1, pp. 51-61, January 1981.

[6] de Loor, G. P., "Soil Moisture Determination at X-Band," Proceedings of the Microwave Remote Sensing on Bare Soil Workshop, EARSeL, Paris, pp. 198-202, April 1979.

[7] King, Christine, "Contribution a l'Utilisation des Micro-Ondes dans l'Étude des Sols," Thesis, Institut National Agronomique, Paris, France, March 1978.

[8] Le Toan, M., G. Flouzat, M. Pausader, A. Fluhr and A. Lopes, "Multifrequency Radar Measurements of Soil Parameters," COSPAR, Budapest, Hungary, June 1980.

[9] Haruto, Hirosawa, S. Komiyama and Y. Matsuzaka, "Cross-Polarized Radar Backscatter from Moist Soil," Remote Sensing of Environment, Vol. 7, No. 3, pp. 211-217, August 1978.

[10] Fenner, R. G., G. F. Pels and S. C. Reid, "A Parametric Study of Tillage Effects on Radar Backscatter," Terrain and Sea Scatter Workshops Report, Washington, D.C., (printed by Remote Sensing Laboratory, University of Kansas, Lawrence, Kansas 66045), March 1980.

[11] Ulaby, F. T., "Radar Response to Vegetation," IEEE Trans. on Antennas and Propagation, Vol. AP-23, No. 1, January 1975.

[12] Ulaby, F. T., T. F. Bush and P. P. Batlivala, "Radar Response to Vegetation II: 8-18 GHz Band," IEEE Trans. on Antennas and Propagation, Vol. AP-23, No. 5, pp. 608-618, September 1975.

[13] Ulaby, F. T. and J. E. Bare, "Look-Direction Modulation Function of the Radar Backscattering Coefficient of Agricultural Fields," Photogrammetric Engineering and Remote Sensing, Vol. 45, No. 11, pp. 1495-1506, November 1979.

[14] Ulaby, F. T., G. A. Bradley and M. C. Dobson, "Microwave Backscatter Dependence on Surface Roughness, Soil Moisture and Soil Texture: Part II -- Vegetation-Covered Soil," IEEE Transactions on Geoscience Electronics, Vol. GE-17, No. 2, pp. 33-40, April 1979.

[15] Dickey, F. M., C. King, J. C. Holtzman and R. K. Moore, "Moisture Dependency of Radar Backscatter from Irrigated and Non-Irrigated Fields at 400 MHz and 13.3 GHz," IEEE Trans. on Geoscience Electronics, Vol. GE-12, No. 1, pp. 19-22, 1974.

[16] Blanchard, Bruce J., "Measurement of Soil Moisture Trends with Airborne Scatterometers," Progress Report RSC 3458-2, Remote Sensing Center, Texas A&M University, College Station, Texas, June 1978.

[17] Jackson, T. J., A. Chang and T. J. Schmugge, "Aircraft Active Microwave Measurements for Estimating Soil Moisture," submitted for publication in Photogrammetric Engineering and Remote Sensing.

[18] Bradley, G. A. and F. T. Ulaby, "Aircraft Radar Response to Soil Moisture," RSL Technical Report 460-2 (AgRISTARS SM-KO-04005), University of Kansas Center for Research, Inc., Lawrence, Kansas 66045, October 1980.

[19] Eagleman, J. and F. T. Ulaby, "Radiometer-Scatterometer Soil Moisture Detection," Proceedings of the American Astronomical Society Meeting, Los Angeles, California, August 1974.

[20] Blanchard, Bruce J., Private Communication.

[21] Ulaby, F. T., F. Kouyate and A. K. Fung, "A Backscatter Model For A Randomly Perturbed Periodic Surface," RSL Technical Report 460-4, University of Kansas Center for Research, Inc., Lawrence, Kansas 66045, February 1981.

[22] Wang, J. L. and T. J. Schmugge, "An Empirical Model for the Complex Dielectric Permittivity of Soils as a Function of Water Content," IEEE Trans. Geos. and Rem. Sensing, Vol. GE-18, No. 4, pp. 288-295, October 1980.

[23] J. R. Lundien, "Terrain Analysis by Electromagnetic Means," U.S. Army Engineer Waterways Experiment Station, Vicksburg, MS, Technical Report 3-727, February 1971.

[24] R. W. Newton, "Microwave Remote Sensing and its Application to Soil Moisture Detection," Texas A&M University, College Station, Texas, Technical Report RSC-81, January 1977.

[25] Schmugge, T. J., "Effect of Texture on Microwave Emission from Soils," IEEE Transactions on Geoscience and Remote Sensing, Vol. GE-18, No. 4, pp. 353-361, October 1980.

[26] Moore, R. K., "Tradeoff Between Picture Element Dimensions and Noncoherent Averaging in Side-Looking Airborne Radar," IEEE Transactions on Aerospace and Electronic Systems, Vol. AES-15, No. 5, pp. 697-708, 1979.

[27] Moore, R. K. and G. C. Thomann, "Imaging Radars for Geoscience Use," IEEE Transactions on Geoscience Electronics, Vol. GE-9, No. 3, pp. 155-164, July 1971.

[28] Stiles, J. A., V. S. Frost, S. A. Smith and J. C. Holtzman, "Coherent and Partially Coherent Radar System Models and Simulation," RSL Technical Report 418-1, University of Kansas Center for Research, Inc., Lawrence, Kansas 66045, October 1980.

[29] Moore, R. K., "Ground Echo," Radar Handbook, ed. M. I. Skolvik, Chapter 25, McGraw-Hill, 1970.

[30] Bush, T. F. and F. T. Ulaby, "Fading Characteristics of Panchromatic Radar Backscatter from Selected Agricultural Targets," IEEE Transactions on Geoscience Electronics, Vol. GE-13, No. 4, pp. 149-157, October 1975.

[31] Goodman, J. W., "Some Fundamental Properties of Speckle," Journal Opt. Soc. Am., Vol. 66, No. 11, pp. 1145-1150, November 1976.

[32] Meyer, P. P. and H. A. Mayer, Radar Target Detection, Academic Press, New York, 1973.

[33] Frost, V. S., "Development of Statistical Models for Radar Image Analysis and Simulation," M.S. Thesis, Univeristy of Kansas, Department of Electrical Engineering, 1978.

[34] Moore, R. K., "Microwave Remote Sensing," Manual of Remote Sensing. Am. Soc. of Photogrammetry, Falls Church, Virginia, 1975.

[35] Harger, Robert O., Synthetic Aperture Radar Systems: Theory and Design, Academic Press, New York, 1970.

[36] Porcello, Leonard J., Norman G. Massey, Richard B. Innes and James M. Marks, "Speckle Reduction in Synthetic Aperture Radars," J. Opt. Soc. Am., Vol. 66, No. 11, pp. 1305-1311, November 1976.

[37] Zelenka, Jerry S., "Comparison of Continuous and Discrete Mixed-Integrator Processors," J. Opt. Soc. Am., Vol. 66, No. 11, pp. 1295-1304, November 1976.

[38] Davenport, W. B. Jr. and W. L. Root, An Introduction to the Theory of Random Signals and Noise, McGraw Hill, New York, 1958.

[39] Holtzman, J. C., V. H. Kaupp, J. L. Abbott, V. S. Frost, E. E. Komp and E. C. Davison, "Radar Image Simulation: Validation of the Point Scattering Method," U. S. Army Engineer Topographic Laboratories Contract, Report ETL-0017 (Vol. 1), September 1977.

[40] Batlivala, P. P. and J. Cihlar, "Joint Soil Moisture Experiment (Texas): Documentation of Radar Backscatter and Ground Truth Data," RSL Technical Report 264-1, University of Kansas Center for Research, Inc., Lawrence, Kansas, April 1975.

[41] Batlivala, P. P. and C. Dobson, "Soil Moisture Experiment (Kansas): Documentation of Radar Backscatter and Ground Truth Data," RSL Technical Report 264-7, University of Kansas Center for Research, Inc., Lawrence, Kansas, March 1976.

[42] Dobson, M. C., "1977 Bare Soil Moisture Experiment Data Documentation," RSL Technical Report 264-26, University of Kansas Center for Research, Inc., Lawrence, Kansas, May 1979.

[43] Dobson, C., H. Stiles, D. Brunfeldt, T. Metzler and S. McMeekin, "Data Documentation MAS 1-8 and MAS 8-18 1975 Vegetation Experiments," RSL Technical Report 264-15, University of Kansas Center for Research, Inc., Lawrence, Kansas, December 1977.

[44] Ulaby, S., "1977 Vegetation-Covered Soil Moisture Experiment Data Documentation," RSL Technical Report 264-27, University of Kansas Center for Research, Inc., Lawrence, Kansas, May 1979.

[45] Bush, T., F. Ulaby, T. Metzler and H. Stiles, "Seasonal Variations of the Microwave Scattering Properties of Deciduous Trees as Measured in the 1-18 GHz Spectral Range," RSL Technical Report 177-60, University of Kansas Center for Research, Inc., Lawrence, Kansas, June 1976.

[46] Kansas State Board of Agriculture, 62nd Annual Report and Farm Facts, Topeka, Kansas, 1979.

[47] Dickey, H. P., J. L. Zimmerman, R. O. Plinsky, and R. D. Davis, Soil Survey of Douglas County, Kansas, USDA/SCS, July 1977.

[48] Dickey, H. P., J. L. Zimmerman, and H. T. Rowland, Soil Survey of Jefferson County, Kansas, USDA/SCS, November 1977.

[49] Pinsky, R. O., J. L. Zimmerman, H. P. Dickey, G. N. Jorgensen, Jr., R. W. Fenwick, and W. E. Roth, Soil Survey of Johnson County, Kansas, USDA/SCS, January 1979.

[50] Zavesky, L. D. and W. C. Boatright, Soil Survey of Leavenworth and Wyandotte Counties, Kansas, USDA/SCS, February 1977.

[51] Soil Moisture Working Group, Plan of Research for Integrated Soil Moisture Studies, Recommendations of the Soil Moisture Working Group, October 1980.